Molecular Nano-electronic Devices Based on Aharonov-Bohm Interferometry

Thesis submitted for the degree of "Doctor of Philosophy"

By:

Oded Hod

Submitted to the Senate of Tel-Aviv University

October 2005

This work was carried out under the guidance of

Professor Eran Rabani

School of Chemistry, Tel-Aviv University

and

Professor Roi Baer

Institute of Chemistry, The Hebrew University of Jerusalem

This work is dedicated with **love** to my parents Dr. Emila (Emi) Freibrun and Prof. Israel (Izzy) Hod who made me who I am, to my wife Adi who makes me a whole person, and to our amazing daughter Ophir for whom we live. Without your endless support and love, this wouldn't come true.

I am grateful to my advisors Prof. Eran Rabani and Prof. Roi Baer who showed me ways to free my mind yet always kept the roads lighted. Due to your extraordinary guidance, these five years have been the most wonderful intellectual experience of my life.

I would like to thank Prof. Abraham Nitzan, Prof. Ori Cheshnovsky, Prof. Mordechai Bixon, Dr. Israel Schek, Dr. Yoram Selzer, Dr. Michael Gozin, and Barry Leibovitch for fruitful suggestions and discussions.

I would also like to thank my wonderful aunt Miri and my wonderful siblings Sivan Hod, Dr. Shahar Hod and Dr. Nir Hod for their support and help at all times.

With a lot of appreciation I thank my second father and mother - Marta (Matti) and Pinchas Zalckvar and the wonderful Einat and Noa for always being there to offer their help.

Many thanks to my friends from the group: Nurit Shental, Claudia G. Sztrum, Guy Yosef, Guy Cohen and Orly Kletenik for intriguing scientific and personal discussions who enriched my life.

I. ABSTRACT

The quest for understanding the physical principles governing sub-micronic and low dimensional systems has gained vast attention in modern physics. The invention of imaging technologies with nanometer scale resolution has opened the way for exciting scientific and technological possibilities. One major field which has recently developed immensely is the field of molecular electronics. From a scientific point of view this field has received a lot of experimental and theoretical interest. While new revolutionary experimental technologies allow the measurement of the physical properties of entities as small as a single molecule, or even a single atom, the related theories enable the utilization of highly accurate, state of the art, computational methods. Therefore the field of molecular electronics encourages an intimate synergic cooperation between experimentalists and theorists. The technological aspect involves the possible utilization of the unique physical properties of small scale systems for the fabrication of miniature new electronic and mechanical devices. This is expected to be a very important technological issue in the near future when existing electronic technologies are predicted to be exhausted.

A major goal of molecular electronics is to gain control over the conductance through a *single molecule*. An effective way suggested to control the conductance through *micrometer* scale loops is the application of a magnetic field threading the cross section of the ring. This effect, attributed to Y. Aharonov and D. Bohm, was intensively explored in mesoscopic physics studies. A natural extrapolation of these ideas to cyclic molecular devices was considered to be prohibited due to the extremely high magnetic fields expected to be involved in the control process.

The objective of the present research is to define the physical problem of utilizing, or even studying, the Aharonov-Bohm effect in scales much smaller than the microscale and to suggest an answer to this problem. This objective is important not only on a pure scientific ground but also when regarding the possible technological outcomes.

In order to fulfill this objective we use a one-dimensional continuum model of a nanometer scale Aharonov-Bohm interferometer, which is based on scattering matrix techniques. Even though very simplistic this model captures the essential physics and allows the isolation and systematic study of the important physical parameters that are crucial to gain controllable transport through miniature conducting loops. The continuum model results

suggest that despite of the nanometer scale cross section of the regarded systems, extremely high sensitivity to external magnetic fields can be achieved. The basic idea is to **weakly** couple a nanometric cyclic molecule/setup to two conducting leads, thus forming a resonant tunneling junction in which conductance occurs only through the well defined resonances of the ring. By applying a gate voltage to the ring, one can control the conducting electrons momentum and tune the system to be highly conductive at the absence of a magnetic field. Turning on a relatively low magnetic field will then shift the doubly degenerate narrow energy levels of the ring out of resonance with the leads and thus the conductance will drop sharply.

We test the predictions of the continuum model on realistic, pre-designed, molecular setups using an atomistic computational model developed for this purpose. This model is based on the semi-empirical extended Hückel approach which is properly adjusted for the calculation of the electronic structure of the molecule under the influence of an externally applied magnetic field. We use non-equilibrium Green's function formalism to calculate the conductance through the molecular setup in the presence of the magnetic fields. In the absence of inelastic scattering this reduces to the Landauer formula which relates the conductance to the transmission probability of an electron through the molecular frame. The transmission probability is in turn calculated using scattering theory approaches such as Green's function techniques and absorbing imaginary potentials methods. The results obtained by the atomistic calculations are found to be fully reproducible by a single parameter fit of the continuum model.

After exploring two terminal interferometers using the methodology described above, an expansion of the continuum model to the three terminal case is presented. It is found that in such a setup the symmetry breaking nature of magnetic fields allow the selective control of the electrons outgoing route. This property is unique to magnetic fields and similar effects cannot be obtained by the application of external electric fields. Based on this concept a molecular logic gate that processes two logic operations simultaneously is presented.

The rule of Inelastic scattering on the electrons dephasing is studied within the framework of non equilibrium Green's function formalism. A model which locally couples the conducting electrons to the vibrations of the device atoms is presented. Using the Born approximation we find that at the low coupling regime the magneto-conductance sensitivity increases. This behavior is opposite to the gate dependent conductance which becomes less sensitive to

changes in the gate potential when the coupling to the vibrations is turned on. Different coupling strengths and temperature dependence are studied.

Possibilities for further investigation in the directions of inelastic scattering effects in the high coupling regime, particles spin effects, and electron versus hole magneto-conductance are discussed.

Contents

II. INTRODUCTION

It was in 1959 that Richard Feynman, in his far-seeing lecture '**There's Plenty of Room at the Bottom**', realized that one of the most technologically promising and scientifically interesting unexplored field in physics involves the ability to manipulate and gain control over miniature structures:

'*... I would like to describe a field, in which little has been done, but in which an enormous amount can be done in principle. This field is not quite the same as the others in that it will not tell us much of fundamental physics ... but ... it might tell us much of great interest about the strange phenomena that occur in complex situations. Furthermore, a point that is most important is that it would have an enormous number of technical applications.*

What I want to talk about is the problem of manipulating and controlling things on a small scale. ...'

This call for multidisciplinary involvement in the study of the manufacturing and control at miniature length scales served to attract attention to a field which has since developed rapidly to be the cutting edge of technology and scientific interest these days.

Nevertheless, the chemical foundations of molecular electronics are considered, by field specialists[1], to be planted two decades ahead of Feynman's visionary statement. It was Mulliken[2] who in the late 1930's commenced studies on the spectroscopy of intra-molecular charge transfer. This led to a massively addressed research domain of Donor-Acceptor complexes charge transfer chemistry[3–10] which eventually set the foundation for the cornerstone of molecular electronics attributed to Aviram and Ratner[11]. In a novel theoretical prediction, made in 1974, they suggested that A Donor-Bridge-Acceptor type molecule could, in principle, act as a molecular rectifier. What designates this study is the fact that for the first time a **single molecule** was considered to act as an **electronic component** rather than just being a charge transfer medium. Therefore, it could serve as a potential building block for future miniature electronic devices. It should be noted that 25 years have passed before experimental evidence[12] of molecular rectification based on the Aviram-Ratner idea became available.

One of the most fundamental difficulties in the actual implementation of Aviram and Ratner's ideas was the inability to 'see' at the molecular scale. Without seeing it is impossible to create, characterize and examine such miniature devices. A major technological

breakthrough that suggested a solution to this problem was the invention of the Nobel prize awarded scanning tunneling microscope* in 1981† by H. Rohrer and G. Binnig[13,14], followed by several atomic resolution imaging technologies such as Atomic Force Microscopy[15]. These inventions allowed for the simultaneous and direct characterization, manipulation and tunneling current measurements of atomic and molecular species on well defined surfaces, enabling the design and investigation of the electronic properties of artificially created structures[16–18].

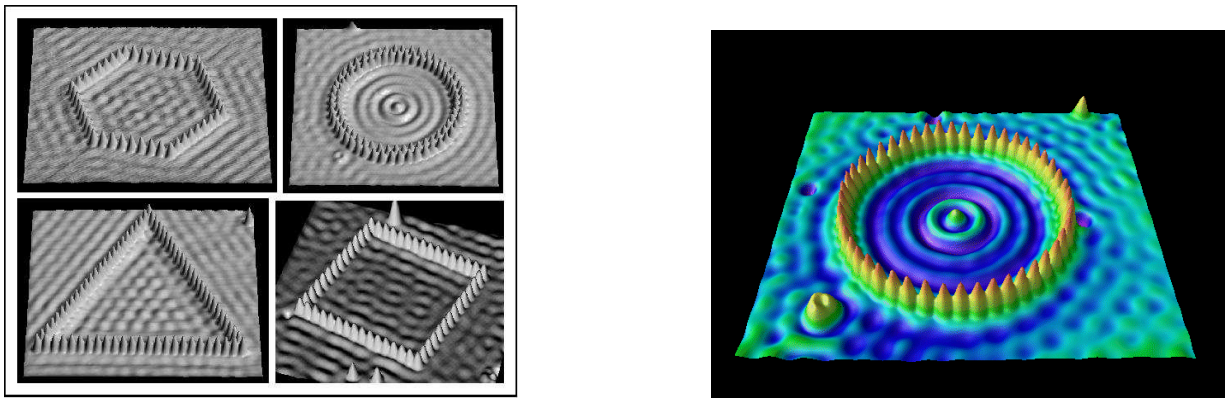

FIG. 1: Quantum corral structure made by STM tip manipulation of Iron atoms on a Copper (111) surface (taken from [19] and [16]).

Currently, single molecule electronics[20–31] is a rapidly growing scientific field. In recent years, a number of experimental techniques have been developed to synthesize molecular junctions and measure their conductance as a function of an externally applied bias. These technologies include mechanically controllable break junctions[32–35], electro-migration break junctions[36–38], electron beam lithography[39,40], shadow evaporation[41,42], electrochemical deposition[43–45], mercury droplet technologies[46–48], cross-wire tunnel junctions[49], STM[50,51] and conducting AFM[52] tip measurements, placing long nanowires on top of conducting electrodes[53], and additional methods[54].

These remarkable achievements allow for the construction of fundamental molecular devices and for the characterization of their electronic and electric properties. However, since

* which perhaps more appropriately should be referred to as a nanoscope rather than a microscope.

† Earlier attempts to build a similar device which were conducted by Russell Young of the U.S. National Bureau of Standards beginning at 1965 ended in failure due to unresolved vibrational issues.

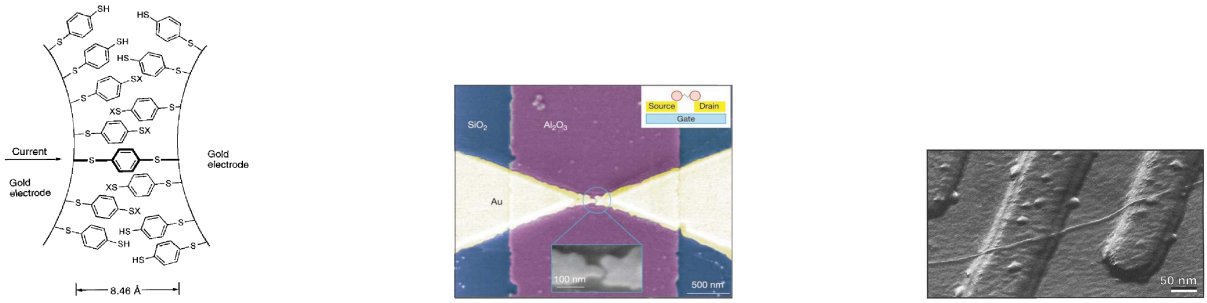

(a) **(b)** **(c)**

FIG. 2: Several examples of molecular junctions. (a) A schematic representation of a benzene-1,4-dithiolate molecule trapped in a mechanically controllable break junction (taken from [32]). (b) A $\sim$ 1nm gold junction formed by electro-migration technique on an aluminum oxide gate electrode (taken from [37]). (c) A carbon nanotube placed on a Si/SiO_2 substrate between two platinum electrodes (taken from [53]).

such technologies are still immature, they encounter fabrication and measurement reproducibility problems sometimes followed by harsh criticism[55].

Such experimental complexities accompanied by the accessibility to the utilization of highly precise and powerful computational methods (due to the smallness of the physical systems considered), make molecular electronics an extremely appealing theoretical field of research. This allows not only the clarification and understanding of existing experimental data but also the ability to predict and design of future molecular devices.

An important contribution to the theoretical investigation of electron current flow through molecular scale systems was made by Rolf Landauer[56] in 1957. Landauer directly related the conductance through a system, which is coupled to two leads, to the (energy dependent) probability amplitude of an electron approaching the system from one of the leads to be transmitted to the other lead. By this he effectively reduced the problem of coherent conductance to a well defined elastic scattering theory problem, thus giving a microscopic description of the conductance process. The utilization of Landauer's formalism with a combination of simple continuum/tight-binding[57–62] models or very sophisticated methods such as ab-initio based Green's function techniques[63–70] is the main tool for investigating the conductance through molecular systems up to this day. Recently, quantum dynamical approaches such as time dependent density functional theory investigations[71–75] and related

methods[76,77] were used for the evaluation of molecular conductance.

Interestingly, at the very same year that Feynman approached the scientific community with the urge to investigate the 'bottom', a seminal work by Yakir Aharonov and David Bohm[78] was published regarding the 'Significance of Electromagnetic Potentials in the Quantum Theory'[‡]. Using two gedanken-experimental setups, one involving electric fields and the other one magnetic fields, Aharonov and Bohm were able to prove that the fundamental entities in quantum mechanics are the electromagnetic potentials. Moreover, they have shown that electromagnetic fields or forces often considered in classical electrodynamics are not adequate from a full quantum mechanical point of view.

The main result of the Aharonov-Bohm (AB) theory is the fact that a charged particle is affected by electromagnetic fields even if they are applied in regions from which the particle itself is excluded. This was theoretically demonstrated for an electronic version of the double-slit experiment, in which a singular magnetic field is applied in the center point between the two slits and perpendicular to the plane of the electrons motion (see Fig. 4). Since the magnetic field is excluded from the electrons pathways, a classical charged particle would not feel its existence. However, a quantum mechanical particle is predicted to experience a phase shift. Due to the fact that the sign of this phase shift depends on whether the particle moves clockwise or counterclockwise in the magnetic field, an observable alternation in the interference pattern is obtained by the application of the magnetic field. This alternation is found to be periodic with a period proportional to the magnetic flux threading the circular electrons pathway. Therefore, allowing for the alternate switching of the interference pattern at a given point on the screen between constructive and destructive interference. It should be noted that since the treatment is based on interference effects it is required that the beam of incoming electrons would be coherent in such a sense that the momentum and the phase of the electrons would be well defined.

Shortly after their theoretical prediction, an experimental verification[80] using vacuum propagating electron waves was available for the AB effect. Nevertheless, even though a great deal of related experimental[81–95] and theoretical[96–103] studies have been conducted since, only a quarter of a century later a realization which seemed appropriate for electronic

[‡] Preliminary discussions considering the role of potentials in quantum mechanics can already be found as early as 1949.[79]

conductance switching was presented. Using a sub-micronic fabricated polycrystalline gold ring coupled to two conducting wires (see Fig. 3) and threaded by an external magnetic field at sub-Kelvin temperatures, Webb el al[104] were able to measure periodic magnetoresistance oscillations with a period of the order of $\sim 1 \times 10^{-2}$ Tesla and an amplitude of about 0.05Ω.

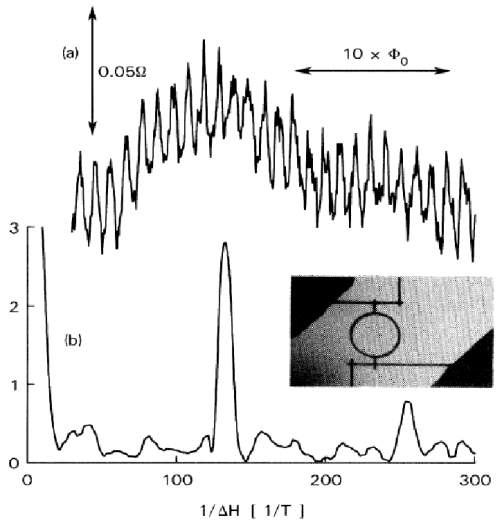

FIG. 3: Aharonov-Bohm magnetoresistance periodic oscillations measured for a polycrystalline gold ring with an inner diameter of 784 nm at a temperature of 0.01K (taken from [104]).

This setup can be viewed as a prototype of a sub-micronic field effect transistor in which the role of the gate control is taken by the external magnetic field. However, even at very low temperatures, such a micrometer scale ring cannot be considered as a coherent conductor. This provides an explanation to the fact that the amplitude of the AB oscillations, observed in Fig. 3 is quite damped.[105]

A natural goal, therefore, would be to miniaturize such a device and make it operable at length scales much smaller than the electrons decoherence length scales. One may naively conclude that the miniaturization of an AB interferometer, based on the setup created by Webb et al,[104] into the nanoscale is purely an engineering fabrication challenge. However, a fundamental physical limitation prevents the observation of the AB effect in the nanoscale. This limitation results from the fact that the period of the magnetoresistance oscillations is proportional to the magnetic **flux** threading the ring, as mentioned above. Therefore, the period of the oscillations for a ring with a diameter of the order of a single nanometer should

be six orders of magnitude larger than that of a micrometer scale ring. Considering the magnetoresistance oscillations measured by Webb et al for a micrometer ring, the predicted period of a nanometer scale ring is of the order of $\sim 1 \times 10^4$ Tesla - much larger than the magnetic field regime limit achievable in modern laboratories ($\sim 5 \times 10^1$ Tesla). Therefore, it is widely accepted that AB interferometry at the nanometer scale regime is not feasible.

Nevertheless, in recent years there have been several experimental realizations of magnetic field effects in nanometer scale structures. The major part of these regard Zeeman splitting of spin states in quantum dots[106] and in carbon nanotubes[53,107,108], and the Kondo effect measured for mesoscale quantum dots,[109,110] fullerenes,[111–114] and single molecules.[37,40] Other magnetic effects in quantum dots[115,116] and in carbon nanotubes[117] where also observed. Yet, most of these still involve basic physics research and are currently not aimed for technological applications.

In this context, it is important to remember that a major propellant for the ongoing development of nanotechnology is the strive to miniaturize current electronic devices in order to gain higher computational efficiency. Miniaturization limitations of current state of the art microelectronic technologies impel the advancement of alternatives. This is best expressed in a statement made by Mark Reed at the third international conference on molecular electronic devices, held at Arlington, Virginia, in October 1986:[1,118]

'*...The exponential growth in the semiconductor electronics industry is attributed to schemes that permit the physical downscaling of transistor-based ICs. This downscaling capability will eventually be brought to an end by the barriers of device scaling limits, interconnection saturation and yield. Achievement of limiting geometries from historical extrapolation will occur in the mid-1990s. If there is to be a post VLSI technology, it must employ simultaneously revolutionary solutions in design, architecture, and device physics to circumvent the interconnection problem. ...*'

This predicted breakdown of Moore's law, even though a decade later than Reed's prediction, is starting to be felt in current CPU performance advancement rates. Therefore, stressing the need to further invest scientific and technological efforts in the development and implementation of revolutionary ideas for future electronic devices based on nanotechnology and molecular electronics. An exceptional example for such novel efforts can be found in the fascinating and growing field of spintronics.[119–127] While in conventional electronics information is carried by the charge of electrons it is suggested that electrons spins can serve as

information carriers enabling faster and more efficient ways for data processing and storage.

The purpose of this thesis is to suggest a way to circumvent the intrinsic physical restriction that limits the utilization of magnetic interferometry to the micrometer scale, and to identify the physical conditions that enable the miniaturization of magnetoresistance electronic devices, based on such effects, to the nanometer/molecular scale. At that scale the clear advantages of coherent transport, quantum confinement and device reproducibility are expected to result in a pronounced effect. The essential procedure involves the **weak** coupling of the conducting leads to the interferometric ring, thus creating a resonant tunneling junction in which the conductance is allowed only through the narrow, doubly degenerate, energy levels of the ring. A gate voltage is used to tune the ring Fermi energy so that at a zero magnetic flux the conductance is high. The application of a relatively low (compared to the full AB period) external magnetic field, consequently shifts the narrow energy levels of the ring out of resonance and thus switches the conductance off. [§] Based on these principles, architectures that both mimic conventional electronics and allow for new computational schemes will be explored.

A. Thesis Outline

The next chapter is dedicated to the definition of the open question. A short mathematical description of the interactions of electrons with electromagnetic fields in the context of magnetoresistance interferometry is given in section III A. Within this description the major differences between the classical and the quantum mechanical treatment of external fields and potentials are stressed. The relevant length scales that set upper limits to the regime at which Aharonov-Bohm interferometry is feasible are discussed in section III B. Finally, in section III C the open question, studied in the subsequent chapters of the thesis, is defined.

In chapter IV a one-dimensional (1D) scattering theory continuum model of an AB interferometer is introduced. The model assumes that the charge carrying particles have well defined momentum and phase and that their transport along the interferometer is ballistic except for two well defined elastic scattering centers. This simplistic model allows the identification and isolation of the crucial physical parameters that allow the miniaturization of

[§] It should be mentioned that resonant tunneling has been previously utilized, through a different mechanism, as a sensitive probe in AB mesoscopic two dimensional electron gas experimental setups.[128–130]

magnetoresistance interferometric devices into the nanoscale.

The advantages of using magnetic fields in nanometer scale electronics are presented in chapter V. This is achieved by expanding the two-terminal continuum model, described in chapter IV, to the three terminal AB interferometer case. It is shown that the magnetic field polarity becomes an important control parameter which allows the selective switching of the conducting electrons outgoing channel. This behavior is found to be unique to magnetic fields due to their symmetry breaking nature.

After identifying and studying the conditions at which AB interferometry at the nanoscale is expected to be feasible using the simplistic physical continuum model, I turn in chapter VI to present the Magnetic Extended Hückel Theory (MEHT) atomistic model developed for the direct calculation of the conductance through molecular junctions under the influence of an externally applied magnetic field. In section VI A an outline of the essential non-equilibrium Green's function formalism relations required for the calculation of the conductance is given. At the limit of coherent transport, these equations are shown to reduce to the two terminal Landauer formula. The calculation of the Green's functions and self energies (SEs) appearing in the conductance formulas is discussed in section VI B. This is followed by an alternative route for the conductance calculation using absorbing potentials boundary conditions which is given in section VI C. All these calculations are based on the information gained from the electronic structure of the system. Section VI D is devoted to the electronic structure calculation of the different parts of the system. A description of the model Hamiltonian, based on the addition of the appropriate magnetic terms to the extended Hückel Hamiltonian, is given therein.

In chapter VII the MEHT calculation results are presented for three different molecular setups. First considered (VII A) is an atomic corral coupled to two atomic wires, placed on a semi-conductor surface, and threaded by a perpendicular magnetic field. This setup mostly resembles the 1D continuum model and the corresponding results are shown to be fully reproducible by a single parameter fit of the continuum model. Next, in section VII B, a nanometer scale molecular switch based on the AB effect in carbon nanotubes (CNTs) is presented. Two experimental setups are suggested: in the first a CNT is placed on an insulating surface in parallel with two conducting electrodes and in the second a CNT is placed on a conducting surface and approached by a STM tip from above. The conductance through the circumference of the CNT can then be controlled by the application of a mag-

netic field parallel to the main axis of the CNT. In section VII C a three terminal device composed of a polyaromatic hydrocarbon ring coupled to three gold atomic wires is studied. Similar to the predictions of the continuum model, it is found possible to control the outgoing route of the electrons by changing the polarity of the magnetic field. A truth table is constructed in which each of the outgoing channels processes a different logic operation simultaneously. To conclude this chapter an analysis of the temperature dependence of the reported calculation results is presented in section VII D.

An expansion of the atomistic calculations model to include inelastic scattering effects is presented in chapter VIII. In section VIII A the model Hamiltonian which includes inelastic scattering effects is presented. The corrections to the conductance formulas in the case of electron-vibrations interactions are given in section VIII B. Approximate ways to solve the many body problem involved in the conductance calculations are outlined in sections VIII C and VIII D. This is followed by the presentation of a truncation procedure, in section VIII E, which allows the reduction of the computational efforts considerably. It is shown that using this procedure the conductance calculation becomes independent of the size of the device.

In chapter IX the results of the atomistic calculations in the case of electron-vibrations interactions are given. First, the dependence of the zero-bias and zero magnetic field conductance through an atomic corral on an applied gate voltage is studied. A comparison between the case of pure coherent transport and the case of transport in the presence of electron-vibrations interactions is given, showing that the line-shape width is broadened due to the vibrational coupling. Similar results are obtained for a phenomenological model of a single level coupled to a single vibrational mode. Next we consider the magneto-conductance spectrum dependence on the vibrational coupling strength. We find that at a temperature of 1K the magneto-conductance becomes more sensitive to the applied magnetic field upon switching on the coupling with the vibrational modes of the molecule. A similar picture is found for a higher temperature of 10K.

Finally, a summary in which future directions are discussed is given in chapter X.

There are two appendices to this thesis. In appendix A we present, for the sake of completeness, the expression for the analytical evaluation of Slater type orbitals overlap integrals, which are used within the MEHT method. Appendix B is devoted to the development of the expansion of relevant magnetic integrals in terms of overlap integrals, allowing for the analytical evaluation of the MEHT magnetic terms as well.

III. DEFINING THE OPEN QUESTION

A. Basic concepts - Aharonov-Bohm interferometry

In classical mechanics the force exerted on a charged particle transversing a region in space which incorporates an electric and/or a magnetic field is given by the Lorentz force law $\mathbf{F} = q(\mathbf{E} + \mathbf{v} \times \mathbf{B})$, where q is the charge of the particle, $\mathbf{E}$ is the electric field, $\mathbf{v}$ is the particle's velocity, and $\mathbf{B}$ is the magnetic field. It can be seen that the electric field operates on a particle whether static or not and contributes a force parallel to its direction and proportional to its magnitude, while the magnetic field operates only on moving particles and contributes a force acting perpendicular to its direction and to the direction of the particles movement. When solving Newtons equation of motion $\mathbf{F} = \frac{d\mathbf{P}}{dt}$, the resulting trajectories for a classical charged particle entering a region of a uniform magnetic field will thus be circular. We can define scalar and vectorial potentials using the following definitions $\mathbf{E}(\mathbf{r}, t) = -\nabla V - \frac{\partial \mathbf{A}(\mathbf{r},t)}{\partial t}$ and $\mathbf{B}(\mathbf{r}, t) = \nabla \times \mathbf{A}(\mathbf{r}, t)$, respectively. When defining the following Lagrangian $L = \frac{1}{2}m\mathbf{v}^2 - qV(\mathbf{r}) + q\mathbf{v} \cdot \mathbf{A}$, and deriving the canonical momentum using the relation $\mathbf{P}_i = \frac{\partial L}{\partial \dot{\mathbf{r}}_i}$ one can, in principle, solve the Euler-Lagrange or Hamilton equations of motion. This procedure, even though easier to solve for some physical problems, is absolutely equivalent to solving Newton equations of motion and will produce the exact same trajectories.

The influence of electric and magnetic fields on the dynamics of quantum charged particles was investigated by Aharonov and Bohm in a seminal work from 1959[78] revealing one of the fundamental differences between the classical and the quantum description of nature. According to Aharonov and Bohm, while in classical mechanics the transition from using electric and magnetic fields to using scalar and vectorial potentials is "cosmetic" and may be regarded as a mathematical pathway for solving equivalent problems, in quantum mechanics the fundamental quantities are the potentials themselves.

In order to demonstrate this principle consider a double-slit experiment applied to electrons as seen in Fig. 4. The experimental setup consists of a source emitting coherent electrons which are diffracted through two slits embedded in a screen. The electron intensity is measured in a detector placed on the opposite side of the screen. In the absence of a magnetic field the intensity measured by the detector when placed directly opposite to the

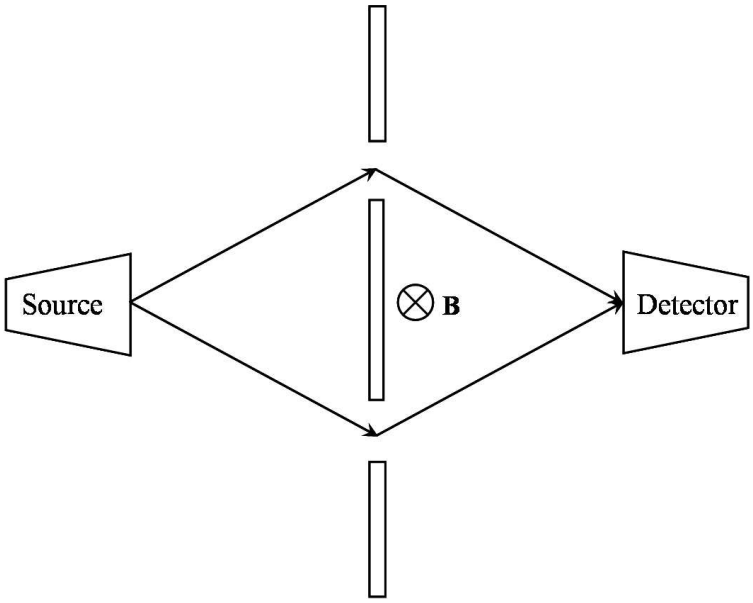

FIG. 4: The Aharonov-Bohm double-slit experiment setup for charged particles.

source will be maximal due to the positive interference between the two electron pathways which are of equal length. When applying a point magnetic field perpendicular to the interference plane, as indicated in Fig. 4, the interference intensity is altered. Unlike the classical prediction, this change in the interference pattern is expected even if the magnetic field is excluded from both electron pathways. This can be traced back to the fact that even tough the magnetic field is zero along these pathways, the corresponding vector potential does not necessarily vanish at these regions.

In order to give a more quantitative description of this phenomena we consider an analogous model consisting of a ring shaped ballistic conductor forcing the bound electrons to move in a circular motion connecting the source and the detector as shown in Fig. 5.

The Hamiltonian of the electrons under the influence of electric and magnetic potentials [¶] is given by:

$$\hat{H} = \frac{1}{2m}\left[\hat{\mathbf{P}} - q\mathbf{A}(\hat{\mathbf{r}})\right]^2 + \hat{V}(\hat{\mathbf{r}}). \tag{1}$$

Here m is the mass of the particle, $\hat{\mathbf{P}} = -i\hbar\hat{\nabla}$ is the canonical momentum operator, and $\hbar$ is Plank's constant divided by 2π. In the absence of electrostatic interactions, the Hamiltonian

[¶] Field quantization is disregarded in the entire treatment and we assume that the potentials are time independent.

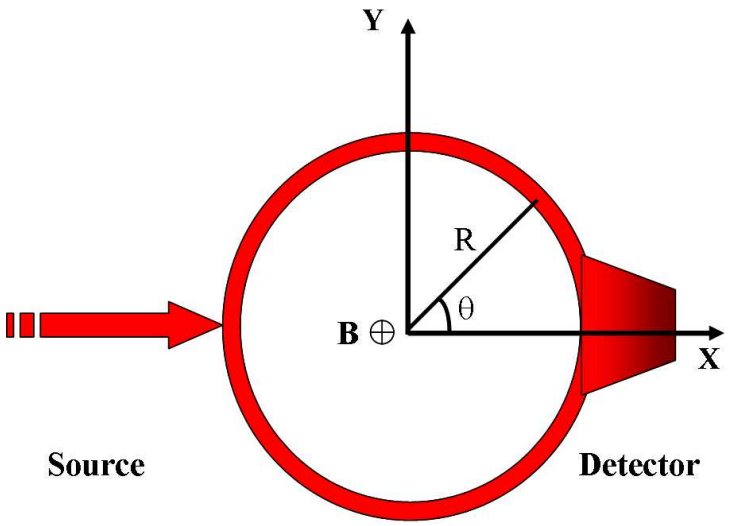

FIG. 5: An Aharonov-Bohm ring shaped interferometer connecting a coherent electron source and a detector.

reduces to the free particle Hamiltonian with the appropriate kinetic momentum operator $\tilde{\hat{\mathbf{P}}} = \hat{\mathbf{P}} - \mathbf{qA}(\hat{\mathbf{r}})$.

In the setup shown in Fig. 5 the wave function splits into two distinct parts, one traveling through the upper arm and the other through the lower arm of the ring. Since the magnetic field is excluded from these paths ($\nabla \times \mathbf{A} = 0$) and both are simply connected in space, it is possible to write a solution to the stationary Schrödinger equation with this Hamiltonian at each path as follows:

$$\Psi^{u/d} = e^{i\int_{u/d}(\mathbf{k}-\frac{q}{\hbar}\mathbf{A})\cdot\mathbf{dl}}, \tag{2}$$

where $\mathbf{k}$ is the wave-vector of the charged particle and the integration is taken along its pathway. Due to the circular symmetry of the system it is useful to transform to polar coordinates where $R = \sqrt{x^2+y^2}$ is the radius of the ring and $tg(\theta) = \frac{y}{x}$. Using the polar form of the differential along the circular path $\mathbf{dl} = Rd(\cos(\theta), \sin(\theta), 0) = R(-\sin(\theta), \cos(\theta), 0)d\theta$, the spatial phase factor accumulated by an electron traveling along the upper or the lower branches of the ring can be easily calculated in the following manner:

$$\Phi_k = \int_{\pi}^{0} \mathbf{k}\cdot\mathbf{dl} = \pi Rk. \tag{3}$$

Here $\mathbf{k}$ is taken to be along the ring, and $k = |\mathbf{k}|$ is the wavenumber of the electron.

When a uniform** magnetic field is applied perpendicular to the cross section of the ring, $\mathbf{B} = (0, 0, B_z)$, the vector potential may be written as $\mathbf{A} = -\frac{1}{2}\mathbf{r} \times \mathbf{B} = \frac{1}{2}B_z(-y, x, 0) = \frac{RB_z}{2}(-\sin(\theta), \cos(\theta), 0)$. Thus, the magnetic phase accumulated by the electron while traveling from the source to the detector in a clockwise manner through the upper path is given by:

$$\Phi_m^u = -\frac{q}{\hbar}\int_{\pi}^{0} \mathbf{A} \cdot \mathbf{dl} = \pi\frac{\phi}{\phi_0}. \tag{4}$$

Here, $\phi = B_z S$ is the magnetic flux threading the ring, $\phi_0 = \frac{h}{q}$ is the flux quantum, and $S = \pi R^2$ is the cross section area of the ring. For an electron traveling through the lower path in a counterclockwise manner the magnetic phase has the same magnitude however an opposite sign:

$$\Phi_m^l = -\frac{q}{\hbar}\int_{\pi}^{2\pi} \mathbf{A} \cdot \mathbf{dl} = -\pi\frac{\phi}{\phi_0}. \tag{5}$$

The electron intensity measured at the detector is proportional to the square absolute value of the sum of the upper and lower wave function contributions:

$$I \propto \left|\Psi^u + \Psi^d\right|^2 = \left|e^{i\pi\left(Rk+\frac{\phi}{\phi_0}\right)} + e^{i\pi\left(Rk-\frac{\phi}{\phi_0}\right)}\right|^2 = 2\left[1 + \cos\left(2\pi\frac{\phi}{\phi_0}\right)\right]. \tag{6}$$

Thus, we find that the intensity measured at the detector is a **periodic** function of the magnetic **flux** threading the ring's cross section. As mentioned before, this general and important result holds also when the magnetic field is not applied uniformly and measurable intensity changes may be observed at the detector even if the magnetic field applied is excluded from the circumference of the ring to which the electrons are bound.

B. Length Scales

The model described above presents an idealized system for which the charge carrying particles travel from the source to the detector without losing either momentum or phase. When considering the issue of measuring the AB effect in a realistic system, a delicate

** The calculation given here assumes a uniform magnetic field even-though, it was claimed that Eq. 2 holds only in regions in space where $\mathbf{B} = 0$. Nevertheless, due to the fact that the electrons are confined to move on the one-dimensional ring, there is no essential difference between the case of a singular magnetic field and a homogeneous magnetic field. Therefore, the usage of the phases calculated here in Eq. 6 is valid. Furthermore, it should be noted that due to Stokes law, the line integration of $\mathbf{A}$ over a closed loop will always give the magnetic flux threading the ring whether the field is uniform, singular or of any other form.

balance between three important length scales is needed: 1. the Fermi electrons de-Broglie wave length, 2. the mean free path, and 3. the coherence length scale. We shall now give a brief description of each of these length scales and its importance in coherent transport problems.

1. Fermi de-Broglie wave length

As in the optical double-slit experiment, the wavelength of the conducting electrons determines the interference intensity measured at the detector. At low temperatures the net current is carried by electrons in the vicinity of the Fermi energy and thus by controlling their wavelength one can determine whether positive or negative interference will be measured at the detector in the absence of a magnetic field.

In order to achieve positive interference, an integer number of Fermi wave lengths should fit into half the circumference of the ring (Fig. 5): $L = n\lambda_F$. Here, n is an integer, $L = \pi R$ is half of the circumference of the ring, and λ_F is the Fermi electrons wavelength given by the well know de-Broglie relation $\lambda_F = \frac{h}{P_F} = \frac{2\pi}{k_F}$, where, P_F is the momentum of the Fermi electrons, and k_F is the associated wavenumber.

For such a condition to be experimentally accessible, the Fermi wavelength should approximately be of the order of magnitude of the device dimensions. Too short wavelengths will give rise to extreme sensitivity of the interference pattern on the Fermi wavenumber, while too long wavelengths will show very low sensitivity.

We shall return to the importance of controlling the wavelength of the conducting electrons in realistic systems measurements in chapters IV and VII.

2. Mean free path

An electron traveling in a perfect crystal can be viewed as a free particle with a renormalized mass.[131] This mass, which is usually referred to as the effective mass of the electrons in the crystal, incorporates the net effect of the periodic nuclei array on the conducting electrons. When impurities or defects exist in the crystalline structure the electrons may scatter upon them. Such scattering implies a random change in the electron's momentum and thus destroys the ballistic nature of the conductance. The mean free path is the average distance

an electron travels before its momentum is randomized due to a collision with an impurity. If the scattering taking place at the impurities sites is **elastic**, such that the electron's energy and the magnitude of its momentum are conserved and only the direction of the momentum is randomized then for a given trajectory a stationary interference pattern will be observed. However, different electron trajectories will give rise to different interference intensities and the overall interference pattern will not be stationary and thus will be averaged to zero. Therefore, in order to be able to observe coherent phenomena the dimension of the system under consideration should not exceed the typical mean free path of the charge carrying particles within it at the given temperature.

3. Coherence length scale

Inelastic scattering may occur when the impurities have internal degrees of freedom which may exchange energy with the scattered electrons. Such scattering events alter the phase of the conducting electron. AB interferometry requires that a constant phase difference exists between the trajectories of electrons moving in the upper and the lower arms of the interferometer ring. Thus, for stationary inelastic scatterers which shift the phase of the electrons in a persistent manner, a constant interference pattern will be measured at the detector. Although the intensity at zero magnetic field will not necessarily be at its maximal value, AB oscillations will be observed. When the scatterers are not stationary, and the phase shifts they induce are not correlated between the two arms of the ring, the coherent nature of the conductance is destroyed and the AB interference pattern is wiped out. Apart from impurities, inelastic scattering may occur due to electron-phonon processes, and electron-electron interactions. The later conserve the total energy but allow energy exchange and thus phase randomization.

C. The open question

As mentioned above, the design of a realistic AB interferometer requires a careful consideration of the typical length scales of the conducting electrons. In order to measure a significant AB periodicity it is necessary to reduce the dimensions of the interferometer beneath the momentum and phase relaxation length scales and make it comparable to

the de-Broglie wave length. As an example, for a micrometer scale GaAs/AlGaAs based two-dimensional electron gas ring the expected AB periodicity is of the order of milliTesla: $\frac{h}{q\pi R^2} \approx 1 \cdot 10^{-3}$Tesla. However, the typical de-Broglie wave length is of the order of ~ 30nm, and the mean free path (momentum relaxation length scale) is three orders of magnitude larger ($\sim 30\mu$m) while the phase relaxation length is $\sim 1\mu$m [††]. Therefore, due to momentum relaxation and dephasing processes, which take place on the same scale of the ring dimensions, the amplitude of the AB oscillations is considerably damped and any realistic implementation is hence impractical. As a result, we are compelled to consider nanometer sized molecular based AB interferometers. Since two molecules of the same material are, by definition, identical defects or impurities in such devices do not exist and the only source of phase relaxation is the exchange of energy with the vibrational degrees of freedom of the molecule. Thus, at low enough temperatures at which such scattering is suppressed the transport through the molecule is coherent and significant AB oscillations are expected to be measured.

A very important advantage of miniaturizing the interferometer is that the transport can be directed to a single, preselected energy level on the ring. Due to quantum confinement effects the energy spacing of the levels on the ring scales as $\frac{(2n+1)\hbar^2}{2m^\star R^2}$ where n is the quantum number of the conducting electron, and $m^\star$ is its effective mass. When the radius of the ring is reduced from the micrometer scale into the nanometer scale, the energy spacing is increased by six orders of magnitude for a given quantum number. Consequently, instead of transmitting through a finite density of states which characterizes the Fermi electrons in micrometer scale devices, it is possible to transmit through a single, well defined, energy level on the ring. Therefore, reducing effects resulting from heterogeneous broadening and remaining with the homogeneous broadening of the single level due to its coupling to the leads or to the vibrational modes of the ring. In this case the conductance becomes less sensitive to temperature effects.

Nevertheless, on top of the engineering challenge of fabricating such small and accurate devices, another substantial physical limitation jeopardizes the whole concept. When considering a nanometer sized AB loop the period of the magnetic interference oscillations increases

[††] It should be mentioned that both the mean free path and the phase relaxation length exhibit strong temperature dependence.

considerably and becomes comparable to $\frac{h}{q\pi R^2} \approx 1 \cdot 10^3$Tesla. Magnetic fields of these orders of magnitude are, by far, not accessible experimentally and thus AB interferometry is not expected to be measured for miniaturized circular systems.

Therefore, a question to be raised is whether electronic devices based on the AB effect can be scaled down to the molecular/nanometric level, in which transport is expected to be coherent, even though the full AB periodicity is achieved at irrationally high magnetic fields?

The purpose of the next chapter is to present the basic physical principles that set the path to overcome the above mentioned limitation and allow for the design of miniaturized electronic devices based on the AB effect.

IV. CONTINUUM MODEL

In the last chapter we have introduced the concept of the AB periodicity in magnetic interferometers of charged particles. The interference intensity was shown to be proportional to the magnetic flux threading the circular path linking the source of coherent electron and the detector (see Fig. 5). This periodicity, which is robust to all AB setups, is determined solely by the charge of the conducting entities and by the dimensions of the interferometer. It was claimed that for a nanometer scale conducting loop, the magnetic fields needed to complete a full AB cycle are irrationally high and thus no AB interferometry is possible at such miniaturized devices.

It is the goal of this chapter to show how this argumentation is only partially correct. Even though it is true that the full AB cycle for nanometer sized conducting loops is accomplished at extremely high magnetic fields, the dependence found in Eq. 6, can be modified such that very high sensitivity of the interference intensity is achieved upon the application of reasonably low magnetic field.

For this purpose we shall now introduce a simplified continuum model[63,97–100,103,132–135] description of an AB interferometer. The model consists of a one dimensional (1D) single mode conducting ring coupled to two 1D single mode conducting leads as depicted in Fig. 6. The transport is considered to be ballistic along the conducting lines. Elastic scattering occurs at the two junctions only.

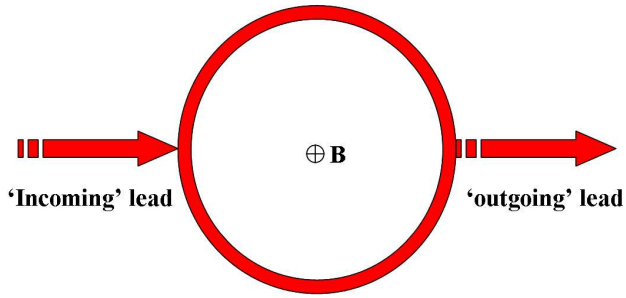

FIG. 6: An illustration of a 1D coherent transport continuum model of an AB interferometer.

Even-though this model neglects important effects such as electron-electron interactions, and electron-phonon coupling, and also disregards the detailed electronic structure of the molecular device, and the exact leads-device junctions structure, it succeeds in capturing the important physical parameters needed to control the profile of the AB period.

The main feature differing the current arrangement from the one shown in Fig. 5, is that an 'outgoing' lead replaces the absorbing detector. Hence, the interference intensity measured at the detector is replaced by a measurement of the conductance between the two leads through the ring. Although it might seem insignificant, this difference is actually the heart of our approach to control the shape of the AB period. In the original setting, an electron arriving at the detector is immediately absorbed and therefore the intensity measured is the outcome of the interference of the two distinct pathways the electron can travel. For the setup considered in Fig. 6 an electron approaching each of the junctions can be either transmitted into the corresponding lead or be reflected back into one of the arms of the ring. Consequently, the conductance through the device is a result of the interference of an infinite series of pathways resulting from multiple scattering events of the electron at the junctions. It is obvious that the behavior predicted by Eq. 6 has to be modified to account for the interference between all pathways.

A scattering matrix approach[63,100,132–134,136,137] can be now used in order to give a quantitative description of the present model. Within this approach we first label each part of the wave function on every conducting wire with a different amplitude which designates its traveling direction. As can be seen in Fig. 7, L_1 marks the right going amplitude of the

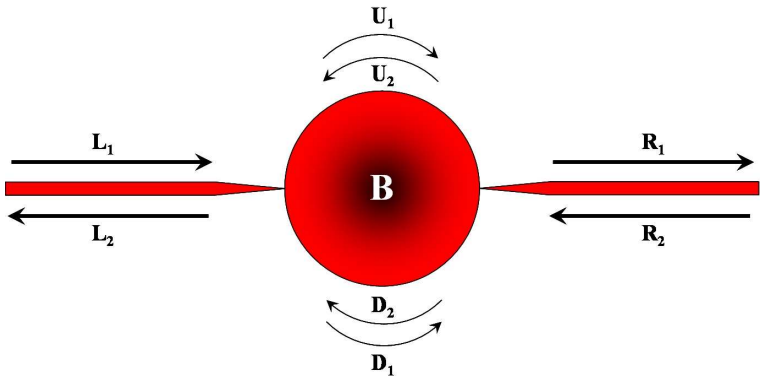

FIG. 7: An illustration of the amplitudes of the different parts of the wave function in the 1D continuum model.

wave function on the left lead, while L_2 - denotes the left going amplitude on the same lead. Similarly, R_1 and R_2 stand for the right and left going wave amplitudes on the right lead, respectively. For the upper arm of the ring U_1 and U_2 represent the clockwise and

counterclockwise traveling amplitudes, respectively, whereas D_2 and D_1 are the clockwise and counterclockwise traveling amplitudes on the lower arm.

Next, each junction is assigned with appropriate scattering amplitudes. In what follows we assume that the junctions are identical. As can be seen in Fig. 8, a- is the probability

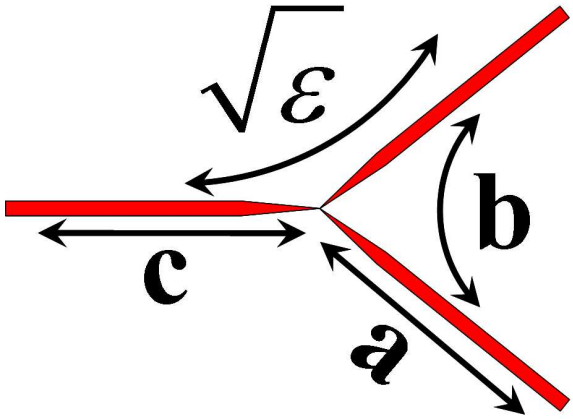

FIG. 8: An illustration of the junction scattering amplitudes in the 1D continuum model.

amplitude for an electron approaching the junction from one of the arms of the ring to be reflected back into the same arm, while b- is the probability amplitude to be transmitted from one arm of the ring to the other upon scattering at the junction. c - is the probability amplitude for an electron approaching the junction from the lead to be reflected back into the lead, and $\sqrt{\epsilon}$ is its probability amplitude to be transmitted to (or out of) either arms of the ring.

For each junction it is now possible to formulate a scattering matrix equation relating the outgoing wave amplitudes to the incoming wave amplitudes. For the left junction we get:

$$\begin{pmatrix} L_2 \\ U_1 \\ D_1 \end{pmatrix} = \begin{pmatrix} c & \sqrt{\epsilon} & \sqrt{\epsilon} \\ \sqrt{\epsilon} & a & b \\ \sqrt{\epsilon} & b & a \end{pmatrix} \begin{pmatrix} L_1 \\ U_2 e^{i\Phi_1} \\ D_2 e^{i\Phi_2} \end{pmatrix}. \tag{7}$$

Here $\Phi_1 = \Phi_k - \Phi_m$ is the phase accumulated by an electron traveling from the right junction to the left junction through the upper arm of the ring, and $\Phi_2 = \Phi_k + \Phi_m$ is the corresponding phase accumulated along the lower arm of the ring. Φ_k and $\Phi_m \equiv \Phi_m^u$ are defined in Eqs. 3

and 4, respectively. An analogous equation can be written down for the right junction:

$$\begin{pmatrix} R_1 \\ U_2 \\ D_2 \end{pmatrix} = \begin{pmatrix} c & \sqrt{\epsilon} & \sqrt{\epsilon} \\ \sqrt{\epsilon} & a & b \\ \sqrt{\epsilon} & b & a \end{pmatrix} \begin{pmatrix} R_2 \\ U_1 e^{i\Phi_2} \\ D_1 e^{i\Phi_1} \end{pmatrix}. \tag{8}$$

In order to insure current conservation during each scattering event at the junctions one has to enforce the scattering matrix to be unitary. This condition produces the following relations between the junction scattering amplitudes: $a = \frac{1}{2}(1-c)$, $b = -\frac{1}{2}(1+c)$, and $c = \sqrt{1-2\epsilon}$. It can be seen that the entire effect of the elastic scattering occurring at the junctions can be represented by a single parameter which we choose to be ϵ - the junction transmittance probability.

Solving these equations [‡‡] and setting the right incoming wave amplitude R_2 equal to zero, one gets a relation between the outgoing wave amplitude R_1 and the incoming wave amplitude L_1. Using this relation it is possible to calculate the transmittance probability through the ring which is given by:[138]

$$T = \left|\frac{R_1}{L_1}\right|^2 = \frac{A[1+\cos(2\phi_m)]}{1+P\cos(2\phi_m)+Q\cos^2(2\phi_m)}, \tag{9}$$

where the coefficients are functions of the spatial phase and the junction transmittance probability:

$$\begin{cases} A = \frac{16\epsilon^2[1-\cos(2\Phi_k)]}{R} \\ P = \frac{2(c-1)^2(c+1)^2-4(c^2+1)(c+1)^2\cos(2\Phi_k)}{R} \\ Q = \frac{(c+1)^4}{R} \\ R = (c-1)^4 + 4c^4 + 4 - 4(c^2+1)(c-1)^2\cos(2\Phi_k) + 8c^2\cos(4\Phi_k). \end{cases} \tag{10}$$

The numerator of Eq. 9 resembles the result obtained for the interference of two distinct electron pathways (given by Eq. 6). The correction for the case where the electrons are not absorbed at the detector is given by the coefficient A and the denominator expression.

Two important independent parameters contribute to the shape of the magneto-transmittance spectrum: the junction transmittance probability - ϵ, and the conducting

[‡‡] It is useful to initially solve the four equations involving the on-ring amplitudes U_1, U_2, D_1, and D_2 as a function of the leads incoming amplitudes L_1, and R_2. Plugging the solution into the equation for the outgoing amplitude R_1 results in the desired relation between R_1 and L_1, needed for the transmittance calculation.

electron wavenumber k appearing in the spatial phase $\Phi_k = \pi Rk$. In Fig. 9 we present the transmittance probability (T) through the ring as a function of the normalized magnetic flux threading it, for a given value of the spatial phase and several junction transmittance probabilities. It can be seen that for high values of the junction transmittance probability

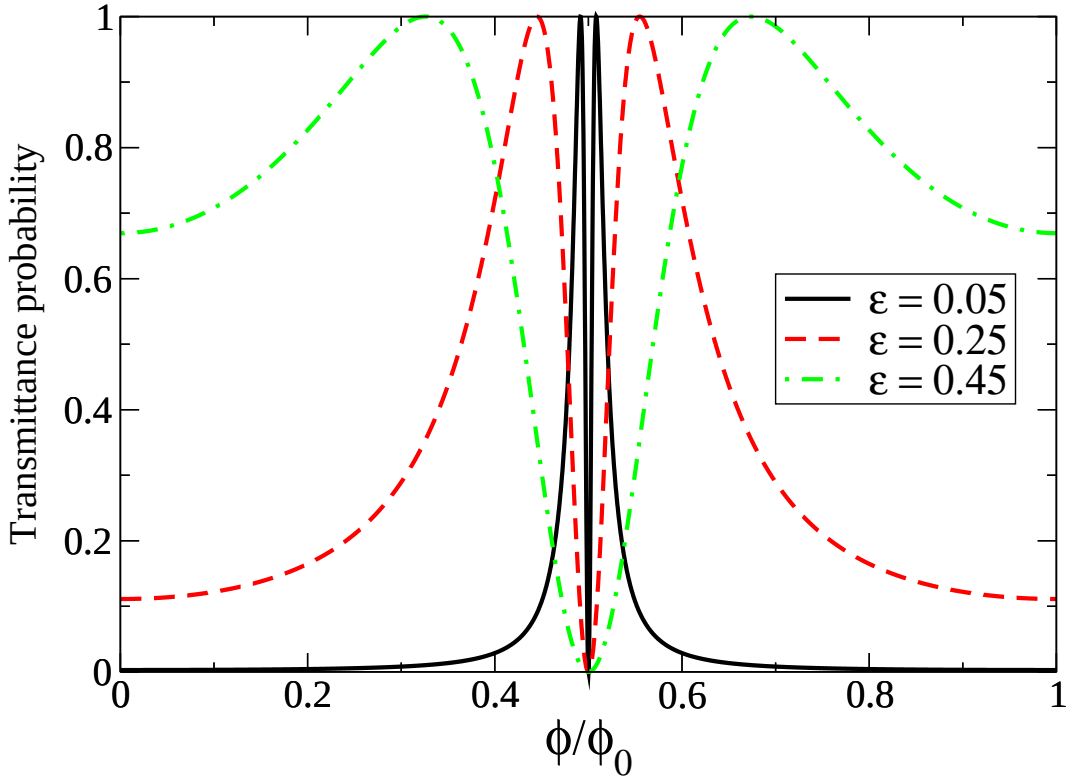

FIG. 9: AB transmittance probability, calculated using Eqs. 9 and 10, as a function of the magnetic flux for different junction transmittance probabilities and $kR = 0.5$. For high values of ϵ (dash-dotted green line) the transmittance probability is similar to that predicted by Eq. 6. As ϵ is decreased the transmittance peaks narrow (dashed red line). For very small values of ϵ the peaks become δ function-like (full black line).

(dashed-dotted green line in the figure) the magneto-transmittance behavior is similar to that predicted by Eq. 6, i.e. a cosine function. As ϵ is reduced from its maximal value of $\frac{1}{2}$ the width of the transmittance peaks is narrowed (dashed red line and full black line). At the limit of vanishing ϵ the magneto-transmittance peaks become a sharp δ function. Physically, this can be explained based on the fact that ϵ controls the coupling between the leads and the ring. High values of ϵ correspond to a high probability of the electron to mount (or dismount) the ring and thus, relate to strong leads-ring coupling. At such values, the

lifetime of the electron on the ring is short and therefore, the energy levels characterizing the ring are significantly broadened. The application of a magnetic field will change the position of these energy levels, however, due to their wide nature they will stay in partial resonance with the energy of the incoming electrons for a wide range of magnetic fields. When reducing the coupling (low values of ϵ) the doubly degenerate energy levels of the ring sharpen. If we assume that at zero magnetic flux two such energy levels are in resonance with the incoming electrons, then upon applying a finite magnetic field the degeneracy is removed such that one level has its energy raised and the other lowered. This splitting causes both sharp energy levels to shift out of resonance and thus reduces the transmittance probability through the ring dramatically. The situation described above for the low coupling regime is, in fact, resonant tunneling occurring through the slightly broadened (due to the coupling to the leads) energy levels of a particle on a ring. Here, the free particle [§§] time-independent scattering wave function on the wires, $\psi_k(z) = e^{ikz}$, has the same form of the wave function of a particle on a ring $\psi_m(\theta) = e^{im\theta}$ where $m = 0, \pm 1, \pm 2, \ldots$. Upon mounting the ring, the electron's wave number, k_m, is quantized according to the following relation: $Rk_m = m$. The value of m for which resonant tunneling takes place is determined by the condition that the kinetic energy of the free electron on the wire equals a sharp energy eigenvalues of the ring[139]:

$$\frac{\hbar^2 k^2}{2m^\star} = \frac{\hbar^2 (m - \frac{\phi}{\phi_0})^2}{2m^\star R^2}. \tag{11}$$

In order to achieve resonance one has to require that $k = (m - \frac{\phi}{\phi_0})/R$. A slight change in the magnetic flux, disrupts this resonance condition and reduces the transmittance considerably. For different values of the wavenumber on the leads the resonance condition in Eq. 11 will be obtained at different values of the magnetic flux.

This effect is depicted in Fig. 10 where the transmittance probability is plotted against the normalized magnetic flux threading the ring, for a given value of ϵ and several spatial phase factors. As depicted in the figure, changing the spatial phase results in a shift of the location of the transmittance peaks along the AB period. This is analogous to the change in the position of the intensity peaks of the interference pattern observed in the optical double-

[§§] It should be emphasized that the validity of effective mass models for the description of nanometer scale systems may be very limited and it is presented here merely to give some physical intuition of some of the main features obtained by the continuum model.

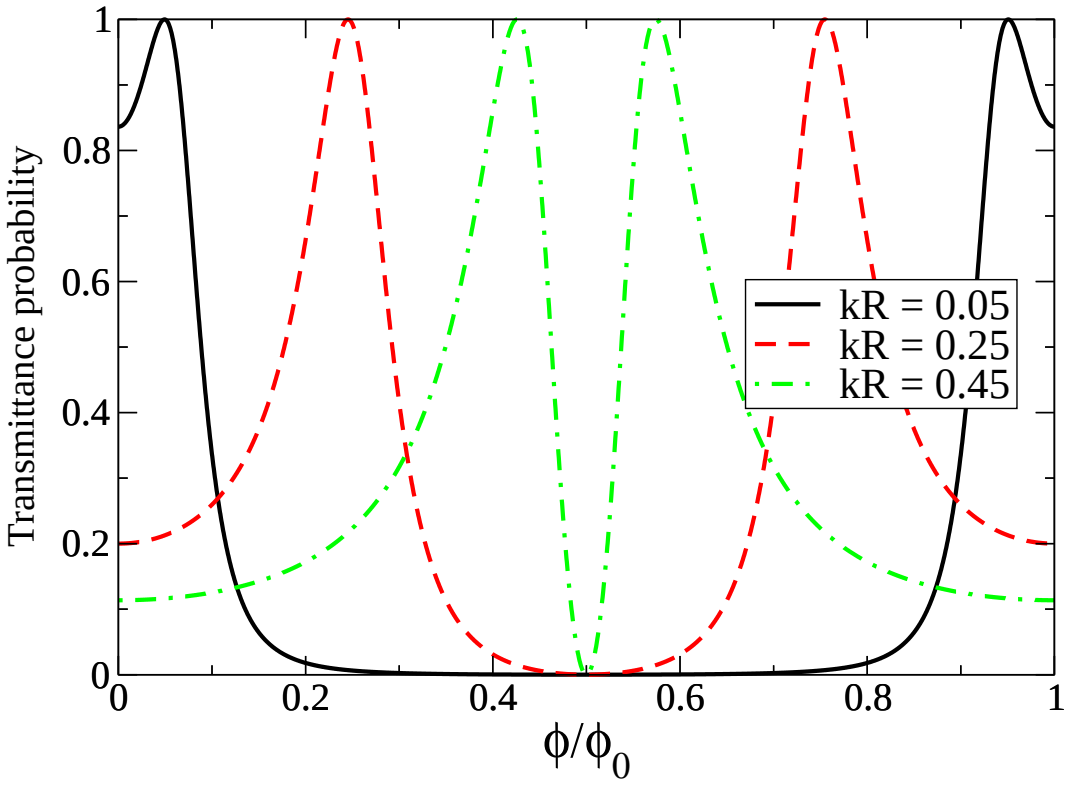

FIG. 10: AB transmittance probability as a function of the magnetic flux for different spatial phases and $\epsilon = 0.25$. By changing the value of kR from $\sim n$ (dashed-dotted green line) to $\sim n + 0.5$ (Full black line), where n is an integer, it is possible to shift the transmittance peaks from the center of the AB period to its edges, respectively.

slit experiment when varying the wavelength of the photons. For kR values of $\sim 0, 1, 2, \cdots$ (dashed-dotted green line in the figure) the peaks are located near the center of the AB period, while for values of $\sim 0.5, 1.5, 2.5, \cdots$ the peaks are shifted toward the period's lower and higher edges (Full black line). In a realistic system such control can be achieved by the application of a gate field that serves to accelerate (or decelerate) the electron as it mounts the ring. The gate potential, V_g, thus modifies the resonance condition of Eq. 11 to:

$$\frac{\hbar^2 k^2}{2m^\star} = \frac{\hbar^2 (m - \frac{\phi}{\phi_0})^2}{2m^\star R^2} + V_g. \tag{12}$$

Eq. 12 implies that a change in the gate potential influences the magnetic flux at which resonance is attained. Therefore, the transmittance resonances position along the AB period can be varied as shown in Fig. 10.

Considering the original goal of measuring AB magneto-transmittance effects in nanome-

ter scale interferometers, we see that even though the full AB period is out of experimental reach, a delicate combination of an appropriate conducting electrons **wavenumber** and **weak** leads-ring coupling, enables to **shift** the transmittance peak toward the low magnetic fields regime while at the same time dramatically increase the **sensitivity** to the external magnetic field.

This important result is depicted in Fig. 11, where magnetic switching for a 1nm radius ring is obtained at a magnetic field of ~ 1 Tesla while the full AB period (see inset of the figure) is achieved at magnetic fields orders of magnitude larger.

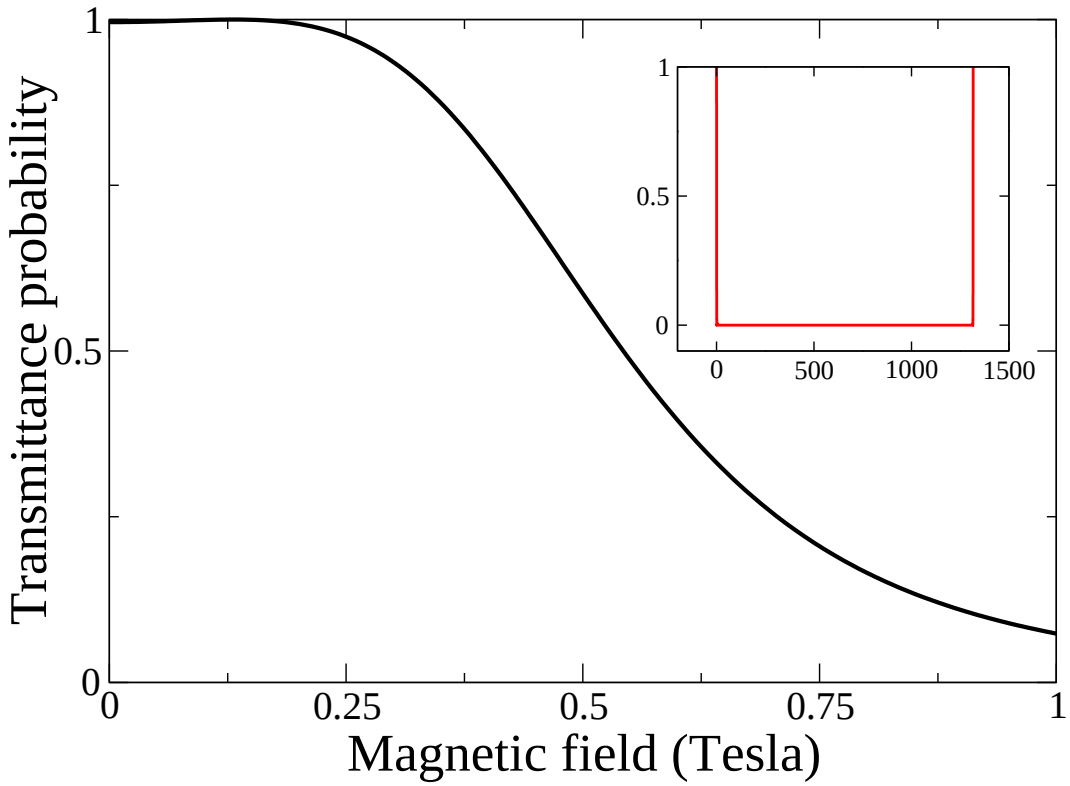

FIG. 11: Low field magnetoresistance switching of a 1nm ring weakly coupled to two conducting wires as calculated using the continuum model. The parameters chosen in this calculation are: $\epsilon = 0.005$, and $kR \approx 1$. Inset showing the full AB period of ≈ 1300 Tesla.

This result resembles the change in the interference intensity measured by the optical Mach-Zehnder interferometer upon altering the phase of the photons on one of the interferometric paths. The plausibility of applying these principles to realistic molecular systems is the subject of chapters VI and VII. But first, an important question, which considers the uniqueness of using magnetic fields, has to be answered.

V. WHY USE MAGNETIC FIELDS?

In the previous chapter we have identified the important physical parameters that have to be taken into account when considering the utilization of nanostructures as magnetoresistance devices based on the AB effect. A legitimate question that may be raised at this point is why use magnetic fields to switch the conductance, while switching devices based on other external perturbations, such as field effect transistors (FETs), already exist and operate even at the molecular scale[140–144]?

In order to address this question it is useful to consider an expansion of the two terminal continuum model described in chapter IV to the three terminal case.[145] An illustration of the three terminal setup is given in Fig. 12

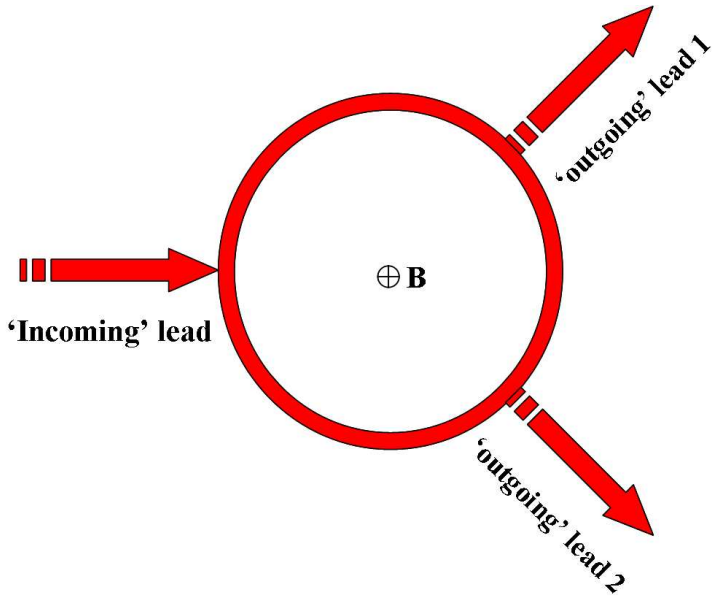

FIG. 12: An illustration of a 1D coherent transport continuum model of a three terminal AB interferometer.

The scattering matrix approach may be used in a similar manner to that described for the two terminal setup. An illustration of the three-terminal setup parameters designation is given in Fig. 13. We denote (panel (a)) by α, β, and $\gamma = 2\pi - \alpha - \beta$ the angles between the three conducting leads. Similar to the two terminal model, we label the wave amplitudes on each ballistic conductor of the system as shown in panel (b) of Fig. 13.

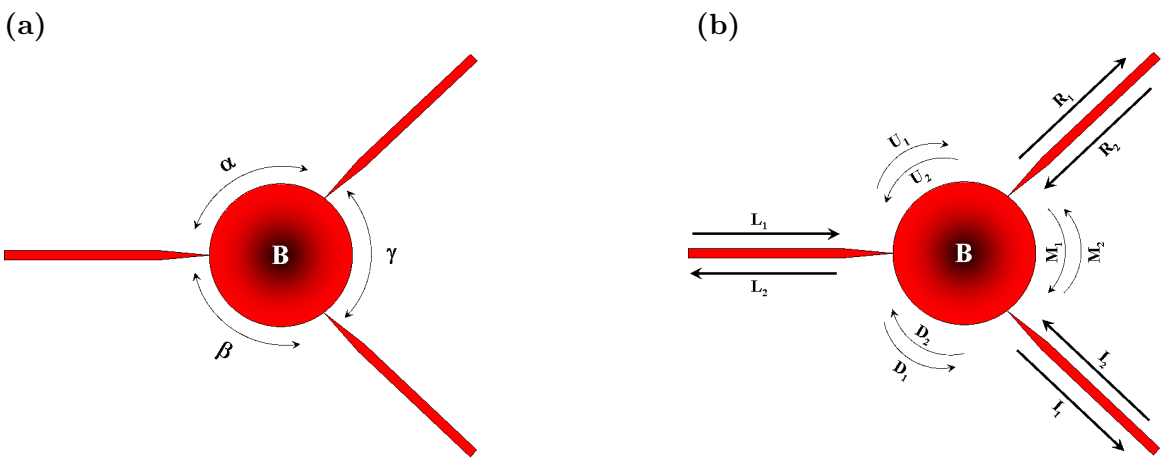

FIG. 13: Parameters designation in the three terminal continuum model. Panel a: The angular separations between the three terminals. Panel b: The amplitudes of the different parts of the wave function.

The scattering amplitudes characterizing the junctions are given in Fig. 8, and obey the scattering matrix unitary condition: $c = \sqrt{1-2\epsilon}$, $a = \frac{1}{2}(1-c)$, and $b = -\frac{1}{2}(1+c)$. For simplicity, in what follows we assume that all the junctions are identical. This assumption can be easily corrected to the case of non-identical junctions.

Using these notations it is again possible to write scattering matrix relations between the incoming and outgoing wave amplitudes at each junction:

$$\begin{pmatrix} L_2 \\ U_1 \\ D_1 \end{pmatrix} = \begin{pmatrix} c & \sqrt{\epsilon} & \sqrt{\epsilon} \\ \sqrt{\epsilon} & a & b \\ \sqrt{\epsilon} & b & a \end{pmatrix} \begin{pmatrix} L_1 \\ U_2 e^{i\Phi_1^\alpha} \\ D_2 e^{i\Phi_2^\beta} \end{pmatrix}$$

$$\begin{pmatrix} R_1 \\ M_1 \\ U_2 \end{pmatrix} = \begin{pmatrix} c & \sqrt{\epsilon} & \sqrt{\epsilon} \\ \sqrt{\epsilon} & a & b \\ \sqrt{\epsilon} & b & a \end{pmatrix} \begin{pmatrix} R_2 \\ M_2 e^{i\Phi_1^\gamma} \\ U_1 e^{i\Phi_2^\alpha} \end{pmatrix} \tag{13}$$

$$\begin{pmatrix} I_1 \\ D_2 \\ M_2 \end{pmatrix} = \begin{pmatrix} c & \sqrt{\epsilon} & \sqrt{\epsilon} \\ \sqrt{\epsilon} & a & b \\ \sqrt{\epsilon} & b & a \end{pmatrix} \begin{pmatrix} I_2 \\ D_1 e^{i\Phi_1^\beta} \\ M_1 e^{i\Phi_2^\gamma} \end{pmatrix}.$$

Here $\Phi_1^{\Delta=\alpha,\beta,\gamma} = \Delta Rk - \Delta\frac{\phi}{\phi_0}$, and $\Phi_2^{\Delta=\alpha,\beta,\gamma} = \Delta Rk + \Delta\frac{\phi}{\phi_0}$. Eliminating the equations for the wave amplitudes on the ring $(U_{1,2}, D_{1,2}, M_{1,2})$, similar to the two-terminal continuum model treatment, and plugging the solution in the equations for the outgoing amplitudes, I_1 and R_1, we get a relation between the incoming amplitude on the left lead L_1 and both outgoing amplitudes. The probability to transmit through the upper (lower) outgoing lead is given by $T^u = \left|\frac{R_1}{L_1}\right|^2$ ($T^l = \left|\frac{I_1}{L_1}\right|^2$). The exact expressions for these transmittance probabilities, even when setting the incoming wave amplitudes R_2 and I_2 to zero, are somewhat tedious, however they are given here for the sake of completeness.

The denominator of the transmittance probability for both output channels is given by the following expression:

$$
\begin{aligned}
T_{denominator} = \\
&\frac{1}{16}(c^2+1)(19-12c+2c^2-12c^3+19c^4)+32c^3\cos(4\pi kr)+ \\
&2(c-1)^4c\{\cos[4\pi kr(1-2\alpha)]+\cos[4\pi kr(1-2\beta)]+\cos[4\pi kr(1-2\gamma)]\}- \\
&8(c-1)^2c(c^2+1)\{\cos[4\pi kr(\alpha-1)]+\cos[4\pi kr(\beta-1)]+\cos[4\pi kr(\gamma-1)]\}- \\
&4(c-1)^2(2-c+2c^2-c^3+2c^4)[\cos(4\pi kr\alpha)+\cos(4\pi kr\beta)+\cos(4\pi kr\gamma)]+ \\
&2(c-1)^4(c^2+1)\{\cos[4\pi kr(\alpha-\beta)]+\cos[4\pi kr(\alpha-\gamma)]+\cos[4\pi kr(\beta-\gamma)]\}- \\
&0.125(c+1)^4\times \\
&\{-4[1+c(c-1)]\cos(2\pi kr)+(c-1)^2[\cos[2\pi kr(1-2\alpha)]+\cos[2\pi kr(1-2\beta)] \\
&+\cos[2\pi kr(1-2\gamma)]]\}\cos(2\pi\frac{\phi}{\phi_0})+\frac{1}{16}(c+1)^6\cos^2(2\pi\frac{\phi}{\phi_0}).
\end{aligned}
\tag{14}
$$

The numerator of the transmittance probability through the upper output channel is given

by:

$$
\begin{aligned}
T^{u}_{numerator} = -0.5\epsilon^2\{&-4(1+c^2)+ \\
&2(c-1)^2\cos(4\pi kr\alpha) + (c+1)^2\cos(4\pi kr\beta) + 2(c-1)^2\cos(4\pi kr\gamma)+ \\
&4c\cos\left[4\pi kr(\alpha+\gamma)\right] - (c-1)^2\cos\left[4\pi kr(\alpha-\gamma)\right] - \\
&2c(c+1)\cos\left[2\pi\left(\frac{\phi}{\phi_0}-kr\right)\right] - 2(c+1)\cos\left[2\pi\left(\frac{\phi}{\phi_0}+kr\right)\right] - \\
&(c^2-1)\cos\left[2\pi\left(\frac{\phi}{\phi_0}+(1-2\alpha)kr\right)\right] + (c^2-1)\cos\left[2\pi\left(\frac{\phi}{\phi_0}-(1-2\alpha)kr\right)\right] + \\
&2(c+1)\cos\left[2\pi\left(\frac{\phi}{\phi_0}+(1-2\beta)kr\right)\right] + 2c(c+1)\cos\left[2\pi\left(\frac{\phi}{\phi_0}-(1-2\beta)kr\right)\right] - \\
&(c^2-1)\cos\left[2\pi\left(\frac{\phi}{\phi_0}+(1-2\gamma)kr\right)\right] + (c^2-1)\cos\left[2\pi\left(\frac{\phi}{\phi_0}-(1-2\gamma)kr\right)\right]\}.
\end{aligned}
\tag{15}
$$

The numerator of the transmittance probability through the lower output channel is given by:

$$
\begin{aligned}
T^{l}_{numerator} = -0.5\epsilon^2\{&-4(1+c^2)+ \\
&(c+1)^2\cos(4\pi kr\alpha) + 2(c-1)^2\cos(4\pi kr\beta) + 2(c-1)^2\cos(4\pi kr\gamma)+ \\
&4c\cos\left[4\pi kr(\beta+\gamma)\right] - (c-1)^2\cos\left[4\pi kr(\beta-\gamma)\right] - \\
&2c(c+1)\cos\left[2\pi\left(\frac{\phi}{\phi_0}+kr\right)\right] - 2(c+1)\cos\left[2\pi\left(\frac{\phi}{\phi_0}-kr\right)\right] + \\
&2c(c+1)\cos\left[2\pi\left(\frac{\phi}{\phi_0}+(1-2\alpha)kr\right)\right] + 2(c+1)\cos\left[2\pi\left(\frac{\phi}{\phi_0}-(1-2\alpha)kr\right)\right] + \\
&(c^2-1)\cos\left[2\pi\left(\frac{\phi}{\phi_0}+(1-2\beta)kr\right)\right] - (c^2-1)\cos\left[2\pi\left(\frac{\phi}{\phi_0}-(1-2\beta)kr\right)\right] + \\
&(c^2-1)\cos\left[2\pi\left(\frac{\phi}{\phi_0}+(1-2\gamma)kr\right)\right] - (c^2-1)\cos\left[2\pi\left(\frac{\phi}{\phi_0}-(1-2\gamma)kr\right)\right]\}.
\end{aligned}
\tag{16}
$$

The backscattering probability is the complementary part of the sum of the transmittance probability through both the upper and the lower leads.

The resulting transmittance probability through one of the outgoing leads, for the symmetric case where $\alpha = \beta = \gamma = \frac{2\pi}{3}$, is presented in Fig. 14 as a function of the magnetic flux threading the ring and the wave number of the conducting electron. In the high coupling limit (left panel of Fig. 14) the system is characterized by a wide range of high transmittance which can be shifted along the AB period by changing the electron's wavenumber. Magnetic

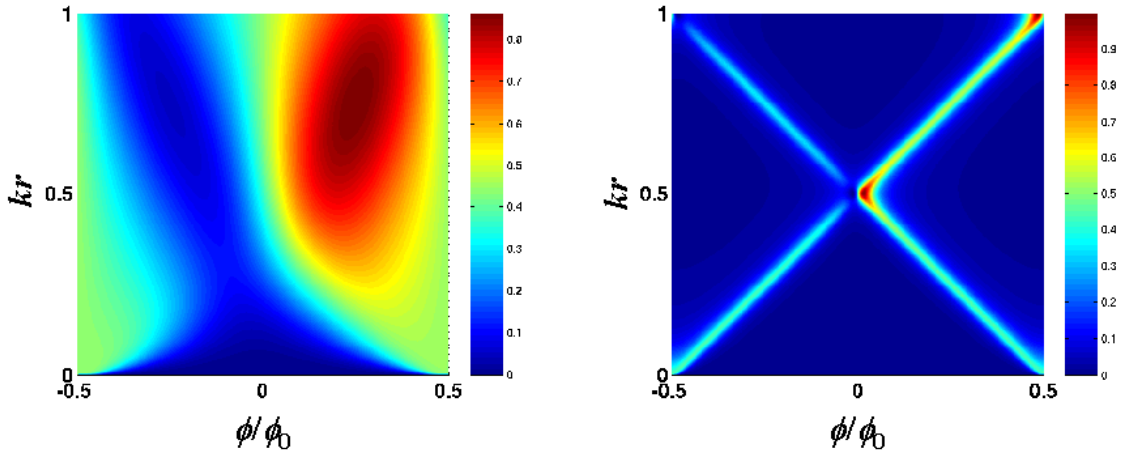

FIG. 14: The transmittance of a three-terminal device as a function of the magnetic flux and the wavenumber of the conducting electron as calculated using the continuum model. Left panel: high coupling ($\epsilon = 0.495$), right panel: low coupling ($\epsilon = 0.095$). Color-bar: deep blue - no transmittance ($T = 0$), deep red - full transmittance ($T = 1$).

switching of the transmittance at a given wavenumber value for this coupling regime requires high magnetic fields, since the transmittance peaks are quite broad.

As the coupling is decreased from its maximal value of $\epsilon = 0.5$ to very low values (right panel of Fig. 14), a resonant tunneling junction is formed and the transmittance probability becomes very sensitive to the magnetic flux. Similar to the two terminal case, this is translated to sharper peaks that develop in the magnetotransmittance curve. For the parameters studied in the right panel of Fig. 14 there is negligible transmittance for all values of k at zero magnetic field. We notice that the position of the first maximum in the transmittance depends linearly on the value of ϕ and k. Fine tuning the wave number to a value that satisfies $kR = 0.5$ results in the appearance of the sharp transmittance peak at finite, relatively low, magnetic flux and thus allows the switching of the device at feasible magnetic fields.

A careful examination of the transmittance probability spectrum for $kR = 0.5$ at the low magnetic flux regime reveals that the appearance of the transmittance peak is sensitive to the polarity of the magnetic flux. While at a positive magnetic flux a pronounce peak is observed, at the negative magnetic flux counterpart this peak is absent. This magnetic rectification phenomena is, allegedly, in contrast with the Onsager symmetry relation[138,146–148] obeyed in the two terminal case which states that $g(\phi) = g(-\phi)$ where g is the conductance.

This contradiction is resolved by considering the transmittance probability through the other output channel which can be obtained by applying a reflection transformation with respect to a plain passing through the incoming lead and perpendicular to the cross section of the ring. The Hamiltonian of the system is invariant to such a transformation only if accompanied by a reversal of the direction of the magnetic field. It follows that the transmittance probability through one outgoing lead is the mirror image of the transmittance through the other. Thus, we find that for the second output channel (not shown) the peak is observed at a negative magnetic flux rather than at a positive one. Onsager's condition is, therefore, regained for the sum of the transmittance probabilities through both output channels.

The above analysis implies that at zero magnetic field both output channels are closed and the electron is totally reflected. The application of a relatively small positive magnetic field opens only one output channel and forces the electrons to transverse the ring through this channel alone. Reversing the polarity of the magnetic field causes the output channels to interchange roles and forces the electrons to pass the ring through the other lead.

To summarize this section, magnetic fields offer unique controllability over the conductance of nanometer scale interferometers. Their polarity can be used to selectively switch different conducting channels. While *non-uniform* scalar potentials have been used in *mesoscopic* physics to obtain a similar effect,[149] such control cannot be obtained via the application of uniform scalar potentials which are commonly used to control molecular scale devices. This is due to the fact that such scalar potentials lack the symmetry breaking nature of magnetic vector potentials.

The question now shifts to the plausibility of the principles discussed above within the framework of the continuum model in molecular based devices. In order to address this question we present, in the following chapter, a magnetic extended Hückel theory developed for the atomistic calculation of the magnetoresistance of molecular systems.

VI. ATOMISTIC CALCULATIONS - MODEL

The model presented in chapter IV is a one-dimensional single mode transport model which was introduced in order to identify and isolate the important physical parameters that allow the control over the profile of the AB period. In order to capture the more complex nature of the electronic structure of realistic nanoscale AB interferometers and its influence on the AB magnetoresistance measurement we now present a model which was developed for the calculation of magneto-conductance through molecular setups. Within our approach we calculate the conductance using non-equilibrium Green's function (NEGF) formalism. In the case of pure elastic scattering, this reduces to the Landauer formalism, which relates the conductance to the transmittance probability through the system. The transmittance is calculated using Green's functions (GFs) and absorbing potentials techniques, based on the electronic structure of the system. The electronic structure is, in turn, calculated using an extension of the extended Hückel method which incorporates the influence of external magnetic fields. The resulting magneto-conductance spectrum can be then studied for different molecular setups and conditions.

A. Conductance

We are interested in calculating the conductance through a molecular device coupled to two macroscopic conducting leads in the presence of an external magnetic field. Our starting point is the current formula obtained within the NEGF framework:[63,150]

$$I_{L(R)} = \frac{2e}{\hbar}\int \frac{dE}{2\pi} Tr\left[\Sigma^{<}_{L(R)}(E)G^{>}_{d}(E) - \Sigma^{>}_{L(R)}G^{<}_{d}(E)\right]. \tag{17}$$

Here $I_{L(R)}$ is the net current measured at the left (right) molecule-lead junction, $G^{<}_{d}(E)$ and $G^{>}_{D}(E)$ are the lesser and greater device Green's functions, respectively, and $\Sigma^{<}_{L(R)}$ and $\Sigma^{>}_{L(R)}$ are the left (right) lesser and greater self energy terms respectively. The first term in the trace in Eq. 17 can be identified with the rate of in-scattering of electrons into the device from the left (right) lead. Similarly the second term represents the out-scattering rate of electrons into the left (right) lead. The difference between these two terms gives the net, energy dependent, flow rate of electrons through the device. When integrated over the energy and multiplied by twice (to account for spin states) the electrons charge this results in the net current flowing through the left (right) junction. It can be shown[151] that $I_L = -I_R$

in analogy to Kirchoff's law, and therefore Eq. 17 represents the full current through the device.

The lesser and greater GFs appearing in Eq. 17 are related to the retarded ($G^r(E)$) and advanced ($G^a(E)$) GFs, which will be discussed later, through the Keldysh equation[152]:

$$\begin{cases} G_d^<(E) = G_d^r(E)\Sigma^<(E)G_d^a(E) \\ G_d^>(E) = G_d^r(E)\Sigma^>(E)G_d^a(E), \end{cases} \tag{18}$$

where in the pure elastic scattering case:

$$\begin{cases} \Sigma^< = \Sigma_L^< + \Sigma_R^< \\ \Sigma^> = \Sigma_L^> + \Sigma_R^>. \end{cases} \tag{19}$$

Furthermore, the lesser and greater self energy terms in Eqs. 17 and 19 are related to the retarded ($\Sigma_{L(R)}^r(E)$) and advanced ($\Sigma_{L(R)}^a(E)$) self energies, which will also be discussed later, in the following manner:

$$\begin{cases} \Sigma_{L(R)}^<(E) = -f_{L(R)}(E,\mu_{L(R)})\left[\Sigma_{L(R)}^r(E) - \Sigma_{L(R)}^a(E)\right] \\ \Sigma_{L(R)}^>(E) = \left[1 - f_{L(R)}(E,\mu_{L(R)})\right]\left[\Sigma_{L(R)}^r(E) - \Sigma_{L(R)}^a(E)\right], \end{cases} \tag{20}$$

where $f_{L(R)}(E,\mu_{L(R)}) = \left[1 + e^{\beta(E-\mu_{L(R)})}\right]^{-1}$ is the Fermi-Dirac occupation distribution in the left (right) lead, $\mu_{L(R)}$ is the chemical potential of the left (right) lead and $\beta = \frac{1}{k_B T}$ where k_B is Boltzmann's constant and T is the temperature.

Upon plugging Eqs. 18 and 20 into Eq. 17, we get the following result for the current:

$$\begin{aligned} I =& \frac{2e}{\hbar}\int \frac{dE}{2\pi}\left[f_R(E,\mu_R) - f_L(E,\mu_L)\right] \\ & Tr\left\{\left[\Sigma_L^r(E) - \Sigma_L^a(E)\right]G_d^r(E)\left[\Sigma_R^r(E) - \Sigma_R^a(E)\right]G_d^a(E)\right\}. \end{aligned} \tag{21}$$

We can now define the level width matrix $\Gamma_{L(R)}$ in the following manner:

$$\Gamma_{L(R)}(E) \equiv i\left[\Sigma_{L(R)}^r(E) - \Sigma_{L(R)}^a(E)\right] \tag{22}$$

and rewrite Eq. 21 as:

$$I = \frac{2e}{\hbar}\int \frac{dE}{2\pi}\left[f_L(E,\mu_L) - f_R(E,\mu_R)\right] Tr\left[\Gamma_L(E)G_d^r(E)\Gamma_R(E)G_d^a(E)\right]. \tag{23}$$

It is now possible to identify $T(E) = Tr\left[\Gamma_L(E)G_d^r(E)\Gamma_R(E)G_d^a(E)\right]$ as the electron transmission probability through the molecule and the difference in the Fermi-Dirac distribution

functions as the net, energy dependent, density of current carrying particles from the left (right) lead to the right (left) lead, due to the difference in their chemical potentials.[153] Therefore, integrating over the energy we obtain the current.

Since we are interested in calculating the conductance (g) we can now define the differential conductance as the derivative of the current with respect to the applied bias voltage (V_b):

$$\begin{aligned} g =& \frac{\partial I}{\partial V_b} \\ =& \frac{2e}{\hbar}\frac{\partial}{\partial V_b}\int \frac{dE}{2\pi}\left[f_L(E,\mu_L) - f_R(E,\mu_R)\right] Tr\left[\Gamma_L(E) G_d^r(E) \Gamma_R(E) G_d^a(E)\right]. \end{aligned} \tag{24}$$

If one assumes that the bias voltage applied does not alter considerably the energetic structure of the device, the only contribution of the bias in Eq. 23 appears in the Fermi-Dirac distribution functions. In what follows, this assumption is reasonable since we shall consider the limit of zero bias conductance. Therefore, it is possible to directly conduct the differentiation in equation 24 to get the following relation:

$$\begin{aligned} g =& \frac{\partial I}{\partial V_b} \\ =& \frac{2e}{\hbar}\int \frac{dE}{2\pi}\frac{\partial\left[f_L(E,\mu_L) - f_R(E,\mu_R)\right]}{\partial V_b} Tr\left[\Gamma_L(E) G_d^r(E) \Gamma_R(E) G_d^a(E)\right]. \end{aligned} \tag{25}$$

If we further assume that the bias potential drops sharply and equally at both junctions[154], the chemical potentials are given by $\mu_{L(R)} = E_f^{L(R)} + (-)\frac{1}{2}eV_b$, where $E_f^{L(R)}$ is the Fermi energy of the left(right) lead. Thus, the derivative with respect to the bias voltage appearing in Eq. 25 is given by ¶¶ :

$$\frac{\partial\left[f_L(E,\mu_L) - f_R(E,\mu_R)\right]}{\partial V_b} = 0.5e\beta\left\{\frac{e^{-\beta|E-\mu_L|}}{\left[1+e^{-\beta|E-\mu_L|}\right]^2} + \frac{e^{-\beta|E-\mu_R|}}{\left[1+e^{-\beta|E-\mu_R|}\right]^2}\right\}. \tag{26}$$

If both Fermi energies of the leads are aligned with the Fermi energy of the device ***, and the chemical potential difference arises from the bias voltage alone, then at the limit of zero

¶¶ Since the left(right) term in Eq. 26 is symmetric with respect to $\mu_{L(R)}$ we can consider only the absolute value $|E-\mu_L(R)|$ in these expressions which is beneficial when evaluating this expression numerically. Furthermore, due to the structure of the integral in Eq. 24 it is sufficient to conduct the integration over two narrow regions centered about μ_L and μ_R. The width of these integration windows can be determined from the temperature and the desired integration convergence accuracy by $W = \frac{log(r-1)}{\beta}$, where W is the integration window width and r is the reduction factor defined as the ratio of the value of $\frac{\partial[f_L(E,\mu_L)-f_R(E,\mu_R)]}{\partial V_b}$ at $\mu_{L(R)}$ and at the edges of the integration region $\mu_{L(R)} \pm W$.

*** Experimentally this can be achieved by using identical leads and properly gating the device.

temperature and zero bias conductance the expression appearing in Eq. 26 approaches a sharp δ function located at the Fermi energy of the molecule and Eq. 24, in turn, reduces to the well established Landauer formula[56,63] which directly relates the conductance to the transmittance probability of the current carrying entity through the relevant device:

$$g = g_0 T, \tag{27}$$

where $g_0 = \frac{2e^2}{h}$ is the conductance quantum.

Considering the full expression given by Eq. 25 it can be seen that for the calculation of the conductance, or more specifically of the transmittance probability, it is necessary to obtain the retarded and advanced GFs of the device and the retarded and advanced self energies of the leads. Obtaining these is the subject of the next section.

B. Retarded and advanced Green's functions and self energies

In the previous section we have derived a formula for the conductance through a microscopic device coupled to two macroscopic conducting leads based on NEGF formalism. The purpose of this section is to obtain direct expressions for the retarded and advanced GFs and for the retarded and advanced leads self energies that appear in this formula.

Following again the lines of Non-Equilibrium Green's function theory[155] the GF associated with a Hamiltonian $\hat{H}$ evaluated in a non-orthogonal basis set must satisfy the following relation in energy space:

$$(E\hat{S} - \hat{H})\hat{G}(E) = \hat{I}, \tag{28}$$

where E is the energy, $\hat{S}$ is the overlap matrix, $\hat{G}(E)$ is the GF, and $\hat{I}$ a unit matrix of the appropriate dimensions.

As suggested above, in molecular conductance calculations it is customary to divide the system into the 'device' which is the conducting molecule[†††] and the 'leads' which are the macroscopic conducting contacts through which electrons are injected into and taken out of the 'device'. In a two terminal setup this is translated to the following sub-matrices devision

[†††] usually one defines an 'extended molecule' which is the molecule itself accompanied with a limited portion of the leads which is influenced by the proximity to the molecule.

of Eq. 28:[155,156]

$$\begin{pmatrix} \epsilon\hat{S}_L - \hat{H}_L & \epsilon\hat{S}_{Ld} - \hat{V}_{Ld} & 0 \\ \epsilon\hat{S}_{dL} - \hat{V}_{dL} & \epsilon\hat{S}_d - \hat{H}_d & \epsilon\hat{S}_{dR} - \hat{V}_{dR} \\ 0 & \epsilon\hat{S}_{Rd} - \hat{V}_{Rd} & \epsilon\hat{S}_R - \hat{H}_R \end{pmatrix} \begin{pmatrix} \hat{G}^r_L(\epsilon) & \hat{G}^r_{Ld}(\epsilon) & \hat{G}^r_{LR}(\epsilon) \\ \hat{G}^r_{dL}(\epsilon) & \hat{G}^r_d(\epsilon) & \hat{G}^r_{dR}(\epsilon) \\ \hat{G}^r_{RL}(\epsilon) & \hat{G}^r_{Rd}(\epsilon) & \hat{G}^r_R(\epsilon) \end{pmatrix} = \begin{pmatrix} \hat{I}_L & \hat{0} & \hat{0} \\ \hat{0} & \hat{I}_d & \hat{0} \\ \hat{0} & \hat{0} & \hat{I}_R \end{pmatrix}. \tag{29}$$

Here, $\hat{H}_{L(R)}$, and $\hat{H}_d$ are the left(right) semi-infinite lead, and the device Hamiltonians, respectively, $\hat{S}_{L(R)}$, and $\hat{S}_d$ are the left(right) lead, and the device overlap matrices, respectively, $\hat{V}_{L(R)d}$ are the coupling matrices between the left(right) lead and the device, and $\hat{S}_{L(R)d}$ are the overlap matrices between the left(right) lead and the device. Since the Hamiltonian is Hermitian one finds that $\hat{V}_{dL(R)} = \hat{V}^\dagger_{L(R)d}$, and in the complex GISTO basis set the same requirement applies for the overlap matrices $\hat{S}_{dL(R)} = \hat{S}^\dagger_{L(R)d}$. All the terms discussed above are calculated using a formalism which will be presented in section VI D.

A complex energy $\epsilon = \lim_{\eta\to 0}\{E + i\eta\}$ has to be introduce in order to shift the poles of the Green's function from the real axis and allow for the convergence of both an analytical and a numerical evaluation of the integrals over the GFs. This softens the sharp singularities of the GF into a smother Lorentzian shape which in the limit of $\eta \to 0$ restores the δ function characteristics of the imaginary part. The superscript r which stands for 'retarded' is added to the GFs when using this form of complex energy. It should be noted that in Eq. 29 we assume that the leads do not directly interact so that $\hat{S}_{LR} = \hat{S}_{RL} = \hat{V}_{LR} = \hat{V}_{RL} = \hat{0}$.

Solving Eq. 29 for the middle column of the GF matrix results in the following expression for the retarded device GF (which appears in Eq. 25) $\hat{G}^r_d(\epsilon)$, when coupled to the two leads:

$$\hat{G}^r_d(\epsilon) = \left[\left(G^{r0}_d(\epsilon)\right)^{-1} - \hat{\Sigma}^r_L(\epsilon) - \hat{\Sigma}^r_R(\epsilon)\right]^{-1}, \tag{30}$$

where $\hat{G}^{r0}_d(\epsilon) = \left[\epsilon\hat{S}_d - \hat{H}_d\right]^{-1}$ is the GF of the bare device, and $\hat{\Sigma}^r_{L(R)}(\epsilon)$ is the retarded self energy of the left(right) lead given by:

$$\hat{\Sigma}^r_{L(R)}(\epsilon) = \left(\epsilon\hat{S}_{dL(R)} - \hat{H}_{dL(R)}\right)\hat{G}^{r0}_{L(R)}(\epsilon)\left(\epsilon\hat{S}_{L(R)d} - \hat{H}_{L(R)d}\right). \tag{31}$$

Here, $\hat{G}^{r0}_{L(R)}(\epsilon) = \left[\epsilon\hat{S}_{L(R)} - \hat{H}_{L(R)}\right]^{-1}$ is the retarded GF of the bare left(right) lead. The advanced device GF is the Hermitian conjugate of its retarded counterpart $\hat{G}^a_d(\epsilon) = \left[\hat{G}^r_d(\epsilon)\right]^\dagger$.

The self energy terms appearing in Eqs. 30 and 31 represent the effect of the coupling to the leads on the GF of the device. The calculation of these terms requires the GF of the bare

lead $\hat{G}^{r0}_{L(R)}(\epsilon)$. This is not a simple task since the leads are macroscopic sources of electrons whose GFs are impossible to calculate directly. A way to overcome this obstacle is to represent the leads as periodic bulk structures of a semi-infinite nature. Using common solid state physics techniques the periodicity of the bulk can considerably reduce the dimensionality of the problem and thus enable the calculation of the electronic structure of the leads. For this we use an efficient iterative procedure developed by López Sancho et al.[157–159] Within this approach the semi-infinite bulk is divided into a set of identical principal layers, as shown in Fig. 15, in such a manner that only adjacent layers overlap and interact. Using Eq. 28

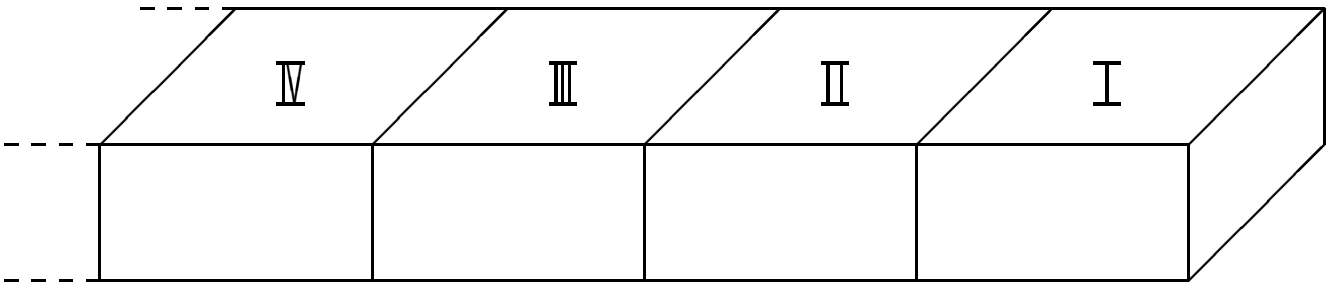

FIG. 15: Division of the semi-infinite bulk lead into a set of nearest neighbors interacting layers.

the resulting GF can be represented as the inverse of a nearest neighbors block-tridiagonal matrix of the form:

$$\begin{pmatrix} \hat{G}_{00}(\epsilon) & \hat{G}_{01}(\epsilon) & \hat{G}_{02}(\epsilon) & \hat{G}_{03}(\epsilon) & \cdots \\ \hat{G}_{10}(\epsilon) & \hat{G}_{11}(\epsilon) & \hat{G}_{12}(\epsilon) & \hat{G}_{13}(\epsilon) & \cdots \\ \hat{G}_{20}(\epsilon) & \hat{G}_{21}(\epsilon) & \hat{G}_{22}(\epsilon) & \hat{G}_{23}(\epsilon) & \cdots \\ \hat{G}_{30}(\epsilon) & \hat{G}_{31}(\epsilon) & \hat{G}_{32}(\epsilon) & \hat{G}_{33}(\epsilon) & \cdots \\ \vdots & \vdots & \vdots & \vdots & \ddots \end{pmatrix} = \begin{pmatrix} \epsilon\hat{S}_{00} - \hat{H}_{00} & \epsilon\hat{S}_{01} - \hat{V}_{01} & 0 & 0 & \cdots \\ \epsilon\hat{S}_{10} - \hat{V}_{10} & \epsilon\hat{S}_{00} - \hat{H}_{00} & \epsilon\hat{S}_{01} - \hat{V}_{01} & 0 & \cdots \\ 0 & \epsilon\hat{S}_{10} - \hat{V}_{10} & \epsilon\hat{S}_{00} - \hat{H}_{00} & \epsilon\hat{S}_{01} - \hat{V}_{01} & \cdots \\ 0 & 0 & \epsilon\hat{S}_{10} - \hat{V}_{10} & \epsilon\hat{S}_{00} - \hat{H}_{00} & \cdots \\ \vdots & \vdots & \vdots & \vdots & \ddots \end{pmatrix}^{-1} . \tag{32}$$

Here, $\hat{S}_{I,I} = \hat{S}_{II,II} = \hat{S}_{III,III} = \cdots \equiv \hat{S}_{00}$ is the overlap matrix of the principal layer with itself, $\hat{S}_{I,II} = \hat{S}_{II,III} = \hat{S}_{III,IV} = \cdots \equiv \hat{S}_{01}$ is the overlap matrix between two adjacent layers, and as before $\hat{S}_{10} = \left[\hat{S}_{01}\right]^{\dagger}$. $\hat{H}_{I,I} = \hat{H}_{II,II} = \hat{H}_{III,III} = \cdots \equiv \hat{H}_{00}$ is the Hamiltonian matrix of the principal layer, $\hat{V}_{I,II} = \hat{V}_{II,III} = \hat{V}_{III,IV} = \cdots \equiv \hat{V}_{01}$ is the coupling matrix between two adjacent layers, and $\hat{V}_{10} = \left[\hat{V}_{01}\right]^{\dagger}$.

Eq. 32 is a matrix representation of a set of equations for the semi-infinite bulk GF matrix

elements $\hat{G}_{ij}(\epsilon)$ which can be solved iteratively to get a compact expression:

$$\hat{G}(\epsilon) = \left[(\epsilon\hat{S}_{00} - \hat{H}_{00}) + (\epsilon\hat{S}_{01} - \hat{H}_{01})T(\epsilon) + (\epsilon\hat{S}_{01}^{\dagger} - \hat{H}_{01}^{\dagger})\overline{T}(\epsilon)\right]^{-1}. \tag{33}$$

The transfer matrices T and $\overline{T}$ are given by converging series of the form:

$$\begin{cases} T(\epsilon) = t_0 + \tilde{t}_0 t_1 + \tilde{t}_0\tilde{t}_1 t_2 + \cdots + \tilde{t}_0\tilde{t}_1\tilde{t}_2\cdots t_n \\ \overline{T}(\epsilon) = \tilde{t}_0 + t_0\tilde{t}_1 + t_0 t_1\tilde{t}_2 + \cdots + t_0 t_1 t_2\cdots\tilde{t}_n, \end{cases} \tag{34}$$

where t_i and $\tilde{t}_i$ are defined by the recursion relations:

$$\begin{cases} t_i = \left(I - t_{i-1}\tilde{t}_{i-1} - \tilde{t}_{i-1}t_{i-1}\right)^{-1} t_{i-1}^2 \\ \tilde{t}_i = \left(I - t_{i-1}\tilde{t}_{i-1} - \tilde{t}_{i-1}t_{i-1}\right)^{-1} \tilde{t}_{i-1}^2, \end{cases} \tag{35}$$

with the following initial conditions:

$$\begin{cases} t_0 = \left(\epsilon\hat{S}_{00} - \hat{H}_{00}\right)^{-1} V_{01}^{\dagger} \\ \tilde{t}_0 = \left(\epsilon\hat{S}_{00} - \hat{H}_{00}\right)^{-1} V_{01}. \end{cases} \tag{36}$$

After calculating the semi-infinite bulk GF given in Eq. 33, the left and right leads self energies can be determined using Eq. 31, and the $\hat{\Gamma}_{L(R)}$ matrices appearing in the conductance expression (Eq. 25) can be calculated using Eq. 22 with, $\hat{\Sigma}^a_{L(R)}(\epsilon) = \left[\hat{\Sigma}^r_{L(R)}(\epsilon)\right]^{\dagger}$.

In some calculations it is found to be useful to neglect the energy dependence of the Γ_L and Γ_R matrices and replace them with constant matrices. These constant matrices elements are taken to be the elements of the energy dependent matrices evaluated at the relevant lead chemical potential. This approximation is usually referred to as the wide band approximation (WBA) or alternatively the wide band limit (WBL).[150] At the zero bias limit as the temperature reduces this approximation becomes valid since the integration in Eq. 25 involves only a narrow energy window at which the Γ matrices can be approximately regarded as constant.

C. An alternative - Absorbing imaginary potentials

A second methodology for the calculation of the transmittance probability involves the application of absorbing potentials[160,161]. Within this approach the $\Gamma_{L(R)}$ matrix appearing

in Eq. 25 is a negative imaginary potential placed deep within the left(right) lead. The purpose of this potential is to absorb an electron traveling in the lead away from the molecular device before it reaches the 'edge' of the lead. This assures that the effect of reflections from the distant lead edge is suppressed to a desired accuracy and thus enables to truncate the lead representation to a computable size.

In the present work we have used a Gaussian imaginary potential of the form $V_{L(R)} = V_0 e^{-\frac{(z-z_0^{L(R)})^2}{2\sigma^2}}$, here V_0 is the potential hight, σ the potential width, and $z_0^{L(R)}$ its location along the left(right) lead assuming that the leads are located along the Z axis. The generalization of the above expression to the case of arbitrary leads direction is straightforward. The parameters of the potential are chosen such that electrons possessing a kinetic energy in a wide band around the Fermi energy are effectively absorbed[58]. As a rule of thumb one can choose the potential hight to be the location of the Fermi energy, E_F, above the bottom of the calculated valence band, E_0, $V_0 \approx E_F - E_0$. The width of the potential should be sufficiently larger than the Fermi wave length, as an example for a carbon wire we choose $\sigma \approx 20a_0$ where a_0 is Bohr's radius. The origin of the potential $z_0^{L(R)}$ is chosen such that the region of the lead close to the device where the effect of the potential is negligible contains at least a few Fermi wave length such that the metallic nature of the lead is appropriately captured. This choice of parameters should serve as an initial try and a convergence check should then be conducted. The Gaussian absorbing potential is of course not a unique choice and other forms of absorbing potential expressions can be used[162].

Within the absorbing potentials methodology the system is not divided into sub-units and the dimensionality of all the matrices appearing in Eq. 25 is the dimensionality of the full system (device+truncated leads). The $\Gamma_{L(R)}$ matrix elements are calculated (usually numerically) as integrals of the atomic basis functions over the imaginary potential $V_{L(R)}$. It should be noted that similar to the WBA discussed above, the Γ matrices in the current methodology are energy independent. This fact considerably reduces the computational efforts involved in the evaluation of the transmission probability.

The device GF in Eq. 25 is now replaced by the GF of the whole system which, similar to Eq. 30, is given by:

$$\hat{G}^r(E) = \left[E\hat{S} - \hat{H} - i\hat{\Gamma}_L - i\hat{\Gamma}_R\right]^{-1}, \tag{37}$$

where $\hat{S}$ and $\hat{H}$ are the overlap and Hamiltonian matrices, respectively, calculated for the

whole system, and E is the real energy. The advanced GF is as before the Hermitian conjugate of the retarded counterpart $G^a(E) = [G^r(E)]^\dagger$.

The last remaining task for the calculation of the conductance is the calculation of the Hamiltonian, overlap, and coupling matrices appearing in Eq. 29. This calculation is explained in the next section.

D. Electronic structure - Magnetic Extended Hückel Theory

Our final task in the calculation of the conductance is the appropriate representation of the electronic structure of the system under the influence of the external magnetic field. For this purpose, a magnetic extended Hückel theory (MEHT) was developed.

We consider the Hamiltonian of the multi electronic problem, which is given by:

$$\hat{H} = \frac{1}{2m_e}\left[\hat{\mathbf{P}} - q\mathbf{A}\right]^2 + V(\mathbf{r}). \tag{38}$$

This is similar to the Hamiltonian presented in Eq. 1 apart from the fact that $\mathbf{P}$ and $\mathbf{r}$ are vectors in the multi-electron space. Within the MEHT formalism the contribution at zero vector potential $\hat{H}(\mathbf{A}=\mathbf{0}) = \frac{\mathbf{P^2}}{\mathbf{2m}} + \mathbf{V}(\mathbf{r})$ is represented by the Extended Hückel (EH) Hamiltonian[163] $\hat{H}^{EH}$ which treats the complex many body problem using a mean field, single-particle, semi-empirical approach. The effect of applying a vector potential is taken into account by simply adding the appropriate magnetic terms to the EH Hamiltonian:

$$\hat{H} = \hat{H}^{EH} - \frac{q}{2m_e}\left(\hat{\mathbf{P}}\cdot\mathbf{A} + \mathbf{A}\cdot\hat{\mathbf{P}}\right) + \frac{q^2}{2m}A^2. \tag{39}$$

As before we assume that the magnetic field is uniform and constant $\mathbf{B} = (B_x, B_y, B_z)$ and thus write down the related vector potential as: $\mathbf{A} = -\frac{1}{2}\mathbf{r}\times\mathbf{B} = -\frac{1}{2}(yB_z - zB_y, zB_x - xB_z, xB_y - yB_x)$. Putting this expression in Eq. 39 we get the following electronic Hamiltonian[164]:

$$\hat{H} = \hat{H}^{EH} - \frac{\mu_B}{\hbar}\mathbf{L}\cdot\mathbf{B} + \frac{q^2\mathbf{B}^2}{8m_e}\mathbf{r}_\perp^2. \tag{40}$$

Here, $\mu_B = \frac{q\hbar}{2m_e}$ is the Bohr magneton, $\mathbf{r}_\perp^2 = \mathbf{r}^2 - \frac{(\mathbf{r}\cdot\mathbf{B})^2}{\mathbf{B}^2}$ is the projection of $\mathbf{r} = (x, y, z)$ onto the plane perpendicular to $\mathbf{B}$, and $\hat{\mathbf{L}} = \mathbf{r}\times\hat{\mathbf{P}}$ is the angular momentum operator. In should be noted that by using this Hamiltonian we neglect effects such as Zeeman splitting and spin-orbit coupling which relate to the spin state of the electron.

For the sake of simplicity, and without limiting the generality of the solution, we assume that the AB ring is placed in the $Y-Z$ plane and that the magnetic field is applied parallel to the X-axis. With this the Hamiltonian in Eq. 40 is reduced to:

$$\hat{H} = \hat{H}^{EH} + i\mu_B B_x \left(y\frac{\partial}{\partial z} - z\frac{\partial}{\partial y} \right) + \frac{q^2 B_x^2}{8m_e}(y^2 + z^2). \tag{41}$$

A Slater Type Orbitals[165,166] (STO) basis set is used to evaluate the Hamiltonian and overlap matrices. In the presence of a magnetic field it is necessary to multiply each STO by an appropriate gauge factor which compensates for the finite size of the set. The resulting atomic orbitals are customarily referred to as Gauge Invariant[167,168] Slater Type Orbitals (GISTOs) and are given by:

$$|\overline{n,l,m}>_\alpha = e^{\frac{iq}{\hbar}\mathbf{A}_\alpha\cdot\mathbf{r}}|n,l,m>_\alpha = e^{\frac{iqB_x}{2\hbar}(y_\alpha z - z_\alpha y)}|n,l,m>_\alpha . \tag{42}$$

Here $|n,l,m>_\alpha$ is a STO (see Eq. A1 of appendix A) characterized by the set of quantum numbers (n,l,m), and centered on the atomic site α. $\mathbf{A}_\alpha$ is the value of the vector potential $\mathbf{A}$ at the nuclear position $\mathbf{R}_\alpha = (x_\alpha, y_\alpha, z_\alpha)$, and $|\overline{n,l,m}>_\alpha$ is the GISTO situated at α.

The generalized eigenvalue problem $\overline{\hat{H}}\psi_n = E_n\overline{\hat{S}}\psi$ is solved to get the electronic energy levels (E_n) and the molecular orbitals (ψ_n) characterizing the system. Here, $\overline{\hat{H}}$ and $\overline{\hat{S}}$ are the Hamiltonian and overlap matrices with elements given by $\overline{\hat{S}}_{1\alpha,2\beta} =_\alpha \left\langle \overline{n_1,l_1,m_1}|\overline{n_2,l_2,m_2} \right\rangle_\beta$ and $\overline{\hat{H}}_{1\alpha,2\beta} =_\alpha \left\langle \overline{n_1,l_1,m_1}|\hat{H}|\overline{n_2,l_2,m_2} \right\rangle_\beta$. We use the London approximation[167,168] for calculating the different matrix elements. Within this approximation the gauge phase appearing in Eq. 42 is taken outside the integral, replacing $\mathbf{r}$ by $\frac{1}{2}(\mathbf{R}_\alpha + \mathbf{R}_\beta)$. The overlap integrals are then given by:

$$\overline{\hat{S}}_{1\alpha,2\beta} \approx \hat{S}_{1\alpha,2\beta}e^{iL_{\alpha\beta}}. \tag{43}$$

Here, $\hat{S}_{1\alpha,2\beta} =_\alpha \langle n_1,l_1,m_1|n_2,l_2,m_2\rangle_\beta$, and $L_{\alpha\beta} = \frac{q}{2\hbar}(\mathbf{A}_\beta - \mathbf{A}_\alpha)\cdot(\mathbf{R}_\alpha + \mathbf{R}_\beta) = \frac{qB_x}{2\hbar}(z_\alpha y_\beta - y_\alpha z_\beta)$. The Hamiltonian matrix elements are approximated as:

$$\overline{\hat{H}}_{1\alpha,2\beta} \approx \frac{1}{2}\left[\hat{H}_{1\alpha,2\beta}e^{iL_{\alpha\beta}} + \hat{H}_{1\beta,2\alpha}e^{iL_{\beta\alpha}}\right], \tag{44}$$

where $\hat{H}_{1\alpha,2\beta} =_\alpha \left\langle n_1,l_1,m_1|\hat{H}|n_2,l_2,m_2 \right\rangle_\beta$. This form guarantees that the Hamiltonian matrix remains Hermitian under the approximation.

All matrix elements in the formulation presented above are calculated analytically. The EH Hamiltonian diagonal matrix elements are set to be equal to the ionization potentials

of the appropriate atomic orbital, $\hat{H}^{EH}_{1\alpha,1\alpha} = I.P._{1\alpha}$, while the off-diagonal elements are given by an average of the corresponding diagonal elements: $\hat{H}^{EH}_{1\alpha,2\beta} = k\frac{\hat{H}^{EH}_{1\alpha,1\alpha}+\hat{H}^{EH}_{2\beta,2\beta}}{2}\hat{S}_{1\alpha,2\beta}$, where, $k = 1.75$ is a parameter chosen to give best fit to experimental data. The overlap matrix is calculated analytically for every set of quantum numbers using a method developed by Guseinov et al[169–173] which is described in appendix A. The matrix elements of the magnetic terms appearing in the Hamiltonian can then be expressed as linear combination of overlap integrals and are thus also calculated without the need to perform numerical integration. The expansion of the magnetic integrals in terms of corresponding overlap integrals is presented, in details, in appendix B.

Before continuing, it should be mentioned that while the current model does take into account the explicit geometry of the system and also some of the details of the system's electronic structure, it remains an effective one-particle model and neglects contributions from electron-electron correlations and coupling to the vibrational degrees of freedom of the molecular device. Furthermore, since the bias potential is assumed to drop sharply at the leads-device junctions and its effect of the energy levels of the device is neglected, the current model is valid only at the low bias regime.

Despite these limitations, the atomistic model presented above can serve as a first-order approximation and reveal some important physical considerations regarding the study of the AB effect at the nanometer scale. In the next chapter we present the magneto-resistance behavior of several studied systems obtained using this formalism.

VII. ATOMISTIC CALCULATIONS - RESULTS

Using the MEHT formalism developed in chapter VI we calculate the conductance of several characteristic atomic and molecular setups that are suggested as promising building blocks for future nanometric magnetoresistance devices based on the AB effect. In the present chapter we present a study the magnetoresistance behavior of these structures as a function of the relevant physical control parameters identified in chapter IV and compare our results to those obtained using the continuum model.

A. Atomic corral

In 1993 a group from IBM was able to confine copper surface electrons to artificially created structures composed of individual iron atoms manipulated on the surface using a STM tip.[16] One of the most intriguing confining structures was that of a perfect ring shaped corral created by the exact positioning of 48 iron atoms on the appropriate sites of the copper(111) surface (See Fig. 1). Using such structures they were able to study the stationary surface electron wave patterns arising due to the confinement, and fascinating phenomena such as the quantum Kondo mirage effect[17] were discovered. In the present study we suggest the utilization of such an atomic corral setup as a nanometer scale AB interferometer.

We consider a corral composed of **monovalent** atoms placed on a semi-conductor surface and coupled to two atomic wires. The whole setup is then placed in a perpendicular homogeneous and constant magnetic field and the conductance between the atomic wire leads through the corral is measured, at the limit of zero bias voltage, as a function of the threading magnetic field. Realizing that the corral itself is also constructed of an atomic wire it is important that we first understand some basic properties of such one-dimensional entities.

Since each atomic site contributes a single valent electron, the number of atoms in the chain, N, must be even to get a closed shell wire. The Fermi energy of the wire has a principal quantum number of $\frac{N}{2}$ which is also the number of nodes the Fermi electrons wave functions have. If the distance between the atomic sites, d, is constant then the separation between the nodes is given by $\frac{Nd}{N/2} = 2d$ and thus the Fermi wavelength is $\lambda_F = 2 \times 2d = 4d$.

We therefore see that for any regular atomic wire composed of monovalent atomic sites the conducting electrons wave length is of the order of four inter atomic distances.

This simple conjecture allows us to divide the symmetric atomic corrals into two prototypes: those having $N = 4n$ and those having $N = 4n + 2$ atoms on the circumference, where n is an integer number. For a $N = 4n$ atomic corral the quantum number of the Fermi wave function of a particle on a ring is an integer: $m_F = k_F r = \frac{2\pi}{\lambda_F}\frac{Nd}{2\pi} = \frac{Nd}{4d} = \frac{N}{4} = n$, and therefore the resonance condition in Eq. 11 is obtained when the magnetic field is off. However, when $N = 4n + 2$, we obtain $m_F = n + \frac{1}{2}$ and resonance is achieved only when $\frac{\phi}{\phi_0} = \frac{l}{2}$ where $l = \pm 1, \pm 2, \cdots$.

A similar picture arises when plotting the wave functions of the Fermi electrons. The complex normalized wave functions of a particle on a ring are given by: $\Psi_{\pm m}(\theta) = \frac{1}{\sqrt{2\pi}} e^{\pm im\theta}$. A linear combination of each doubly degenerate functions having the same quantum number m results in real wave functions of the form $\frac{1}{\sqrt{\pi}}\cos(m\theta)$ and $\frac{1}{\sqrt{\pi}}\sin(m\theta)$. The cosine functions are plotted in Fig. 16 for the two corral prototypes having $m = m_F = \frac{N}{4}$. As can be seen,

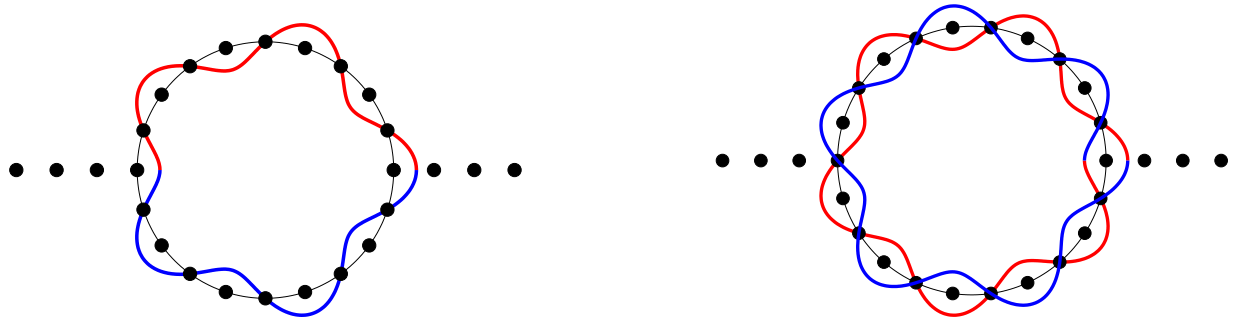

(a) **(b)**

FIG. 16: An illustration of the Fermi cosine wave functions of a particle on a ring shaped corral. Panel a: A $4n$ ring with $n = 5$ creates a stationary solution. Panel b: A $4n + 2$ ring with the same n as before creates a destructive interference between the clockwise (blue) and counterclockwise (red) electron pathways.

for the $4n$ prototype a standing wave is obtained for which both input and output leads are located at non-stationary points. For the $4n + 2$ corral at zero magnetic flux the wave function is not stationary and the output lead is located exactly at a node of the interference

between the clockwise and counter clockwise traveling electrons[‡‡‡].

An alternative explanation for this class devision can be given based upon the energetic structure of the ring. Due to the symmetry of the ring, apart from the lowest energy level, all energy levels of a particle on an uncoupled ring are doubly degenerate. This is illustrated in Fig. 17. When considering a single valent electron per site corral the occupation of the

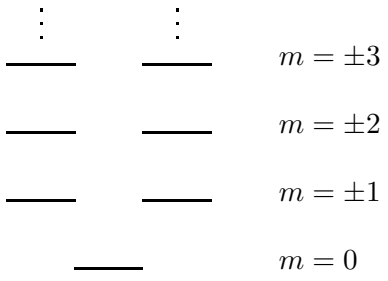

FIG. 17: Energy level scheme of a particle on a ring

energy levels of the $4n$ prototype differs from that of the $4n+2$ prototype. This can be seen

FIG. 18: The occupation of the energy levels of the corral for the $4n$ prototype (left panel) and for the $4n + 2$ prototype (right panel).

in Fig. 18 where the highest occupied molecular orbital (HOMO) occupation is presented for both prototypes. As can be seen in the left panel of the figure, the HOMO occupation of the $4n$ prototype involves two vacancies and thus is suitable for electron conduction when

[‡‡‡] In fact, the interference is destructive not only at the nodes but for every point on the ring and thus this energy level does not exist.

brought to resonance with the leads. While the HOMO occupation of the $4n+2$ prototype (right panel of Fig. 18) is full and therefore does not conduct electrons.

It is interesting to note that the sine function, which is shifted by $\frac{\pi}{2}$ from the cosine counterpart, has both leads located at its nodes as can be seen in Fig. 19. Therefore, at a given leads location and in the absence of a gate potential and a magnetic field only one of the two degenerate energy levels will conduct and the maximum zero bias conductance will be the quantum conductance, g_0.

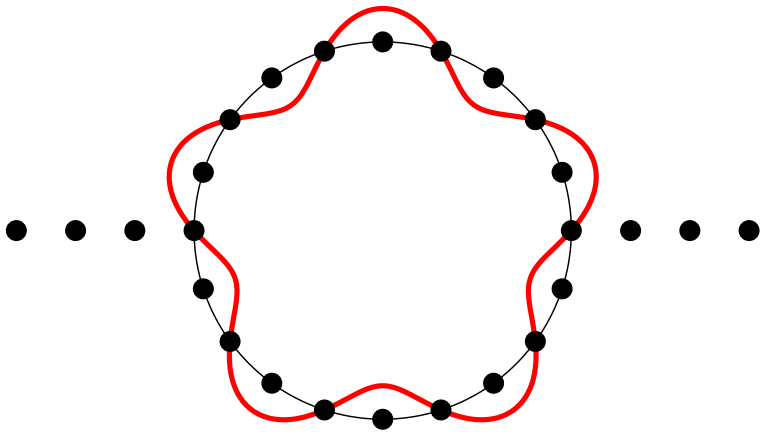

FIG. 19: An illustration of the Fermi sine wave functions of a particle on a ring shaped corral having $N = 4n$ atoms with $n = 5$. Note that the leads are located on the wave function nodes.

This may also be explained by using energy scheme considerations. As mentioned above the HOMO occupation of the $4n$ prototype has two vacancies (one for each spin) and therefore allows only for a single conductance quantum per spin.

After realizing these important features of one-dimensional monovalent atomic wires, we may turn to study atomistic calculations results obtained using the imaginary potentials method within the MEHT formalism as discussed above. In Fig. 20 the conductance through atomic corrals composed of 40 and a 42 copper atoms is plotted[60]. All atoms on the corral are separated by a distance of 2.35Å. The effect of a gate potential was simulated by changing the corral atomic orbital energies by V_g. As discussed above, at zero gate voltage the conductance peak for the $n = 40$ corral is located at the low magnetic field region while for the $n = 42$ corral it is located near the middle of the AB period. Two common features are clearly observed for the two corral prototypes: (a) a large magnetic field ($\sim 500-600$ Tesla) is required to complete a full AB period. (b) The conductance peaks (red spots) shift with

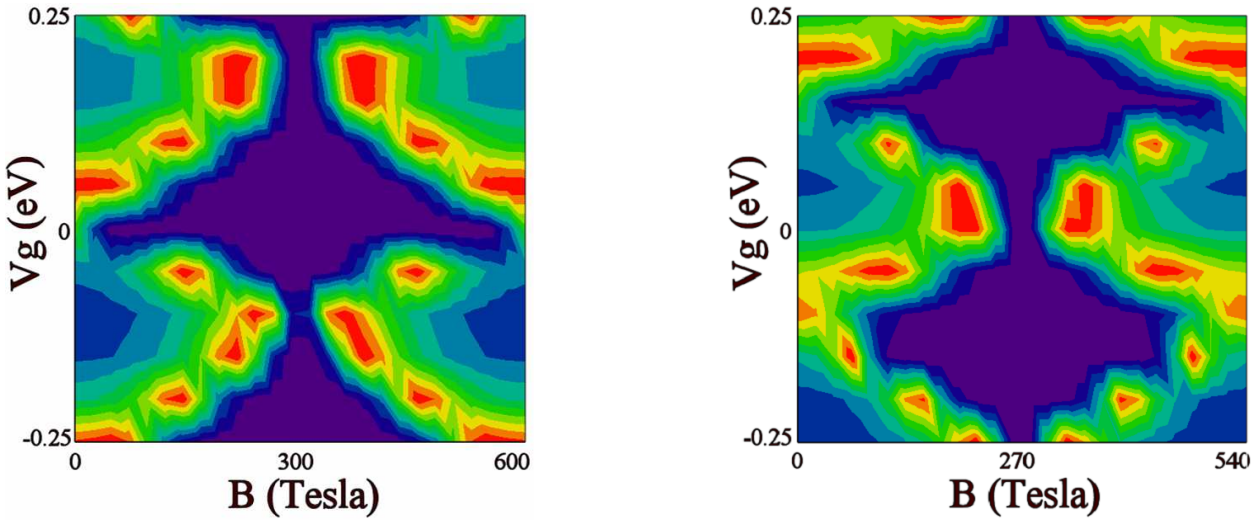

FIG. 20: Conductance as a function of the magnetic field and the gate voltage for a 40 (left panel) and a 42 (right panel) atomic corral composed of copper atoms at $T = 1K$. Color code: Red - $g = g_0$, purple - $g = 0$.

the gate voltage, V_g. The latter effect is analogous to the shift of peaks seen in Fig. 10 for the continuum model as the conducting electron wave number is varied. Therefore, the application of a gate voltage allows the control over the location of the peak conductance. In particular, it can be used to shift the maximal conductance to zero magnetic field for the $N = 4n + 2$ corral prototype and to fine tune the location of the $N = 4n$ peak if slightly shifted from the magnetic field axis origin.

The next step is to control the width of the conductance resonances as a function of the magnetic field. In the continuum model, this was done by reducing the transmission amplitude, ϵ. In the molecular system this can be achieved by increasing the distance between the ring and the edge lead atom closest to the ring. Alternatively, one can introduce an impurity atom at the junctions between the lead and the ring. However, for quantum corrals the former approach seems more realistic.

In Fig. 21 the conductance as a function of the magnetic field is depicted for several values of the leads-ring separation. For each generic corral prototype, a proper gate voltage is applied to ensure maximal conductance at $B = 0$ Tesla. As the lead-ring separation is increased, the lifetime of the energy levels on the ring is increased. This is translated to a sharpening of the switching response to the magnetic field in the magneto-conductance

spectrum. At the highest separation studied we achieve a switching capability of the order of a *single Tesla*, despite the fact the the AB period is comparable to $500 - 600$ Tesla.

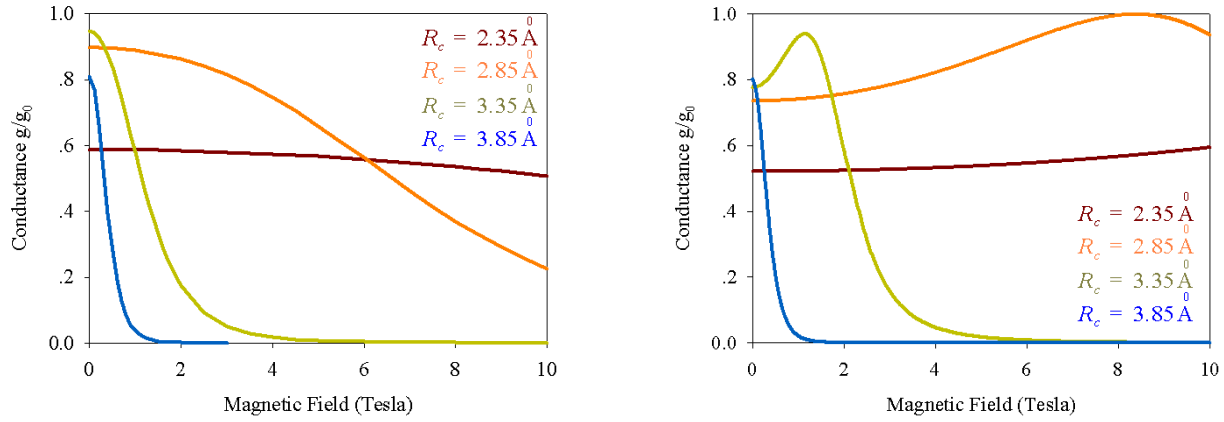

FIG. 21: Conductance as a function of the magnetic field and the contact bond length for a 40 (left panel) and a 42 (right panel) atomic corral composed of copper atoms at $T = 1K$. The gate potential is 0V (left) and -0.132V (right).

Due to the dependence of the AB period on the magnetic flux, the effects discussed above are scalable with the dimension of the ring. For a given leads-corral coupling strength, doubling the cross section of the corral will reduce the switching limit to half its original value. This can be clearly seen in Fig. 22, where the magneto-conductance of several corrals with inter-site spacing of 1Åand at a temperature of 1K is calculated in the WBL with a coupling strength of 0.05eV. For a corral with a diameter of $\sim$ 1.3nm switching occurs at $\sim$ 4 Tesla (solid black curve in the figure). When doubling the diameter of the corral (multiplying the cross section by 4) the switching threshold reduces to $\sim$ 1 Tesla (dashed red line in the figure), as expected. Upon a further increase in the dimensions of the corral (dashed-dotted green curve) the switching threshold reduces respectively.

Summarizing the case of the atomic corral, we have shown that despite the small dimensions, magnetic field switching of conductance through nanometric atomic corrals can be achieved based on the AB effect. The essential procedure is to weakly couple the interferometer to the leads, creating a resonance tunneling junction. Thus the conductance is possible only in a very narrow energy window. The resonant state is tuned by the application of a gate potential so that at $B = 0$ conductance is maximal. The application of a relatively

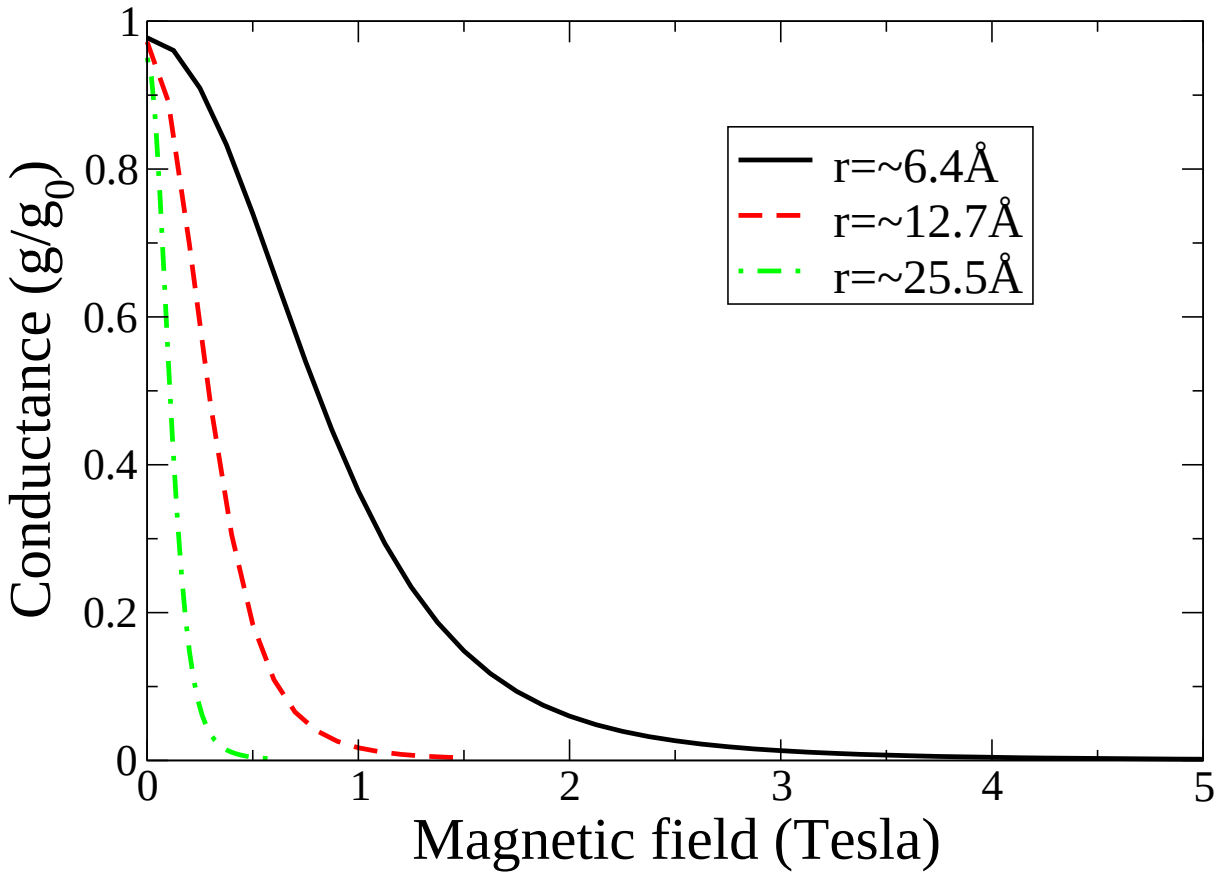

FIG. 22: Magneto-conductance through an atomic corral as a function of the corral dimensions. As the diameter of the corral is doubled from $\sim$ 1.3nm (solid black line) to $\sim$ 2.6nm (dashed red line) the switching threshold reduces by a factor of four. For the largest corral considered (dashed-dotted green line) the switching threshold is $\sim$ 0.5 Tesla for a coupling strength of 0.05eV.

low magnetic field shifts the interferometer level out of resonance, and the conductance is strongly reduced.

B. Carbon Nanotubes

Another interesting and more experimentally accessible molecular system that can serve as a candidate for AB interferometry are Carbon Nanotubes (CNTs). Since their discovery[174] in 1991, and due to their unique mechanical and electronic properties[175–179], CNTs have been investigated in the context of molecular electronics both experimentally[53,140–144,180–185] and theoretically.[186–188] Recently, the AB effect has been measured for single-walled and

multi-walled carbon nanotubes (SWCNT and MWCNT, respectively).[189–191] The MWCNT with relatively large diameter (15nm), exhibits h/e-periodic magnetic flux dependence with $B = 5.8$ Tesla for a full AB period. This result is important, showing that transport is coherent through the tube, in agreement with previous observations.[192] Furthermore, the measurements for the smaller diameter SWCNT indicate that the band structure of the tube depends on the magnetic flux threading it.[191] But, a full AB period and, thus, switching capability, would require magnetic fields of the order of a 1000 Tesla (for a 1nm diameter SWCNT), much higher than those used in the experiment ($B_{max} = 45$ Tesla).

In this section, we suggest a way to switch the conductance through the nanometric cross section of a SWCNT by the application of small (≈ 1 Tesla) magnetic fields parallel to the axis of the tube, using the physical principles discussed above.

Similar to the quantum corral setup, when a magnetic field is applied perpendicular to the cross section of the tube (along its main axis), electron pathways transversing the circular circumference in a clockwise and a counterclockwise manner gain different magnetic phases, and thus AB interference occurs. As the coupling between the CNT and the conducting leads is decreased, a resonant tunneling junction forms. This results in an increase of the electron's lifetime on the CNT and thus in a narrowing of the energy levels width. Using a bias/gate potential it is possible to tune the resonance such that the transmittance is high at zero magnetic field. The application of low magnetic fields shifts the narrow energy level out of resonance. Thus switching occurs at fields much smaller than those required to achieve a full AB cycle.

Two different experimental configurations are considered for this purpose.[61] The first consists of a SWCNT placed on an insulating substrate between two thin conducting contacts (see Fig. 23a) and a bias potential is applied between the contacts. Similar setups have been recently demonstrated experimentally.[37,193–195] In the second configuration a SWCNT is placed on a conducting substrate coupled to a scanning tunneling microscope (STM) tip from above as described schematically in Fig. 23b. The bias potential is applied between the STM tip and the underlying surface. For both configurations we calculate the resulting conductance between the leads, using the MEHT approach, showing that high sensitivity to the magnetic field can be achieved.

For configuration (a) (Fig. 23a) both leads are modeled by atomic conducting wires and the calculations are done using the imaginary potentials method (see chapter VI C), while

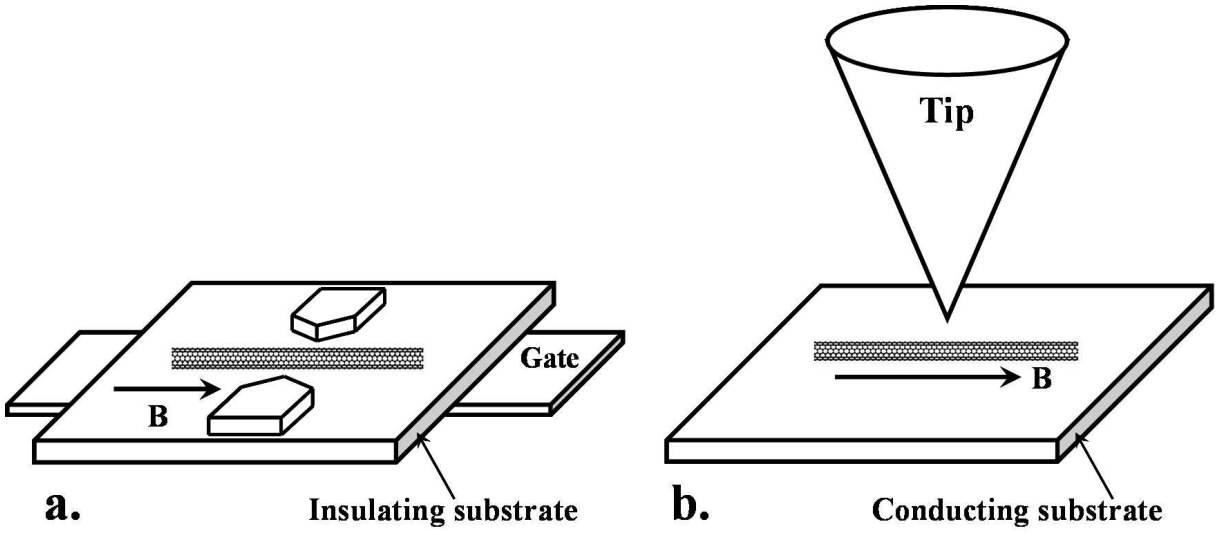

FIG. 23: An illustration of the experimental configurations suggested for measuring the cross sectional magnetoresistance of a CNT. In configuration (a) The SWCNT is placed on an insulating surface between two narrow metallic contacts. While in configuration (b) The SWCNT is placed on a conducting substrate and approached from above by a STM tip.

for configuration (b) (Fig. 23b) the STM tip is modeled by a semi-infinite one dimensional atomic conducting gold wire and the substrate is modeled by a semi-infinite slab of gold crystal and we apply the iterative procedure discussed in section VI B, to obtain the semi-infinite bulk Green's function. The calculations were conducted for a tube four unit cells in length, using minimum image periodic boundary conditions for the passivation of the edge atoms. Such short CNTs have been recently synthesized.[196] Tests on longer tubes reveal the same qualitative picture described below.

In Fig. 24, the conductance through the cross section of a $(24, 0)$ SWCNT, as calculated for configuration (a), is plotted against the external axial magnetic field for several bias potentials. The conductance at zero bias first increases as we switch on the magnetic field (negative magnetoresistance), peaks near $B = 10$ Tesla, and subsequently decreases as the field grows, vanishing at fields above 30 Tesla. The maximum conductance observed, $g/g_0 = 2$, is limited by the number of open channels in the vicinity of the Fermi energy of the SWCNT. In order to achieve switching capability at magnetic fields smaller than 1 Tesla, it is necessary to move the conductance peak to zero magnetic fields and at the same time

reduce its width.

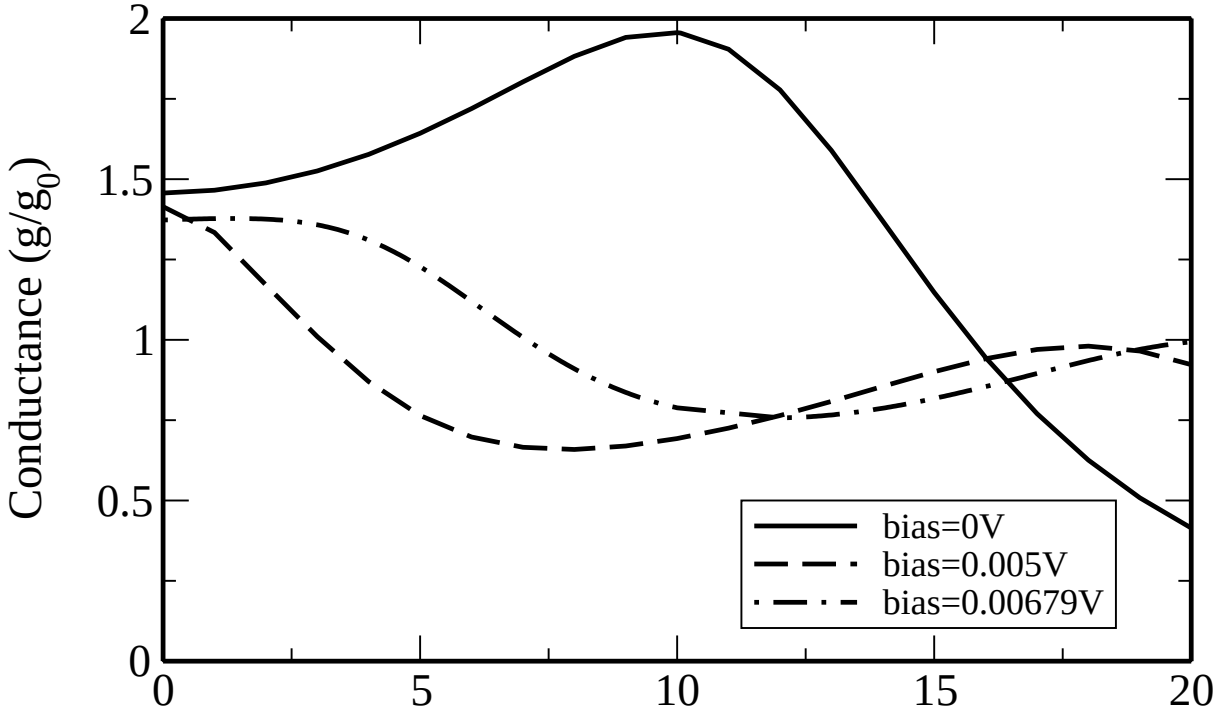

FIG. 24: Conductance versus the magnetic field for several bias potentials as calculated by the MEHT for a $(24, 0)$ SWCNT placed as in configuration (a). The effect of the application of a bias potential on the position of the conductance peaks is depicted at a constant tube-contacts separation of 2.4Å.

When a small bias is applied to the sample the conductance peak splits into a doublet[§§§]. The position of the corresponding peaks depends on the value of the bias and the maximum conductance is reduced by $25\% - 50\%$. As can be seen in the figure, by adjusting the bias potential it is possible to shift one of the conductance peaks toward low values of the magnetic field, such that the conductance is maximal at $B = 0$ Tesla and positive magnetoresistance is achieved. The shift in the conductance peak can be attributed to the change in the energy level through which conductance occurs when a small bias is applied. As a result of this change, the electron momentum is altered resulting in the conductance peak shift observed in the calculation.

[§§§] This is due to the specific way we chose the bias potential drop at the two lead-device junctions as described in chapter VI A. For different bias potential profiles the quantitative details of the calculations would change, however, the qualitative picture would remain the same.

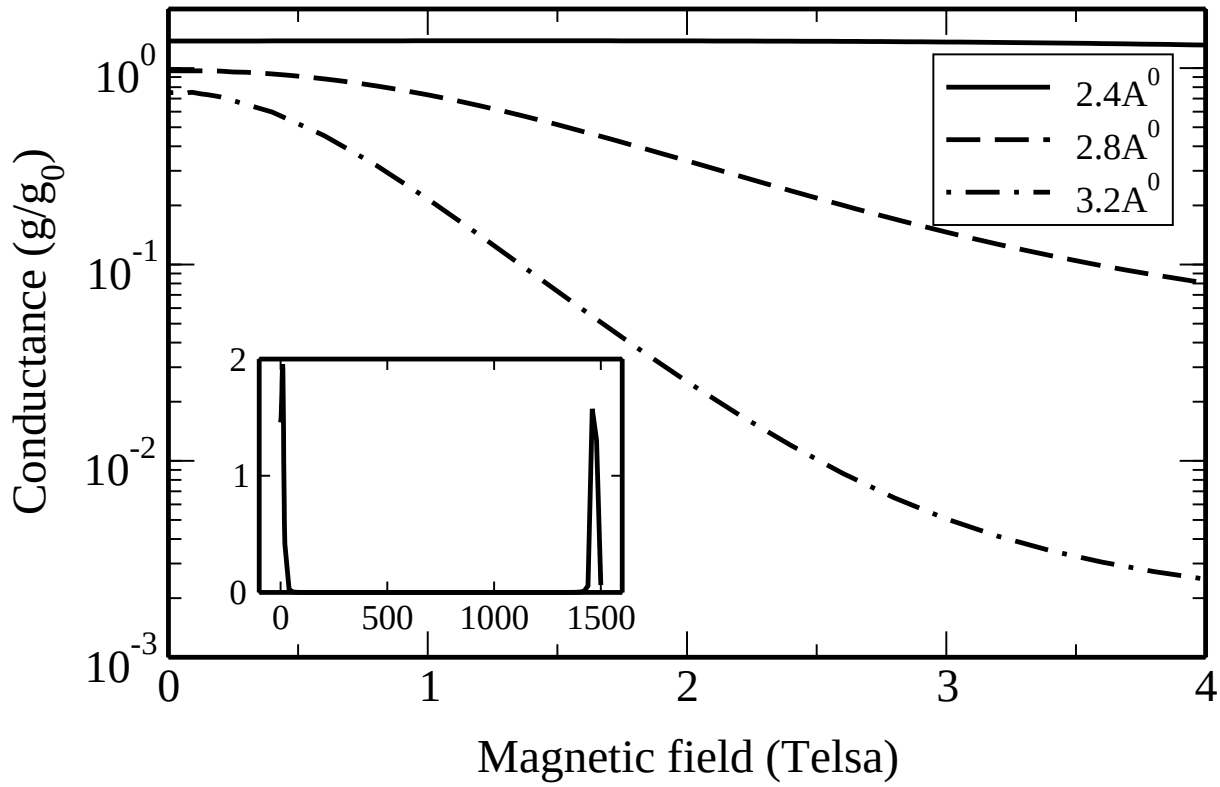

FIG. 25: Conductance versus the magnetic field for several tube-contact separations as calculated by the MEHT for a $(24, 0)$ SWCNT placed as in configuration (a). The effect of an increase in the tube-contact separation is depicted at a constant bias potential of $0.00679V$. Inset: The full AB period for a $(24, 0)$ SWCNT at zero bias potential and tube-contact separation of 2.4Å.

In Fig. 25, the effect of changing the tube-contact separation at constant bias potential is studied. As one increases the separation between the tube and the contacts, their coupling decreases resulting in a reduction of the width of the energy resonances of the SWCNT. Thus, the conductance becomes very sensitive to an applied magnetic field and small variations in the field shift the relevant energy level out of resonance. In the magnetoresistance spectrum, this is translated to a narrowing of the transmittance peaks, similar to the case of the atomic corral discussed in section VII A. For the smallest separation considered (2.4Å), the conductance seems to be constant, on the logarithmic scale, at the magnetic field range shown in the figure, while at the highest separation studied (3.2Å), the width of the conductance peak is comparable to 1 Tesla. At higher magnetic fields (not shown) the conductance of the 2.4Åcase reduces as well.

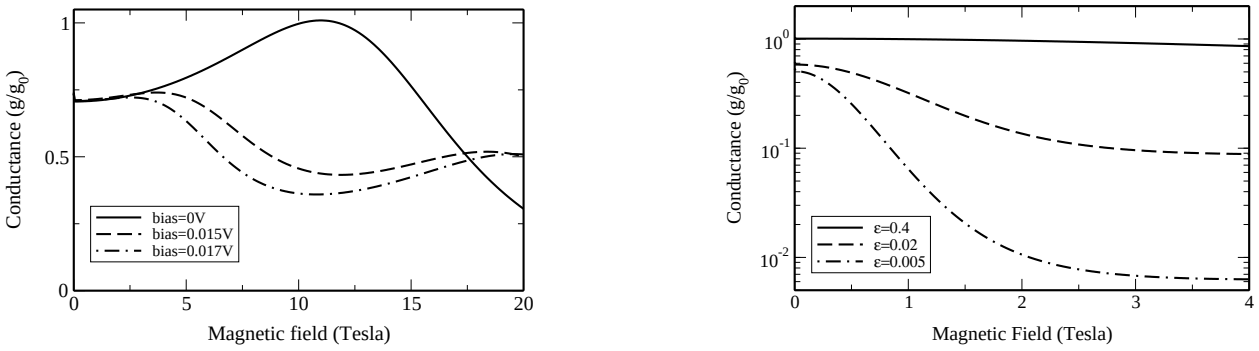

FIG. 26: Magneto-conductance of a ≈ 9.5Åring as calculated using the continuum model. Left panel: The effect of a bias potential on the position of the conductance peaks for $\epsilon = 0.035$. Right panel: The effect of a decrease in the junction transmittance amplitude ϵ at a constant bias potential of $0.0195V$.

In Fig. 26 we present the results of the continuum model (see chapter IV) for a ring of radius $R \approx 9.5$Åand electron wave number approximately equal to that of a Fermi electron in a graphene sheet ($k = 2\pi/3.52$ Å^{-1}). As can be seen in the left panel of the figure, changing the bias potential results in a shift in the position of the transmission peaks similar to the effect seen in the MEHT atomistic calculations (Fig. 24). Furthermore, in the right panel of Fig. 26 we present the effect of reducing the junction transmittance probability which results in a narrowing of the conductance peaks. This corresponds to reducing the coupling (increasing the separation) between the leads and the ring in the MEHT atomistic calculations (Fig. 25). Therefore, although the 1D model does not poses the full 2D characteristics of the CNT we find that it captures all the essential physics to reproduce the results of the conductance through such a complex system. The only fitting parameter we use is the junction transmittance probability, ϵ.

Similar to the corral case, the combined effect of the bias potential and the tube-contacts separation, allows to shift the position of the conductance peak to small magnetic fields while at the same time reduce its width. This is achieved by carefully selecting the values of the bias potential and tube-contacts separation. Under proper conditions, we obtain positive magnetoresistance with a sharp response occurring at magnetic fields comparable to 1 Tesla. This result is significant since it implies that despite the fact that the tube radius is small (~ 1 nm) and the corresponding full AB period requires unrealistic large magnetic fields of

the order of 1500 Tesla (as shown in the inset of Fig. 25), it is possible to achieve magnetic switching at relatively small magnetic fields.

A similar picture arises when considering configuration (b). In Fig. 27 we plot the conductance as calculated for a $(6, 0)$ SWCNT placed between a sharp STM tip and a conducting surface for two bias voltages. We use a smaller diameter CNT in these calculations in order to be able to properly describe the bulky nature of the conducting substrate with respect to the dimensions of the CNT.

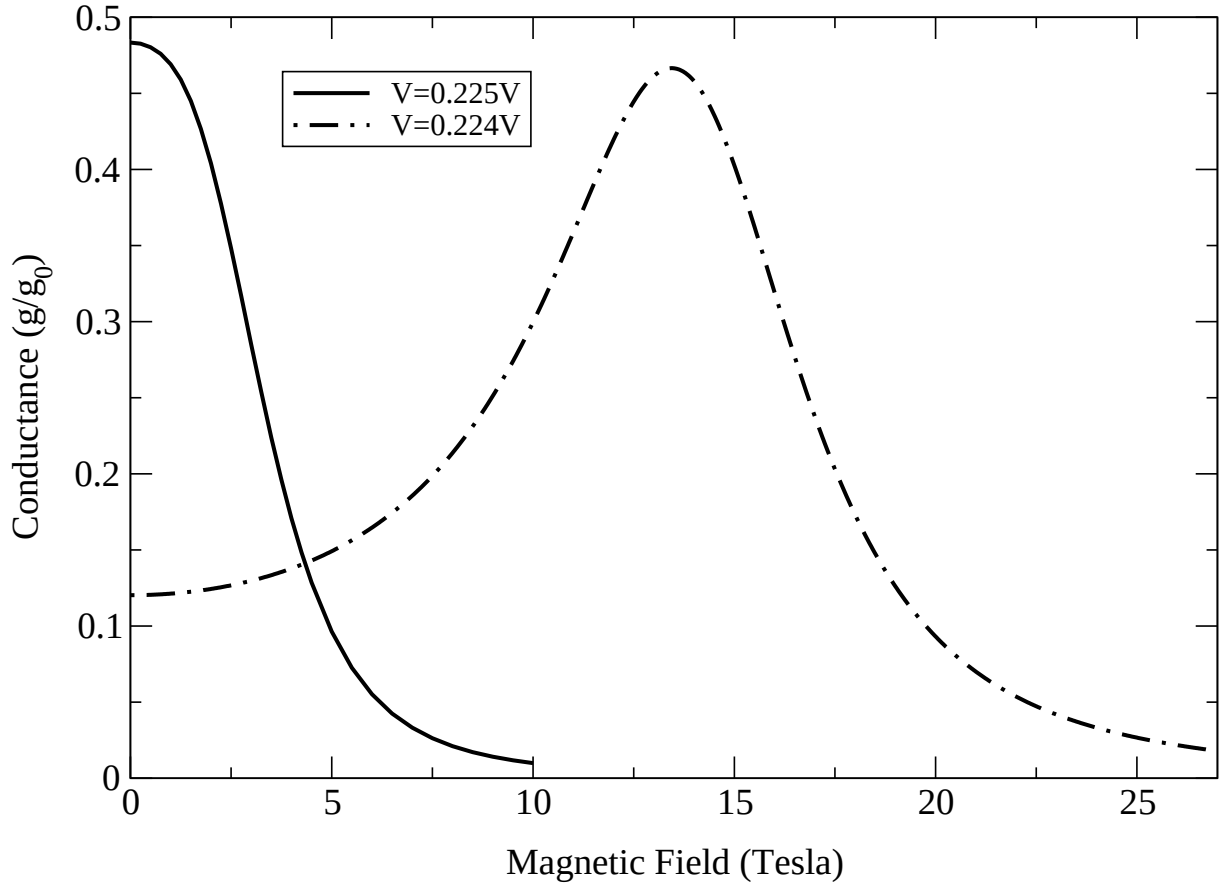

FIG. 27: Conductance as a function of the magnetic field through a $(6, 0)$ CNT as calculated for configuration (b) at different bias voltages. The separation between the CNT and the conducting leads used in this calculation is taken to be 4.1Å.

As can be seen, when a bias voltage of $\sim 0.224V$ is applied the conductance peaks at a magnetic field of ~ 14 Tesla. By changing the bias potential to $\sim 0.225V$ the conductance peak shifts toward zero magnetic field. Under these conditions switching occurs at a magnetic field of ~ 10 Tesla while the full AB period for this system is of the order of $2 \cdot 10^4$ Tesla.

The CNT-leads separation required to achieve high magnetoresistance sensitivity in this configuration is larger than the one needed for configuration (a). This is due to the difference in the CNT diameters and the different leads geometries. As the diameter of the tube becomes smaller, the magnetic field needed to gain a similar AB phase shift grows larger. Therefore, the conductance peaks become wider so that larger CNT-leads separations are required in order to narrow their width. Furthermore, as the lead becomes more bulky its coupling to the CNT needs to be decreased in order to achieve the same magnetoresistance sensitivity.

To conclude the CNT AB interferometry part, we have demonstrated that SWCNTs can be used as magnetoresistance switching devices based on the AB effect. As in the corral setup the essential procedure involves the weak coupling of the SWCNT to the conducting leads in order to narrow the conducting resonances, while at the same time controlling the position of the resonances by the application of a bias potential. The control over the coupling between the SWCNT and the conducting leads in configuration (a) of Fig 23 can be achieved via a fabrication of a set of leads with proper gaps. In configuration (b) of the same figure one needs to control the distance between the STM tip and the CNT and between the substrate and the CNT. The former can be achieved by piezoelectric control and the latter by covering the surface with monolayer/s of an insulating material.

C. Three terminal devices based on polyaromatic hydrocarbon rings

As discussed in chapter V, an interesting case in which magnetic fields provide unique control over the conductance is based on the three-terminal setup. Here, we will study the effects of magnetic field polarity on the selective switching of molecular devices, and show how such devices can be used for parallel logic operations.[62]

We consider a polycyclic aromatic hydrocarbon (PAH) hexagonal ring composed of 48 conjugated benzene units with a diameter of $\sim$ 3nm. Similar PAH molecules have been synthesized[197–199] and studied theoretically,[200–203] and the conductance of related organic molecules attached to gold wires has recently been measured.[18] The molecule, is coupled to three gold atomic wires as shown in Fig. 28, and the geometry of the entire system is optimized using Fletcher-Reeves/Polak-Ribiere conjugate-gradient algorithm applied to the MM+ force field on the HyperChem 6.02 software. The transmittance is computed using

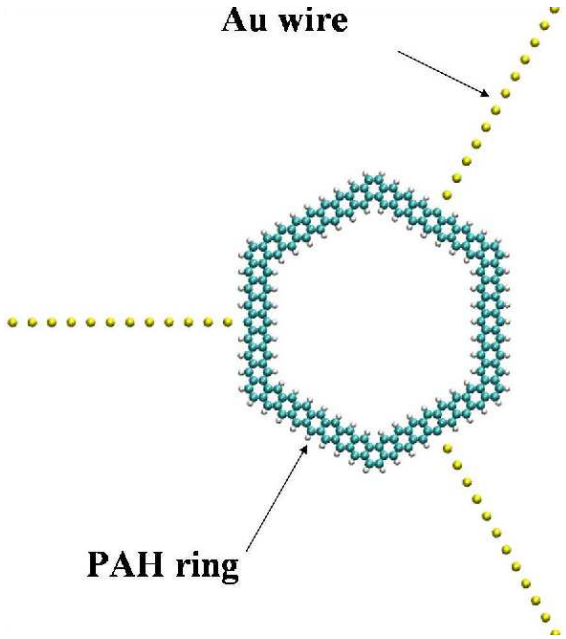

FIG. 28: A realization of a three terminal molecular AB interferometer based on a polyaromatic hydrocarbon molecule coupled to three atomic gold wires.

imaginary absorbing potentials as discussed in chapter VI C.

In Fig. 29 we plot the zero bias conductance of the molecular switch as a function of the magnetic field intensity for both output channels (black and red curves). We focus on the region of realistic magnetic fields (much smaller than the field required to complete a full AB period which is ~ 470 Tesla for a ring with a cross section area of about $8.75nm^2$). A relatively large gate voltage, $V_g = 1.85$V, is needed in order to bring the system into resonance, and the lead-molecule separation is taken to be ~ 3Å.

For zero magnetic field, both channels are semi-opened and the conductance assumes a value of $0.4g_0$ at the selected gate voltage. When a magnetic field of ~ 2.5 Tesla is applied, we observe that one output channel fully opens while the other closes shut. As the polarity of the field changes sign the two output channels interchange their role. Exactly the same characteristics are captured by the continuum model (e.g. green and blue curves of Fig. 29). Therefore, it can be seen that the magnetic field polarity serves as a distributor that streams the electrons to the desired output channel.

Based on this magnetic rectification behavior, it is possible to design a molecular logic gate which processes two different logic operations simultaneously. This can be achieved by

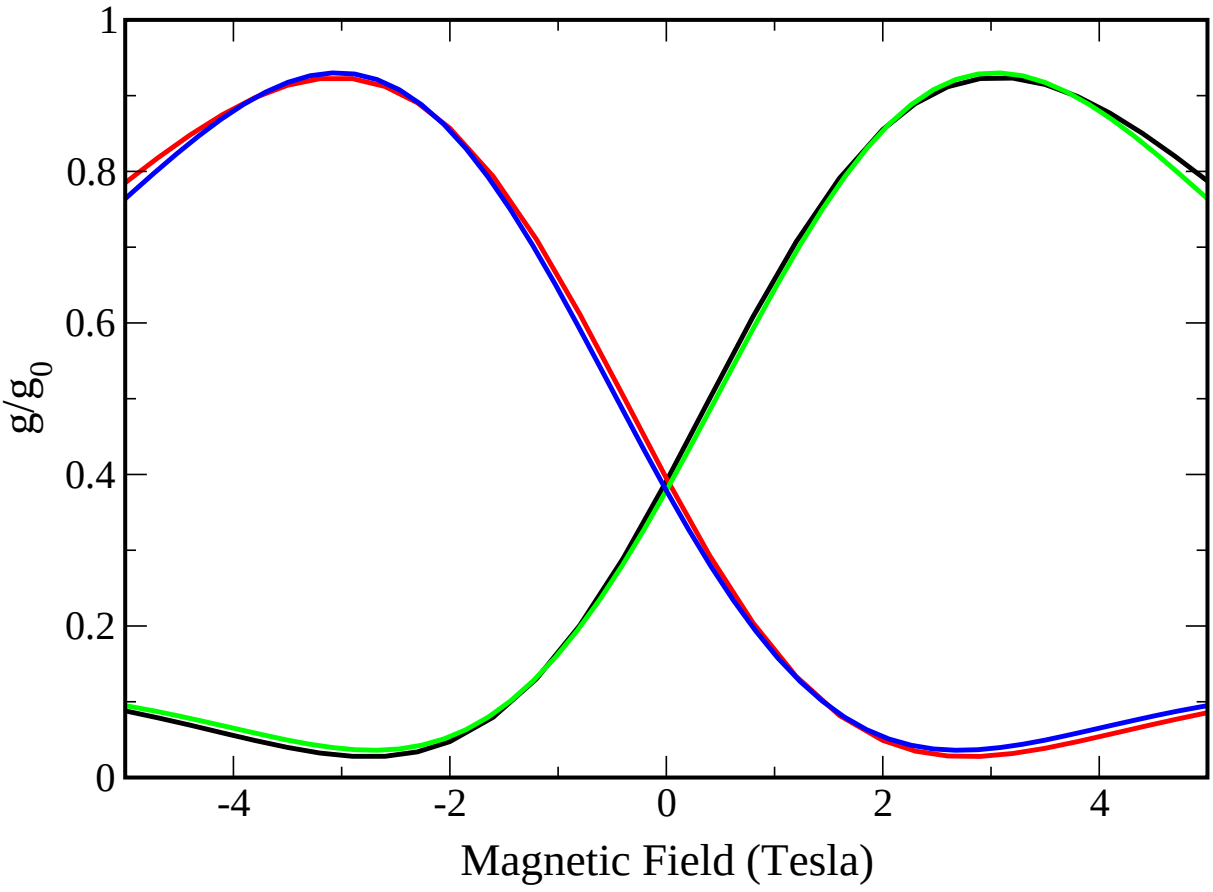

FIG. 29: Magneto-conductance of the three terminal molecular device shown in Fig. 28. Black and red curves - conductance of the upper and lower outgoing terminals, respectively, as calculated by MEHT formalism. Green and blue curves - conductance of the upper and lower outgoing terminals, respectively, as calculated by the continuum model.

choosing one input signal as the bias voltage (V_b) and the other input signal as the magnetic field (B). For the bias input signal, V_b, we mark as $'0'$ the case where $V_b = 0$V and as $'1'$ the case where a small bias is applied. For the magnetic field input signal we mark as $'0'$ the case where $B \approx -3$ Tesla and as $'1'$ the case where $B \approx 3$ Tesla. The output signals are the currents measured at the two outgoing leads marked as I_1 and I_2. The following truth table can be built based on these definitions:

One sees that the output I_1 gives the logic operation V_b && B while the output O_2 gives the logic operation V_b && $\overline{B}$ where the over-line stands for NOT. Even though the conductance peaks are sharp relative to the full AB period, this truth table holds for a wide range of the threading magnetic field intensity $\pm(2-4)$Tesla and is thus suitable for robust

V_b	B	I_1	I_2
0	0	0	0
0	1	0	0
1	0	0	1
1	1	1	0

TABLE I: Truth table for the parallel molecular logic gate.

logic gate operations. Shifting the conductance peaks via the change of the gate potential will give rise to different logic operations of the same setup.

To summarize the current section, it can be seen that single cyclic molecules are promising candidates for the fabrication of magnetoresistance parallel switching and gating devices at feasible magnetic fields. As in the previous discussion, careful fine tuning of experimentally controllable physical parameters allows the selective switching of a single preselected output channel. This feature allows the design of a molecular logic gate, processing two logic operations in parallel.

D. Temperature effects - Broadening of the Fermi-Dirac distributions

The above calculations have been performed assuming a low temperature of 1K (apart for the $(6,0)$ CNT where a temperature of 0.1K was used). However, the effect we report will hold even at higher temperatures. In oder to understand that, we recall that within the Landauer formalism, the temperature effect is taken into account only through the difference of the leads Fermi-Dirac population distributions $f_{L(R)}(E,\mu_{L(R)})$. This difference sets the (temperature dependent) width of the energy band through which conductance occurs. Thus, this width should be narrow enough (the temperature should

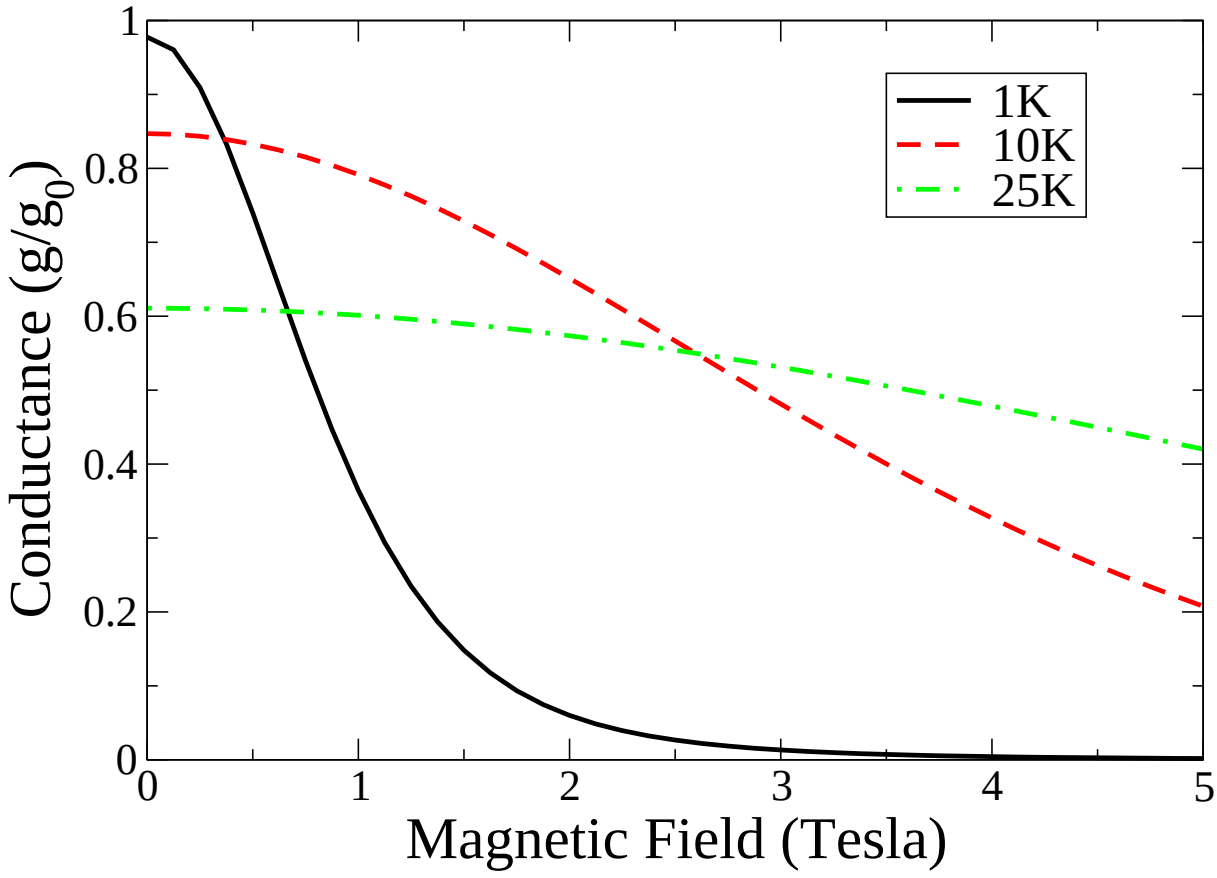

FIG. 30: Magneto-conductance through an atomic corral composed of 40 single electron sites with 1Åspacing at different temperatures. It can be seen that as the temperature rises from 1K (Solid black curve) to 10K (dashed red curve) the device response becomes less sensitive to the magnetic field. At 25K (dashed-dotted green line) the conductivity is almost insensitive to the magnetic field at the low magnetic fields region.

be low enough) in order to resolve the magnetic field splitting of the, originally degenerate, energy levels of the ring. Using Eq. 11, we find that this splitting is given by $\frac{\hbar^2}{2m^\star R^2}\left[\left(-|m_F|-\frac{\phi}{\phi_0}\right)^2-\left(|m_F|-\frac{\phi}{\phi_0}\right)^2\right] = \frac{2\hbar^2 m_F}{m^\star R^2}\frac{\phi}{\phi_0} = \frac{2\hbar^2 k_F}{m^\star R}\frac{\phi}{\phi_0}$. Therefore, the temperature should fulfill the following condition in order for AB switching to be observed: $k_B T < \frac{2\hbar^2 k_F}{m^\star R}\frac{\phi}{\phi_0}$.

Considering an atomic corral with a diameter of $\sim$ 1.3nm and inter-atomic distances of 1Å(40 atomic sites), the normalized magnetic flux at 5 Tesla is, $\frac{\phi}{\phi_0} \approx 1.5\times10^{-3}$, and the Fermi wavelength is $\lambda_F \approx 4$Å, resulting in a Fermi wave number of $k_F = \frac{2\pi}{\lambda_F} \approx \frac{\pi}{2}$ Å^{-1}. Assuming and effective mass of $m^\star = 1$a.u. we get a temperature upper limit of approximately 7K.

This can be seen in Fig. 30 where the magneto-conductance through such a corral is calculated using the WBL at different temperatures. The coupling to both leads is taken to be 0.05eV such that switching occurs at $\sim$ 5 Tesla. As the temperature rises from 1K (Solid black curve in the figure) to 10K (dashed red curve in the figure) the device response becomes less sensitive to the magnetic field even-though an effect is still observable, as predicted. At a higher temperature of 25K (dashed-dotted green line) the conductivity becomes almost insensitive to the magnetic field at the magnetic fields region considered.

VIII. INELASTIC SCATTERING EFFECTS - MODEL

So far, we have neglected inelastic scattering effects in the treatment of AB interferometry in nanometer scale rings. Due to interactions between the conducting electrons and the vibrational modes of the molecular device (or external phonon modes coupled to the system for this matter), the phase of the electrons at each pathway on the ring can be randomized thus reducing coherent interference effects. Therefore, it is important to characterize the relevant physical regime at which inelastic scattering effects are expected to become significant in molecular based electronic interferometers.

A. Hamiltonian

We consider a tight binding model of an atomic corral based interferometer. As before, we regard the case of a single valence electron per atomic site. We assume that the interaction between the electrons and the vibrations occurs on site, namely an electron located at site i will couple to the local vibration of the ith atom.

The Hamiltonian of the system is given by:

$$\hat{H} = \hat{H}_{el} + \hat{H}_{vib} + \hat{H}_{int}, \tag{45}$$

where $\hat{H}_{el}$ is the electronic part of the Hamiltonian, $\hat{H}_{vib}$ is the part of the Hamiltonian describing the vibrational modes of the molecule, and $\hat{H}_{int}$ represents the interaction of the electrons with the vibrations of the molecule.

Before proceeding we shall first give a full description of each of these contributions to the Hamiltonian.

1. The electronic Hamiltonian

The electronic part of the Hamiltonian may be written as a combination of two terms $\hat{H}_{el} = \hat{H}^0_{el} + \hat{H}^{int}_{el}$ where $\hat{H}^0_{el} = \hat{H}^{device}_{el} + \hat{H}^{leads}_{el}$, $\hat{H}^{device}_{el}$ being the electronic Hamiltonian of the isolated corral (or any other device), $\hat{H}^{leads}_{el}$ the electronic Hamiltonian of the bare leads, and $\hat{H}^{int}_{el}$ is the leads-device electronic interaction Hamiltonian. We may write these terms using second quantization operators. For the non interacting electronic Hamiltonian

we have:

$$\hat{H}^0_{el} = \sum_{i,j} t_{i,j} c_i^\dagger c_j + \sum_{l,m \in L,R} \epsilon_{l,m} d_l^\dagger d_m, \tag{46}$$

where $c_i^\dagger$, c_i, are creation and annihilation operators of an electron on site i on the device, and $d_l^\dagger$ and d_l are the creation and annihilation operators of an electron on site l on the relevant lead. $t_{i,j}$ is the hopping integral between site i and site j on the device and $\epsilon_{l,m}$ is the hopping integral between site l and site m on the relevant lead. L and R stand for Left and right leads.

For the interaction part we have:

$$\hat{H}^{int}_{el} = \sum_{l,i} V_{l,i} d_l^\dagger c_i + H.c., \tag{47}$$

where $H.c.$ stands for Hermitian conjugate. The matrix elements of all these terms are evaluated using the MEHT approach presented in chapter VI.

2. The vibrational Hamiltonian - Normal modes of an atomic chain

When considering the vibrational part of the Hamiltonian, $\hat{H}_{vib}$, we allow the device atoms to vibrate around their equilibrium position such that we can describe their vibrations using the harmonic approximation. For the sake of simplicity we also assume that the atoms are confined to move along the circumference such that we can map the problem onto a one-dimensional (1D) chain of coupled harmonic oscillators with periodic boundary conditions as shown in Fig. 31.

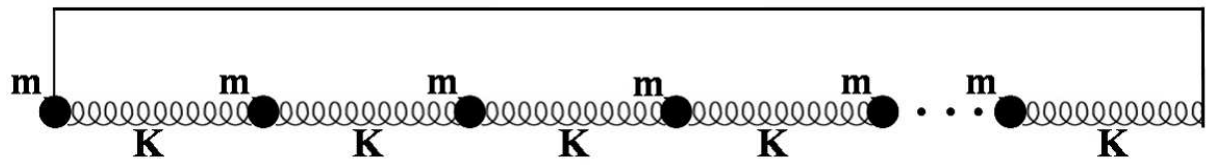

FIG. 31: An illustration of a one-dimensional chain of harmonic springs with periodic boundary conditions. Connecting the rightmost spring with the leftmost mass, is a massless rigid rod of length N times the equilibrium length of the springs, N being the number of springs.

For the case of a corral composed of identical atoms, the masses, m, and spring constants, K, in the 1D chain are the same for all sites. Due to the quadratic nature of the harmonic

potential it is possible to represent such a 1D chain of identical local springs as a set of uncoupled non-identical harmonic springs which describe collective motions of the atoms in the chain. These are usually referred to as the normal vibrational modes of the molecule.

In order to obtain these normal modes we first present the classical vibrational Hamiltonian of the system which can be written as follows:

$$H_{vib} = T_{vib} + V_{vib} = \sum_{k=0}^{N-1} \frac{P_k^2}{2m} + \frac{1}{2}K \sum_{k=0}^{N-1} (x_{k+1} - x_k)^2. \tag{48}$$

Here, N is the number of atoms and $P_k = m\dot{x}_k$ and x_k denote the momentum operator and the deviation from the equilibrium position of atom k along the chain, respectively. We impose periodic boundary conditions on the system such that $x_N = x_0$. For simplicity we define mass-weight coordinates in the following manner $\widetilde{x}_k \equiv \sqrt{m}x_k$. Using this transformation the Hamiltonian can be rewritten in the following form:

$$H_{vib} = \frac{1}{2} \sum_{k=0}^{N-1} \widetilde{P}_k^2 + \frac{1}{2}\omega_0^2 \sum_{k=0}^{N-1} (\widetilde{x}_{k+1} - \widetilde{x}_k)^2. \tag{49}$$

Here, $\widetilde{P}_k = \dot{\widetilde{x}}_k$ and $\omega_0 \equiv \sqrt{\frac{K}{m}}$. It is now possible to write the potential energy term appearing in Eq. 49 using matrix notation:

$$V_{vib} = \frac{1}{2}\omega_0^2 \sum_{k=0}^{N-1} (\widetilde{x}_{k+1} - \widetilde{x}_k)^2 = \omega_0^2 \mathbf{x}^T \hat{W} \mathbf{x}, \tag{50}$$

where

$$\mathbf{x}^T \equiv \left(\widetilde{x}_0,\ \widetilde{x}_1,\ \ldots,\ \widetilde{x}_{N-1} \right) \tag{51}$$

and

$$\hat{W} \equiv \begin{pmatrix} 1 & -\frac{1}{2} & 0 & 0 & 0 & \ldots & 0 & 0 & 0 & -\frac{1}{2} \\ -\frac{1}{2} & 1 & -\frac{1}{2} & 0 & 0 & \ldots & 0 & 0 & 0 & 0 \\ 0 & -\frac{1}{2} & 1 & -\frac{1}{2} & 0 & \ldots & 0 & 0 & 0 & 0 \\ \vdots & \vdots & \vdots & \vdots & \vdots & \ddots & \vdots & \vdots & \vdots & \vdots \\ 0 & 0 & 0 & 0 & 0 & \ldots & -\frac{1}{2} & 1 & -\frac{1}{2} & 0 \\ 0 & 0 & 0 & 0 & 0 & \ldots & 0 & -\frac{1}{2} & 1 & -\frac{1}{2} \\ -\frac{1}{2} & 0 & 0 & 0 & 0 & \ldots & 0 & 0 & -\frac{1}{2} & 1 \end{pmatrix}. \tag{52}$$

Let us now denote by $\hat{U}$ the orthogonal transformation matrix which diagonalizes $\hat{W}$ such that $\widehat{\widetilde{W}} \equiv \hat{U}\hat{W}\hat{U}^T$ is a diagonal matrix, where the diagonal elements are the eigenvalues Ω_k

$(k = 0, \ldots, N-1)$ of $\hat{W}$ and $\hat{U}^T\hat{U} = I$ where I is the unit matrix. We can now write the potential energy as:

$$V_{vib} = \omega_0^2 \mathbf{x}^T \hat{U}^T \hat{U} \hat{W} \hat{U}^T \hat{U} \mathbf{x} = \omega_0^2 \mathbf{q}^T \hat{\widetilde{W}} \mathbf{q} = \omega_0^2 \sum_{k=0}^{N-1} \Omega_k q_k^2 \equiv \sum_{k=0}^{N-1} \frac{1}{2} \omega_k^2 q_k^2, \tag{53}$$

where $\mathbf{q} \equiv \hat{U}\mathbf{x}$ and $\omega_k = \sqrt{2\Omega_k}\omega_0$, and the kinetic energy term as:

$$T_{vib} = \frac{1}{2} \sum_{k=0}^{N-1} \widetilde{P}_k^2 = \frac{1}{2} \sum_{k=0}^{N-1} \widetilde{P}_k \widetilde{P}_k = \frac{1}{2} \sum_{k=0}^{N-1} \dot{\widetilde{x}}_k \dot{\widetilde{x}}_k = \frac{1}{2} \dot{\mathbf{x}}^T \dot{\mathbf{x}} = \frac{1}{2} \dot{\mathbf{x}}^T \hat{U}^T \hat{U} \dot{\mathbf{x}} = \frac{1}{2} \dot{\mathbf{q}}^T \dot{\mathbf{q}}. \tag{54}$$

Finally, the full classical vibrational Hamiltonian is given by:

$$H_{vib} = T_{vib} + V_{vib} = \frac{1}{2} \sum_{k=0}^{N-1} {P_k^{(q)}}^2 + \frac{1}{2} \sum_{k=0}^{N-1} \omega_k^2 q_k^2, \tag{55}$$

where $P_k^{(q)} = \dot{q}_k$ is the canonical momentum conjugated to the coordinates $\{q_k\}$. This Hamiltonian represents a set of N uncoupled harmonic oscillators each with frequency ω_k of the collective normal mode of vibration q_k.

Next we consider the quantum mechanical counterpart of the vibrational Hamiltonian which has exactly the same form as in Eq. 55 except for the canonical momentum which has the following form: $\hat{P}_k^{(q)} = -i\hbar \frac{d}{dq_k}$.

It is now possible to define the raising and lowering operators in the following manner:

$$\hat{b}_k = \frac{1}{\sqrt{2}} \left[\sqrt{\frac{\omega_k}{\hbar}} q_k + i \frac{1}{\sqrt{\hbar\omega_k}} \hat{P}_k^{(q)} \right] \tag{56}$$

for the lowering operator, and

$$\hat{b}_k^\dagger = \frac{1}{\sqrt{2}} \left[\sqrt{\frac{\omega_k}{\hbar}} q_k - i \frac{1}{\sqrt{\hbar\omega_k}} \hat{P}_k^{(q)} \right] \tag{57}$$

for the razing counterpart. These important operators raise or lower the energy of the harmonic oscillator by a single quantum. Finally, the vibrational Hamiltonian may be written in terms of these operators:

$$\hat{H}_{vib} = \sum_{k=0}^{N-1} \hbar\omega_k (b_k^\dagger b_k + \frac{1}{2}). \tag{58}$$

Therefore, using the transformations described above we have represented a set of local coupled vibrations using a set of uncoupled normal vibrations. This resembles the transformation from an electronic basis set of localized atomic orbitals to the representation of orthogonal molecular orbitals.

3. The electron-vibrations interaction term

The last term to consider in the full Hamiltonian is the electron-vibration coupling term. As mentioned, we chose this term to be of the following form:

$$\hat{H}_{int} = M \sum_{i=0}^{N-1} c_i^\dagger c_i (a_i^\dagger + a_i). \tag{59}$$

Using this form we couple an electron on site i, represented by the number operator $N_i \equiv c_i^\dagger c_i$, to the local vibration of atom i, represented by $a_i^\dagger + a_i$. Here $a_i^\dagger$ and a_i are the raising and lowering operators of the local vibrational modes defined as:

$$\begin{cases} a_k \equiv \frac{1}{\sqrt{2}}[\sqrt{\frac{m\omega_0}{\hbar}}\hat{x}_k + i\frac{1}{\sqrt{m\hbar\omega_0}}\hat{P}_k] \\ a_k^\dagger \equiv \frac{1}{\sqrt{2}}[\sqrt{\frac{m\omega_0}{\hbar}}\hat{x}_k - i\frac{1}{\sqrt{m\hbar\omega_0}}\hat{P}_k], \end{cases} \tag{60}$$

such that $(a_k^\dagger + a_k) = \sqrt{\frac{2m\omega_0}{\hbar}}\hat{x}_k = \sqrt{\frac{2\omega_0}{\hbar}}\hat{\widetilde{x}}_k$. Due to the symmetric nature of the device, we consider only a single coupling parameter, M, for the coupling between an electron on site i and the corresponding local vibration. Since we have $q_i = \sum_k U_{ik}\widetilde{x}_k$ and $U^T U = I$ we can write $\widetilde{x}_i = \sum_k U_{ik}^T q_k = \sum_k U_{ki} q_k$. Plugging all this into Eq. 59 we have:

$$\begin{aligned} \hat{H}_{int} &= M \sum_{i=0}^{N-1} c_i^\dagger c_i (a_i^\dagger + a_i) = M \sum_{i=0}^{N-1} c_i^\dagger c_i \sqrt{\frac{2\omega_0}{\hbar}}\hat{\widetilde{x}}_i = M \sum_{i=0}^{N-1} c_i^\dagger c_i \sqrt{\frac{2\omega_0}{\hbar}} \sum_{k=0}^{N-1} U_{ki} q_k \\ &= M \sum_{i,k=0}^{N-1} c_i^\dagger c_i \sqrt{\frac{2\omega_0}{\hbar}} U_{ki} \sqrt{\frac{\hbar}{2\omega_k}} (b_k^\dagger + b_k) = M \sum_{i,k=0}^{N-1} c_i^\dagger c_i \sqrt{\frac{\omega_0}{\omega_k}} U_{ki} (b_k^\dagger + b_k) \\ &= \sum_{i,k=0}^{N-1} M_i^k c_i^\dagger c_i (b_k^\dagger + b_k), \end{aligned} \tag{61}$$

where we have defined $M_i^k \equiv M\sqrt{\frac{\omega_0}{\omega_k}} U_{ki} = M(2\Omega_k)^{-\frac{1}{4}} U_{ki}$.

4. The full Hamiltonian

Collecting all the terms appearing in Eqs. 46, 47, 58, and 61 the full Hamiltonian of the system is given by the following expression:

$$\begin{aligned} \hat{H} = &\sum_{i,j} t_{i,j} c_i^\dagger c_j + \sum_{l,m \in L,R} \epsilon_{l,m} d_l^\dagger d_m + (\sum_{l,i} V_{l,i} d_l^\dagger c_i + H.c.) \\ &+ \sum_{k=0}^{N-1} \hbar\omega_k (b_k^\dagger b_k + \frac{1}{2}) + \sum_{i,k=0}^{N-1} M_i^k c_i^\dagger c_i (b_k^\dagger + b_k). \end{aligned} \tag{62}$$

Hamiltonians similar to the one appearing in Eq. 62 where recently considered in the context of inelastic electron tunneling spectroscopy[150,204–206] and phonon effects in molecular based transistors[207]. The only two free parameters in this Hamiltonian are M - the local coupling strength between an electron on site i and the corresponding local vibration, and ω_0 - the local atomic vibrational frequency. In the next section we use the formalism given in [150] for the calculation of the conductance through the corral in the presence of electron-vibrations interactions.

B. conductance

The calculation of the conductance in the presence of the interaction of the conducting electrons with the vibrational modes of the molecular device is done, as before, within the framework of NEGF formalism.[63,150,208–210] Eq. 17 is still valid for calculating the net current through the device. Nevertheless, the lesser and greater self energies appearing in Eq. 19 have to be replaced by the following expressions:

$$\begin{cases} \Sigma^{<} = \Sigma_L^{<} + \Sigma_R^{<} + \Sigma_{vib}^{<} \\ \Sigma^{>} = \Sigma_L^{>} + \Sigma_R^{>} + \Sigma_{vib}^{>}, \end{cases} \tag{63}$$

which results in the following current formula:

$$I = I_{el} + I_{inel}. \tag{64}$$

Here the elastic part is given by a Landuer-like expression:[150]

$$\begin{aligned} I_{el} &= \frac{2e}{\hbar}\int \frac{dE}{2\pi} Tr\left\{\Sigma_L^{<}(E)G_d^r(E)\left[\Sigma_L^{>}(E)+\Sigma_R^{>}(E)\right]G_d^a(E) - \Sigma_L^{>}(E)G_d^r(E)\left[\Sigma_L^{<}(E)+\Sigma_R^{<}(E)\right]G_d^a(E)\right\} \\ &= \frac{2e}{\hbar}\int \frac{dE}{2\pi}\left[f_L(E,\mu_L) - f_R(E,\mu_R)\right] Tr\left[\Gamma_L(E)G_d^r(E)\Gamma_R(E)G_d^a(E)\right] \end{aligned} \tag{65}$$

and the inelastic contribution is:[150]

$$I_{inel} = \frac{2e}{\hbar}\int \frac{dE}{2\pi} Tr\left[\Sigma_L^{<}(E)G_d^r(E)\Sigma_{vib}^{>}(E)G_d^a(E) - \Sigma_L^{>}(E)G_d^r(E)\Sigma_{vib}^{<}(E)G_d^a(E)\right]. \tag{66}$$

In Eqs. 65 and 66, the retarded GF is modified to include the vibrational coupling in the following manner:

$$\hat{G}_d^r(\epsilon) = \left[\left(G_d^{r0}(\epsilon)\right)^{-1} - \hat{\Sigma}_L^r(\epsilon) - \hat{\Sigma}_R^r(\epsilon) - \hat{\Sigma}_{vib}^r(\epsilon)\right]^{-1} \tag{67}$$

and, as before, the advanced counter part is the Hermitian conjugate of the retarded GF.

C. Self consistent Born approximation

The calculation of the Green's functions discussed above involves the solution of a many body problem. A widely used approximation for solving this problem is the self consistent Born approximation (SCBA).[150,152,211] This approximation effectively sums over an infinite subset of non-crossing diagrams appearing in the pertubative expansion of the GF.

Within the SCBA framework, the vibrational self energy contributions are given as convolutions of the vibrational GFs and the electronic GFs. For the retarded self energy we get (in what follows we use atomic units):

$$\begin{aligned}\left[\Sigma^r_{vib}(E)\right]_{ij} = i\sum_{k_1,k_2} M_i^{k_1} M_j^{k_2} \int [D^<_{k_1k_2}(\omega)G^r_{ij}(E-\omega) + D^r_{k_1k_2}(\omega)G^<_{ij}(E-\omega) \\ + D^r_{k_1k_2}(\omega)G^r_{ij}(E-\omega)]\frac{d\omega}{2\pi} + \delta_{ij}\sum_{k_1,k_2,i'} M_i^{k_1} M_{i'}^{k_2} n^{el}_{i'} D^r_{k_1k_2}(\omega=0)\end{aligned} \tag{68}$$

and for the lesser and greater self energies:

$$\left[\Sigma^{\gtrless}_{vib}(E)\right]_{ij} = i\sum_{k_1,k_2} M_i^{k_1} M_j^{k_2} \int \frac{d\omega}{2\pi} D^{\gtrless}_{k_1,k_2}(\omega)G^{\gtrless}_{ij}(E-\omega). \tag{69}$$

In these expression:

$$n^{el}_i = -i\int \frac{dE}{2\pi} G^<_{ii}(E) \tag{70}$$

and the retarded phonon Green function is given by:

$$D^r(\omega) = \left[(D^r_0(\omega))^{-1} - \Pi^r(\omega)\right]^{-1}, \tag{71}$$

where the unperturbed retarded phonon Greens function is:

$$[D^r_0]_{k,k'}(\omega) = [D^a_0]^\star_{k,k'}(\omega) = \delta_{k,k'}\left[\frac{1}{\omega-\omega_k+i\eta} - \frac{1}{\omega+\omega_k+i\eta}\right], \tag{72}$$

η being the vibrational mode energy broadening due to its relaxation to a thermal bath. This broadening is taken to be constant in the WBL. The retarded phonon SE due to the interaction with the electrons is given by:

$$\left[\Pi^r(\omega)\right]_{ij} = -i\sum_{i_1,i_2} M^i_{i_1} M^j_{i_2} \int \frac{dE}{2\pi}\left[G^<_{i_1,i_2}(E)G^a_{i_2,i_1}(E-\omega) + G^r_{i_1,i_2}(E)G^<_{i_2,i_1}(E-\omega)\right]. \tag{73}$$

The advanced phonon Green function is the conjugate transpose of the retarded one:

$$D^a(\omega) = D^r(\omega)^\dagger, \tag{74}$$

while lesser (and greater) phonon Green function in Eqs. 68 and 69 is given by:

$$D^{\gtrless}(\omega) = D^r(\omega)\Pi^{\gtrless}(\omega)D^a(\omega). \tag{75}$$

The lesser and greater phonon SEs are:

$$\left[\Pi^{\gtrless}(\omega)\right]_{ij} = -i\sum_{i_1,i_2} M^i_{i_1} M^j_{i_2} \int \frac{dE}{2\pi} G^{\gtrless}_{i_1,i_2}(E) G^{\lessgtr}_{i_2,i_1}(E-\omega). \tag{76}$$

Since the evaluation of the self energies involves the electronic GFs which themselves include the self energies, the calculation is done self consistently, using the uncoupled (to the vibrations) GFs as a starting point, until convergence is reached.

D. First Born approximation

In our calculations we use the first Born approximation, which actually can be viewed as the first iteration of the SCBA scheme. Within this approximation we replace the electronic and the vibrational GFs appearing in Eqs. 68 and 69 by their zero order counterparts to get:

$$\begin{aligned}\left[\Sigma^r_{vib}(E)\right]_{ij} = i\sum_k M^k_i M^k_j \int \{&\left[D^<_0\right]_{k,k}(\omega)\left[G^r_0\right]_{ij}(E-\omega) + \left[D^r_0\right]_{k,k}(\omega)\left[G^<_0\right]_{ij}(E-\omega) \\ &+ \left[D^r_0\right]_{k,k}(\omega)\left[G^r_0\right]_{ij}(E-\omega)\}\frac{d\omega}{2\pi} + \delta_{ij}\sum_{k,i'} M^k_i M^k_{i'} n^{el}_{0,i'}\left[D^r_0\right]_{k,k}(\omega=0),\end{aligned} \tag{77}$$

with $n^{el}_{0,i} = -i\int \frac{dE}{2\pi}\left[G^<_0\right]_{ii}(E)$. And for the lesser and greater self energies:

$$\left[\Sigma^{\gtrless}_{vib}(E)\right]_{ij} = i\sum_k M^k_i M^k_j \int \frac{d\omega}{2\pi}\left[D^{\gtrless}_0\right]_{k,k}(\omega)\left[G^{\gtrless}_0\right]_{ij}(E-\omega). \tag{78}$$

The zero order lesser and greater vibrational GFs are given in terms of the retarded and advanced zero order vibrational GFs:

$$\begin{cases} D^<_0(\omega) = F(\omega)\left[D^r_0(\omega) - D^a_0(\omega)\right] sgn(\omega) \\ D^>_0(\omega) = F(-\omega)\left[D^r_0(\omega) - D^a_0(\omega)\right] sgn(\omega), \end{cases} \tag{79}$$

where $sgn(\omega)$ is the sign of ω and $F(\omega)$ is given by:

$$F(\omega) = \begin{cases} N(|\omega|) & \omega > 0 \\ 1 + N(|\omega|) & \omega < 0. \end{cases} \tag{80}$$

In the above equations $N(\omega) = [exp(\omega/k_BT) - 1]^{-1}$ is the Bose-Einstein distribution function, and the zero order electronic GFs are the pure electronic terms without the electron-vibrations interactions as discussed in chapter VI.

The last term in Eq. 77 appears only in finite systems and is referred to as the Hartree term. In our calculations we neglect this term since it contributes a constant shift to the energy levels which can be compensated experimentally by the application of a gate potential.

One should keep in mind that the first Born approximation is a truncation of the self-consistent Born procedure which by itself is an approximation to the solution of the real many-body problem. Therefore, only the low electron-phonon coupling regime can be considered within the framework of this model.

E. Numerical considerations

The computational efforts involved in the calculation of the conductance can be considerably reduced if one notices that at low temperature and in the zero bias limit, the only energy levels contributing to the conductance process are those close to the Fermi energy of the leads (which is tuned in our calculations to equal the Fermi energy of the device). This is true if the energy level spacing is much larger then their width and than the difference in the chemical potentials of the leads. When calculating the conductance through molecular Aharonov-Bohm interferometers it is also necessary to require that the magnetic fields are small with respect to the full AB period such that higher or lower levels do not shift into resonance with the leads in the magnetic field range studied. Fortunately, this is exactly the case for our calculations. Therefore, it is sufficient to take into consideration only the two degenerate energy levels which are tuned into resonance at zero magnetic field. For this we have to transform all our matrices from the atomic basis to the molecular basis and truncate the molecular basis matrices accordingly.

We denote by V the matrix which diagonalizes the device Hamiltonian and overlap matrices such that $\tilde{H}_d = V^\dagger H V$ is a diagonal matrix of the eigenvalues and $V^\dagger S V = I$ where I is the unit matrix.

The transformation of the retarded device GF into the molecular basis set is therefore

given by:

$$\begin{aligned} G_d^r &= \left(ES - H + \frac{1}{2} i\Gamma_L + \frac{1}{2} i\Gamma_R - \Sigma_{vib}^r \right)^{-1} \\ &= \left[\left(V^\dagger\right)^{-1} V^\dagger \left(ES - H + \frac{1}{2} i\Gamma_L + \frac{1}{2} i\Gamma_R - \Sigma_{vib}^r \right) V V^{-1} \right]^{-1} \\ &= \left[\left(V^\dagger\right)^{-1} \left(E - \tilde{H} + \frac{1}{2} i\tilde{\Gamma}_L + \frac{1}{2} i\tilde{\Gamma}_R - \tilde{\Sigma}_{vib}^r \right) V^{-1} \right]^{-1} \\ &= V \left(E - \tilde{H} + \frac{1}{2} i\tilde{\Gamma}_L + \frac{1}{2} i\tilde{\Gamma}_R - \tilde{\Sigma}_{vib}^r \right)^{-1} \hat{V}^\dagger \\ &= V \tilde{G}_d^r V^\dagger, \end{aligned} \tag{81}$$

where we have defined, $\tilde{G}_d^r \equiv \left(E - \tilde{H} + \frac{1}{2} i\tilde{\Gamma}_L + \frac{1}{2} i\tilde{\Gamma}_R - \tilde{\Sigma}_{vib}^r \right)^{-1}$, $\tilde{\Gamma}_{L(R)} \equiv V^\dagger \Gamma_{L(R)} V$, and $\tilde{\Sigma}_{vib}^r \equiv V^\dagger \Sigma_{vib}^r V$. From Eq. 81 we find that the transformation of the retarded GF to the molecular basis set is given by $\tilde{G}_d^r = V^{-1} G_d^r \left(V^\dagger\right)^{-1}$. In a similar manner it is easy to show that $\tilde{G}_d^a = \left(\tilde{G}_d^r\right)^\dagger$.

The current expressions appearing in Eqs. 65 and 66 can be now written in the molecular basis. For the elastic part we have:

$$\begin{aligned} I_{el} = \frac{2e}{\hbar} \int \frac{dE}{2\pi} \left[f_L(E, \mu_L) - f_R(E, \mu_R) \right] \\ Tr \left[(V^\dagger)^{-1} V^\dagger \Gamma_L(E) V V^{-1} G_d^r(E) (V^\dagger)^{-1} V^\dagger \Gamma_R(E) V V^{-1} G_d^a(E) \right], \end{aligned} \tag{82}$$

which by performing a cyclic permutation in the trace multiplication and using the transformations defined above becomes:

$$I_{el} = \frac{2e}{\hbar} \int \frac{dE}{2\pi} \left[f_L(E, \mu_L) - f_R(E, \mu_R) \right] Tr \left[\tilde{\Gamma}_L(E) \tilde{G}_d^r(E) \tilde{\Gamma}_R(E) \tilde{G}_d^a(E) \right]. \tag{83}$$

For the inelastic contribution we can write in a similar manner:

$$I_{inel} = \frac{2e}{\hbar} \int \frac{dE}{2\pi} Tr[\tilde{\Sigma}_L^<(E) \tilde{G}_d^r(E) \tilde{\Sigma}_{vib}^>(E) \tilde{G}_d^a(E) - \tilde{\Sigma}_L^>(E) \tilde{G}_d^r(E) \tilde{\Sigma}_{vib}^<(E) \tilde{G}_d^a(E)], \tag{84}$$

where the lesser and greater self energies transform to the molecular basis set in the same manner the retarded and advanced counterparts do: $\tilde{\Sigma}_{L(R)}^{\gtrless} = V^\dagger \Sigma_{L(R)}^{\gtrless} V$ and $\tilde{\Sigma}_{vib}^{\gtrless} = V^\dagger \Sigma_{vib}^{\gtrless} V$.

The expressions given in Eqs. 77 and 78 apply only for the case where for each vibrational mode k, M^k is a diagonal matrix. When transforming to the molecular basis set we have to rewrite these expressions in a general matrix form:

$$\begin{aligned} \Sigma_{vib}^r(E) = i \sum_k \int M^k \{ \left[D_0^< \right]_{k,k} (\omega) G_0^r(E - \omega) + \left[D_0^r \right]_{k,k} (\omega) G_0^<(E - \omega) \\ + \left[D_0^r \right]_{k,k} (\omega) G_0^r(E - \omega) \} M^k \frac{d\omega}{2\pi}, \end{aligned} \tag{85}$$

where we have omitted the Hartree term, and,

$$\Sigma^{\gtrless}_{vib}(E) = i\sum_k \int \frac{d\omega}{2\pi} M^k \left[D_0^{\gtrless}\right]_{k,k}(\omega) G_0^{\gtrless}(E-\omega) M^k. \tag{86}$$

The transformed self energies are, therefore, given by:

$$\begin{aligned}\tilde{\Sigma}^r_{vib}(E) &= V^\dagger \Sigma^r_{vib}(E) V \\ &= i\sum_k \int \tilde{M}^k \{[D_0^<]_{k,k}(\omega)\tilde{G}_0^r(E-\omega) + [D_0^r]_{k,k}(\omega)\tilde{G}_0^<(E-\omega) \\ &+ [D_0^r]_{k,k}(\omega)\tilde{G}_0^r(E-\omega)\}\tilde{M}^k \frac{d\omega}{2\pi}\end{aligned} \tag{87}$$

and

$$\tilde{\Sigma}^{\gtrless}_{vib}(E) = V^\dagger \Sigma^{\gtrless}_{vib}(E) V = i\sum_k \int \frac{d\omega}{2\pi} \tilde{M}^k \left[D_0^{\gtrless}\right]_{k,k}(\omega)\tilde{G}_0^{\gtrless}(E-\omega)\tilde{M}^k, \tag{88}$$

where $\tilde{M}^k = V^\dagger M^k V$, and $G_0^{\gtrless}$ transform the same as G_0^r. Eqs. 87 and 88 can now be written for each matrix element as:

$$\begin{aligned}\left[\tilde{\Sigma}^r_{vib}\right]_{nm}(E) &= i\sum_k \sum_{pq} \int \tilde{M}^k_{np} \{[D_0^<]_{k,k}(\omega)\tilde{G}^r_{0\ pq}(E-\omega) + [D_0^r]_{k,k}(\omega)\tilde{G}^<_{0\ pq}(E-\omega) \\ &+ [D_0^r]_{k,k}(\omega)\tilde{G}^r_{0\ pq}(E-\omega)\}\tilde{M}^k_{qm}\frac{d\omega}{2\pi}\end{aligned} \tag{89}$$

and

$$\left[\tilde{\Sigma}^{\gtrless}_{vib}\right]_{nm}(E) = i\sum_k \sum_{pq} \int \frac{d\omega}{2\pi} \tilde{M}^k_{np} \left[D_0^{\gtrless}\right]_{k,k}(\omega)\tilde{G}^{\gtrless}_{0\ pq}(E-\omega)\tilde{M}^k_{qm}. \tag{90}$$

We can now truncate the electronic GFs to include as many energy levels as desired. If, for example, we would like to include only two levels in our calculation marked as a and b then the electronic GFs would be truncated as $\tilde{G}_{pq} \rightarrow \tilde{G}_{pq}(\delta_{pa}+\delta_{pb})(\delta_{qa}+\delta_{qb}) = \tilde{G}_{pq}\sum_{i=a}^{b}\sum_{j=a}^{b}\delta_{pi}\delta_{qj}$. For the more general case we have:

$$\tilde{G}_{pq} \rightarrow \tilde{G}_{pq}\sum_{i\in A}\sum_{j\in A}\delta_{pi}\delta_{qj}, \tag{91}$$

where A is the sub block of relevant energy levels included in the conductance calculation.

Finally, plugging the truncated version of the GFs given in Eq. 91 in Eqs. 89 and 90, changing summation indices, and reorganizing the terms, results in the truncated version of the vibrational self energies calculation: Eqs. 87 and 88 can be now written for each matrix

element as:

$$\left[\tilde{\Sigma}^r_{vib}\right]_{nm}(E) = i\sum_k \sum_{pq\in A} \tilde{M}^k_{np}\tilde{M}^k_{qm}\int \{[D_0^<]_{k,k}(\omega)\tilde{G}^r_{0\ pq}(E-\omega) + [D_0^r]_{k,k}(\omega)\tilde{G}^<_{0\ pq}(E-\omega) + [D_0^r]_{k,k}(\omega)\tilde{G}^r_{0\ pq}(E-\omega)\}\frac{d\omega}{2\pi} \tag{92}$$

and

$$\left[\tilde{\Sigma}^{\gtrless}_{vib}\right]_{nm}(E) = i\sum_k \sum_{pq\in A} \tilde{M}^k_{np}\tilde{M}^k_{qm}\int \frac{d\omega}{2\pi}\left[D_0^{\gtrless}\right]_{k,k}(\omega)\tilde{G}^{\gtrless}_{0\ pq}(E-\omega). \tag{93}$$

As mentioned above, in our case due to the confinement, the ring energy levels spacing is large. This spacing is much larger than the width of each energy levels since we are considering low coupling of the device to the leads and of the electrons to the vibrations. Therefore, at low temperatures and for magnetic fields much smaller than the full AB period, the zero bias conductance can be calculated using only the two degenerate energy levels which are in resonance with the leads in the absence of the magnetic field. Thus, using the truncation methodology presented above, the conductance calculation becomes independent of the device dimensions. Furthermore, this procedure reduces the computational time and the required allocated memory, significantly.

IX. INELASTIC SCATTERING EFFECTS - RESULTS

In the previous chapter the basic computational tools that allow the investigation of the conductance through a molecular device in the presence of electron-vibrations interactions were introduced. In the current chapter we shall present results of numerical calculations conducted using these tools, for the magneto-conductance of an atomic corral including the coupling to the vibrations.

We consider a tight binding model of an atomic corral composed of 40 sites. The sites are identical and monovalent such that each site contributes a single electron. Only two sites, which are separated by 180^0, are coupled to the external electronic reservoirs. These reservoirs are treated within the wide band limit[150] and are represented as constant diagonal matrices in the atomic basis set. The only non vanishing element in these matrices is the diagonal element, $\gamma_{L(R)}$, which corresponds to the atomic site coupled to the relevant reservoir. This element has the dimensions of energy and is identified as the coupling strength to the relevant lead. After transforming to the molecular basis set we truncate all matrices to include only two energy levels, as discussed above.

Since the corral is of $4n$ type, it is expected to conduct in the absence of an external magnetic field. The coupling to each of the leads is chosen to be $\gamma_L = \gamma_R = 0.05$eV such that the magneto-conductance switching in the absence of electron-vibrations interactions is obtained at ~ 5 Tesla.

First we investigate the influence of electron-vibrations coupling on the gate voltage dependence of the zero-bias, zero-temperature conductance in the absence of a magnetic field. A similar calculation was recently conducted by Mitra, Aleiner and Millis[207] for a single level coupled to a single vibrational mode. The results obtained in Fig. 11 of reference [207] are reproduced in Fig. 32. Since our calculation is done via numerical integrations, we do not work at absolute zero temperature. Nevertheless, we choose the temperature to be as low as 0.1K such that $\frac{k_B T}{\Gamma} \approx 1.7 \times 10^{-3} << 1$. Thus, for any practical consideration this can be considered as the zero temperature limit. The vibrational frequency, ω_0, is taken to give $\hbar\omega_0 = 0.01$eV, the coupling to the leads is considered to be symmetric such that $\Gamma_L = \Gamma_R = 0.25\hbar\omega_0$ and $\Gamma = \Gamma_L + \Gamma_R = 0.5\hbar\omega_0$, and the width of the vibrational energy levels due to their relaxation to an external thermal bath is taken as $\eta = 2 \times 10^{-4}$eV. We plot the conductance as a function of the gate potential for the case of no vibrational coupling ($\frac{M}{\Gamma}$=0)

and for the case where the coupling of the electron to the nuclear vibrations of the device equals the coupling of the device to the leads ($\frac{M}{\Gamma} = 1$), where M is the coupling strength to the vibrational mode. The latter condition defines the upper limit for the relevance of the pertubative treatment discusses in the last chapter.[207]

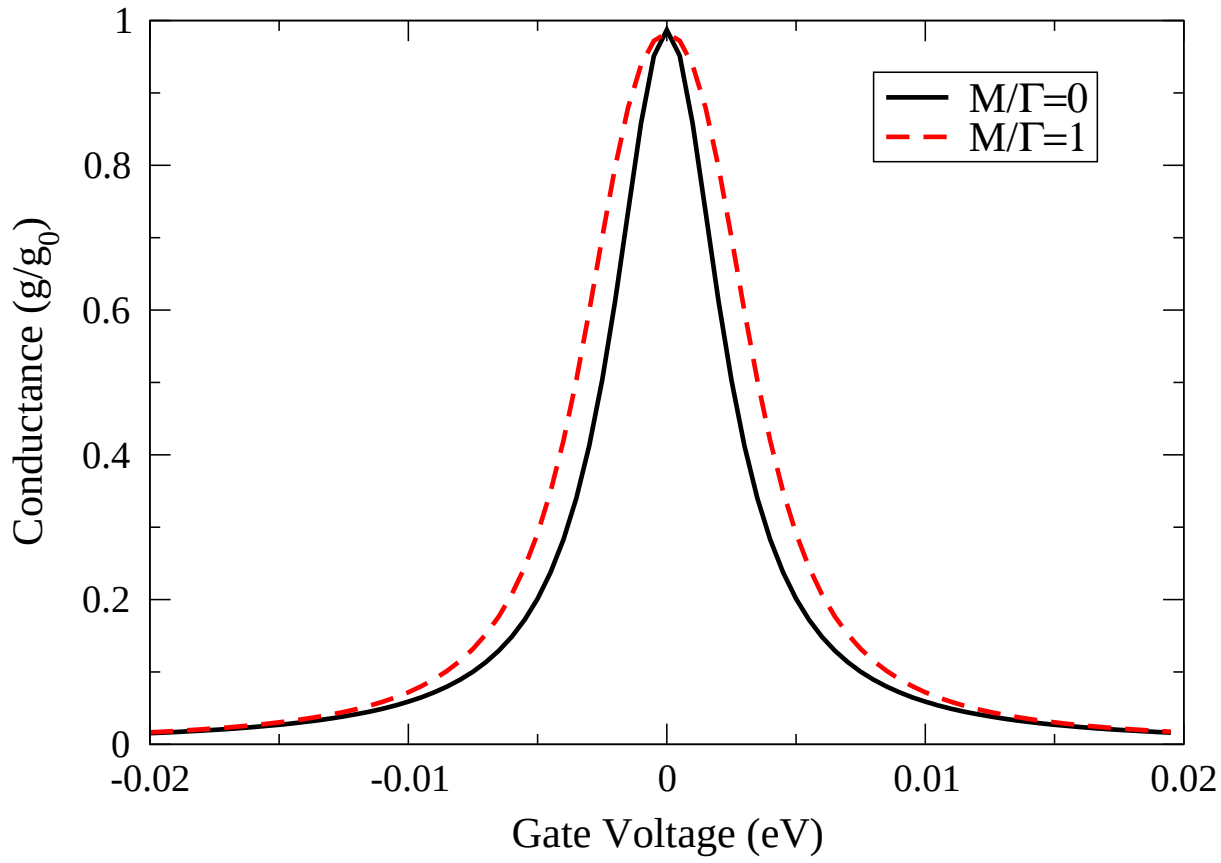

FIG. 32: Conductance vs. gate voltage for a single energy level coupled to two electronic reservoirs in the absence (solid black curve) and the presence (dashed red curve) of an interaction with a single vibrational mode.

As can be seen in Fig. 32 the Lorentzian line-shape of the gate voltage dependent conductance widens due to the interaction with the vibrational mode. Since at equilibrium the zero energy imaginary part of the vibrational contribution to the retarded electronic self energy (Σ^r_{vib}) vanishes, we find that this broadening results mainly from the real part of Σ^r_{vib}.

In Fig. 33 a similar plot is presented for the two degenerate levels of the atomic corral. Here, the frequency of the local vibrations is taken to be $\omega_0 = 0.0124$eV, the vibrational energy levels broadening is $\eta = 2 \times 10^{-4}$eV, the leads coupling parameter is $\gamma = \gamma_L + \gamma_R =$

0.1eV and the coupling of the electrons to the local vibrations equals the coupling to the electronic reservoirs ($\frac{M}{\gamma} = 1$). As can be seen, the picture that arises in the corral case

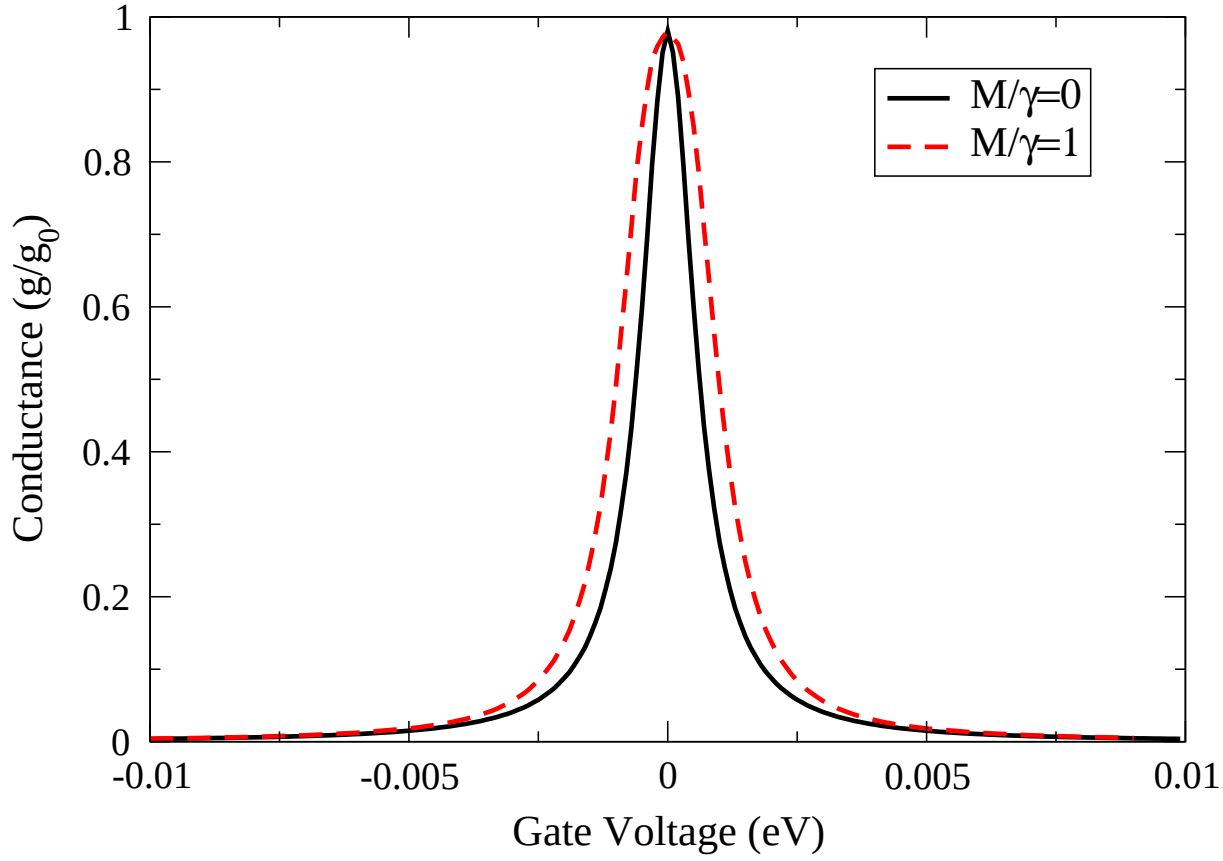

FIG. 33: Conductance vs. gate voltage for a 40 sites atomic corral coupled to two electronic reservoirs in the absence (solid black curve) and the presence (dashed red curve) of electron-vibrations interactions.

(Fig. 33) resembles that obtained for a single level (Fig. 32). The difference in the width of the line-shapes between the two cases results from the fact that the coupling to the electronic reservoirs is different and that the coupling strength of the molecular levels to the vibrations in the corral case is not given by M itself but by a set of transformations involving M.

Next we fix the gate voltage to zero, such that at zero magnetic field the corral fully conducts, and study the magneto-conductance spectrum as a function of the electronic coupling to the local vibrations, M, and the temperature. In Fig. 34 the zero-bias magneto-conductance is plotted at a temperature of $1K$, and $\gamma = 0.1$eV. As can be seen, for extremely low coupling of $M = 0.05\gamma$ (dashed red curve in the figure), we see no significant influence

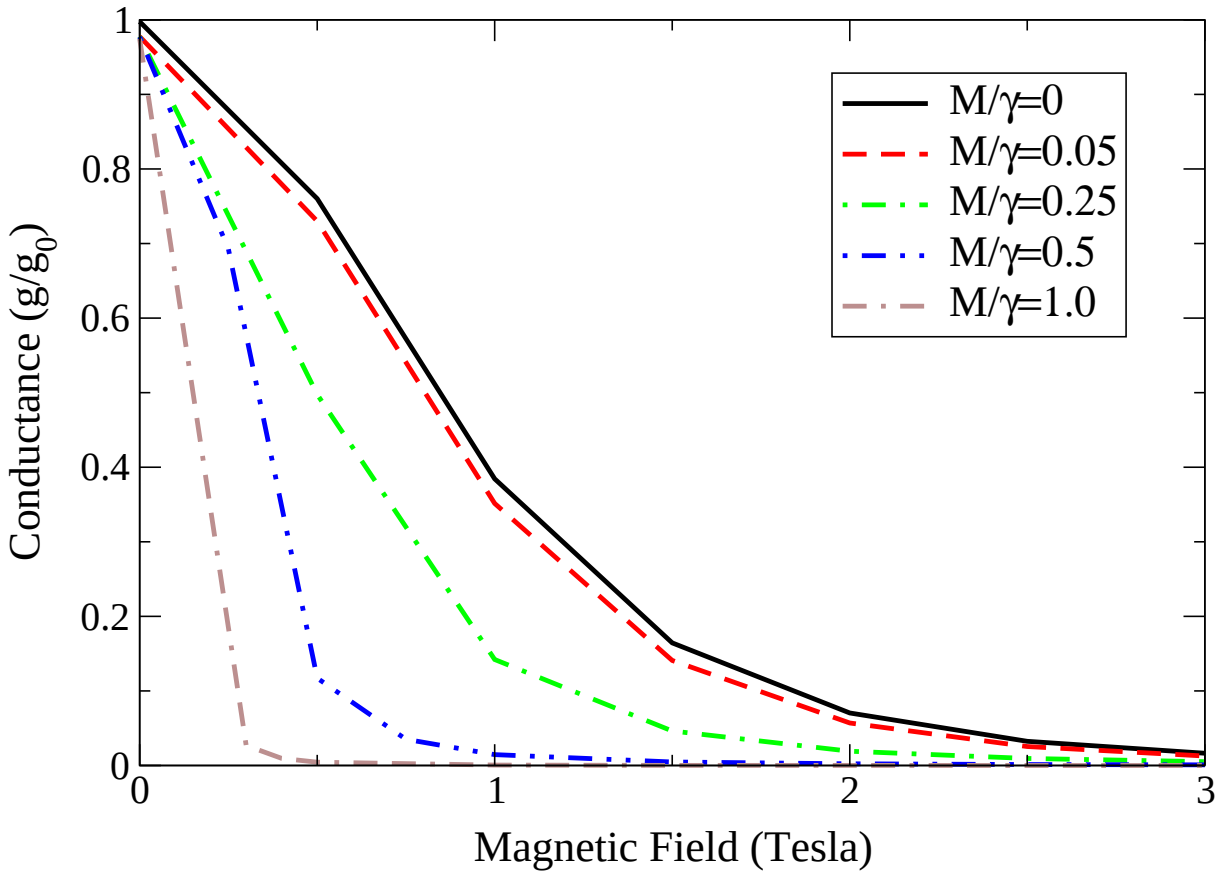

FIG. 34: Low magnetic field magneto-conductance spectrum of a 40 sites corral at 1K and for different vibrational coupling strengths. Black curve - no coupling, dashed red curve - $\frac{M}{\gamma} = 0.05$, dashed dotted green curve - $\frac{M}{\gamma} = 0.25$, dashed double dotted blue curve - $\frac{M}{\gamma} = 0.5$, and double dashed dotted brown curve - $\frac{M}{\gamma} = 1.0$. Here, $\gamma = 0.1$eV.

on the magneto-conductance spectrum. However, unlike the case of the gate voltage dependence, as the vibrational coupling is increased the magneto-conductance spectrum lowers and becomes narrower. When the coupling is set to $M = 0.5\gamma$ the width of the magneto-conductance peak is reduced by a factor of two. This behavior can be explained by the fact that the high transmittance through the corral at zero magnetic field is a result of a delicate interference condition between the different paths that an electron travels while transversing the ring. The coupling to the vibrational modes randomizes the phases of these paths and thus reduces the interference intensity. In the magneto-conductance spectrum this is translated to a narrowing of the peak.

In Fig. 35 we present the electron's transmittance probability appearing in the elastic

conduction term, which is the dominant contribution to the overall conductance at the zero bias limit. As can be seen, when no magnetic field is applied (left panel of the figure), the

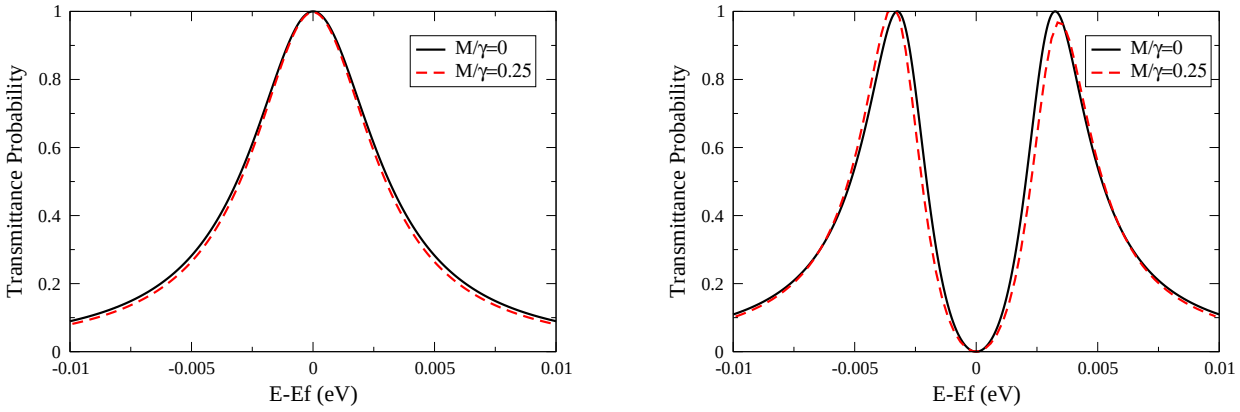

FIG. 35: The energy dependence of the transmittance probability through a 40 sites corral as a function of the coupling to the vibrations at a temperature of 25K (The rest of the parameters are kept unchanged). Left panel: no magnetic field. Right panel: $B = 5$ Tesla. Full black curves - no vibrational coupling, dashed red curves - $\frac{M}{\gamma} = 0.25$

conductance peak slightly narrows (red vs. black curve). Upon applying a magnetic field of 5 Tesla (right panel of Fig. 35), the conductance peak splits into a doublet. Each peak corresponding to one of the two energy levels which are shifted out of resonance due to the magnetic field. An important point to notice is that when coupling the electrons to the vibrations, the separation between the transmittance peak increases at a given magnetic field (black peaks vs. red peaks in the right panel of Fig. 35) and thus the conductance decreases. Again, this shift is attributed mainly to the energy dependence of the real part of $\Sigma^r_{vib}(E)$. The slight asymmetry observed between the two conducting peaks at 5 Tesla with the vibrational coupling is a numerical artifact which does not effect the results.

A similar picture arises when considering the magneto-conductance at a temperature of 10K (Fig. 36). As discussed in section VII D, the magneto-conductance peaks become wider at a higher temperature however the overall effect of the coupling to the vibrational modes remains the same as that presented for the 1K case. It can be clearly seen in Fig. 36 that the conductance reduces even in the absence of the magnetic field. This is a result of the narrowing of the transmittance probability line shape discussed above (see left panel of Fig. 35).

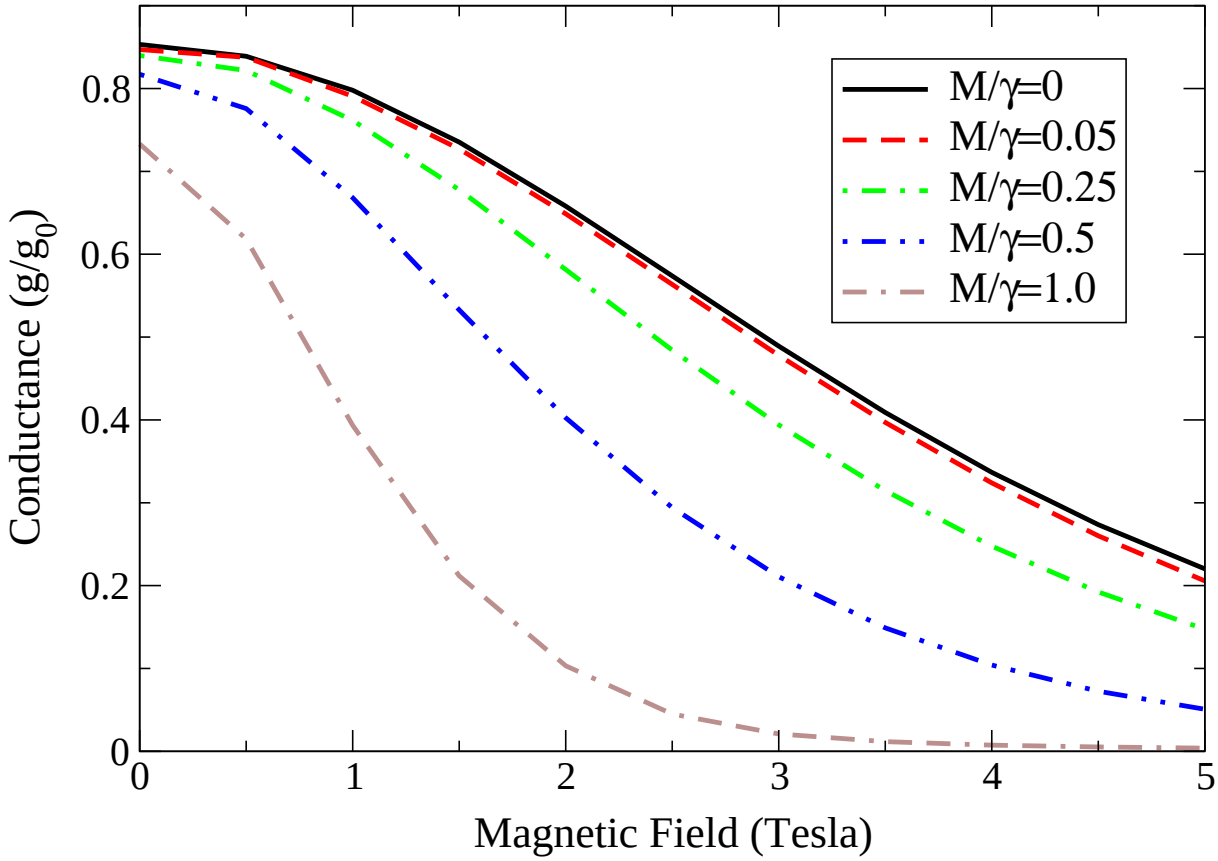

FIG. 36: Low magnetic field magneto-conductance spectrum of a 40 sites corral at 10K and for different vibrational coupling strengths. Black curve - no coupling, dashed red curve - $\frac{M}{\gamma} = 0.05$, dashed dotted green curve - $\frac{M}{\gamma} = 0.25$, dashed double dotted blue curve - $\frac{M}{\gamma} = 0.5$, and double dashed dotted brown curve - $\frac{M}{\gamma} = 1.0$. Here, $\gamma = 0.1$eV.

To summarize, we find, as expected, that the gate voltage dependence of the conductance broadens upon switching on the electron-vibrations coupling. Nevertheless, the magneto-conductance peaks reduce both in size and in width when the vibrational coupling is taken into account. This implies a higher sensitivity of the device to the application of an external magnetic field, than that predicted for the pure coherent case.

X. SUMMARY AND PROSPECTS

Our current understanding of the physics underlying the process of electronic transport through a single molecule, even though highly addressed during the past few decades, is still far from complete. The rapid development in molecular junction fabrication in recent years has opened the way for exciting experimental measurements of conductance through a single molecule. This has drawn a lot theoretical and technological attention for the possible utilization of single molecules as miniature electronic components.

External electric fields are often considered when planning a controllable molecular device. Nevertheless, even though Zeeman splitting and the Kondo effect in single-molecule devices have been studied, the utilization of magnetic fields in molecular electronics has been much less explored. Especially, exploiting the Aharonov-Bohm effect in order to control the conductance through nanometer scale molecular systems was regarded impossible. This is due to the fact that the nanometric dimensions of cyclic molecular systems should, in principle, require extremely high magnetic fields to influence the conductance.

In the present study we have outlined a way to circumvent some technological limitations that where thought to prevent the current application of AB interferometry in nanoscale devices and presented the physical conditions at which significant magnetoresistance effects in nanometer scale electronic interferometers are expected to be found.

Using a one-dimensional scattering theory continuum model of an AB interferometer, which captures the essential physical features of the problem, we have been able to identify and isolate the important parameters that allow the magnetic control over the conductance through a nanometer scale ring. We find that in contrast to the constant strive to gain better coupling between the leads and the molecule within the molecular junction, such magnetic control in the nanometer scale can be obtained only when this coupling is **weak**. This results in a resonant tunneling junction in which the weakly coupled (and thus extremely narrow) energy levels of the ring allow the transport only at well defined resonance energy values. By the application of a **gate** voltage it is possible to tune these resonances such that in the absence of a magnetic field the device will fully conduct. Turning on a magnetic field will shift the narrow doubly degenerate energy levels of the ring out of resonance with the leads and thus will lower the conductance considerably. Therefore, considering the combined effect of increasing the lifetime of the electron on the ring (through the coupling) and controlling

its energy (using a gate voltage), we are able to narrow the magneto-conductance peaks in the AB spectrum while at the same time shift them toward the low magnetic field regime. In such a way it should be possible to gain high sensitivity of the conductance through a nanometer AB ring to a, relatively low ¶¶¶, threading magnetic field. This is despite the fact that the full AB period involves magnetic fields orders of magnitude higher.

The importance of using magnetic fields rather than electric fields to control the conductance was stressed through the example of a three terminal device. In such a device the unique symmetry breaking nature of the magnetic vector potential allows the selective control over the outgoing route of the electron. The magnetic field **polarity** becomes an important control parameter which determines through which of the two outgoing leads the electrons will transverse the ring.

In order to validate the basic principles revealed by the continuum model we have developed a magnetic extended Hückel theory which allows the atomistic calculation of the conductance through molecular setups under the influence of an external magnetic field. Since we are interested in understanding the general physical phenomena, we are less concerned about the fine details of the electronic structure of the system. Therefore, we have chosen to rely on the extended Hückel Hamiltonian for our basic electronic structure calculation. To that we added the appropriate magnetic terms which were evaluated analytically in a gauge invariant Slater type orbitals basis set. We have calculated the transmittance probability using both the imaginary absorbing potentials method and non-equilibrium Green's function techniques. The conductance was then calculated using the Landauer formalism.

Similar to the conclusions drawn by the continuum model, our atomistic calculation results indicate that nanometer scale circular setups such as an atomic corral or the cross section of a carbon nanotube can be used for AB interferometry. At a proper combination of coupling and gate/bias voltage the conductance through the device becomes very sensitive to the magnetic field. Therefore, one can suggest the application of such devices as electromagnetic switches or as miniature magnetic sensors. Furthermore, when extending our interest to the three terminal case and applying the same principles discussed above, we have been able to design a molecular setup that acts as a logic gate that simultaneously processes two different logic operations. One can only imagine the immense possibilities of

¶¶¶ relative to the full AB period and to the current experimental achievable magnetic fields upper limit.

networking such devices.

The important issue of the effect of coupling the electron motion to the nuclear motion on the coherent nature of the transport through nanometer scale electronic interferometers was addressed. Since AB magnetoresistance oscillations have been measured, at low temperatures, even at the micrometer scale, it is evident that inelastic scattering events do not totally wipe out the coherent nature of the transport. The situation is expected to be much better at the nanometer scale where the frequency of inelastic scattering events is much lower under similar conditions. A careful planning of the experimental setup, using materials which have long Fermi wavelength and low decoherence length scales should allow for the measurements of the AB effect even at reasonably high temperatures. Using a tight binding model of an atomic corral, in which local electron-vibrations coupling is allowed, we study the magneto conductance dependence on the vibrational coupling. This model was shown to be equivalent to a problem recently studied, where a set of energy levels was coupled to a set of vibrational modes. We calculated the conductance using non-equilibrium Green's function formalism. The Born approximation was used to solve the many-body problem, which arises in the calculation of the electron-vibrations coupling effects. We have found that the gate dependence of the conductance is broadened due to the vibrational coupling. This result was shown to be expected by considering a reduced model of a single level coupled to a single vibrational mode. Nevertheless, the magneto-conductance trough the device becomes more sensitive to the application of an external magnetic field. This is explained by the fact that the coherent nature of the transport is impaired, which results in reduced interference intensity. We find this effect to sustain even at temperatures as high as 10K for the case studied. Therefore, even in the presence of vibrational coupling it should, in principle, be possible (at least at the low coupling limit studied here) to utilize the nanometer scale electronic interferometers discussed above in future miniaturized electronic devices.

Many important issues are still to be addressed. One of them involves the investigation of coherent effects in the presence of electron-vibrations interactions in the high coupling regime. In this regime it is possible that the coherent nature of the transport would be destroyed such that no interference effects would be observable at all. Therefore, it is important to identify the physical conditions at which such effects are expected to be found. The theoretical investigation of this problem remains a physically interesting issue as well as a theoretical challenge. Another interesting issue still to be taken into consideration is the

effect of the spin of the current carrying particles. Since opposite spins respond differently when entering a magnetic field region, one would expect that their AB interference patterns would be different. Using a three terminal setup, it might be possible to design a spin splitter in which each spin species will transverse the ring through a different outgoing channel. One other point not yet addressed is the comparison of electron versus hole magneto-conductance. It is not obvious that the conclusions drawn above for negative charge carrying particles are valid when considering positive charge conductance. Research in these directions is part of our present and future plans.

APPENDIX A: ANALYTIC EXPRESSIONS FOR THE OVERLAP INTEGRALS OVER REAL SLATER TYPE ORBITALS

There has been a considerable amount of work dedicated to the development of analytic expressions for different integrals over the STO basis set. Usually, the main goal is to express these integrals in terms of the overlap integrals which themselves can be put in simple analytical forms.[169–173,212–223] It is the purpose of the current appendix to give a rigorous and full description of the analytical treatment of the overlap integrals between each pair of arbitrary STOs, while correcting a few typing mistakes that have been published in the literature and may cause some confusion when trying to implement the equations in actual calculations.

We consider the real STO basis set which consists of a set of atomic orbitals of the following form[165,166]:

$$|n,l,m\rangle_\alpha = \frac{(2\zeta)^{n+0.5}}{\sqrt{(2n)!}} r_\alpha^{n-1} e^{-\zeta r_\alpha} \cdot \begin{cases} \frac{(-1)^m}{\sqrt{2}}\left(Y_{l,m}(\theta,\phi) + Y^\star_{l,m}(\theta,\phi)\right) & m>0, \\ Y_{l,0}(\theta,\phi) & m=0, \\ \frac{(-1)^m}{i\sqrt{2}}\left(Y_{l,-m}(\theta,\phi) - Y^\star_{l,-m}(\theta,\phi)\right) & m<0. \end{cases} \tag{A1}$$

Here, (r_α,θ,ϕ) are spherical coordinates centered at the position of atom α, $Y_{l,m}(\theta,\phi)$ are the complex spherical harmonics, $i=\sqrt{-1}$, and $\zeta=\frac{Z-s}{n^\star}$, Z being the nuclear charge, s - a screening constant and $n^\star$ - an effective principal quantum number.

We treat separately three different possibilities of orbital alignments. In section A 1 we consider the overlap of two STOs situated on the same atomic center. Section A 2 is devoted to the overlap expressions between two STOs which are situated upon atomic centers having a common Z axis. Finally, in section A 3, the general overlap integrals are given as a linear combination of appropriate rotations of the coaxial overlap integrals.

It should be noted that the full details of the mathematical treatment leading to the following overlap terms are out of the scope of this work. Presented below are only the final expressions.

1. single center overlap integrals

In the case of the real hydrogen-like orbitals which consist a full orthonormal basis set the single center overlap integrals are simply given by ${}_\alpha\langle n_2,l_2,m_2|n_1,l_1,m_1\rangle_\alpha = \delta_{n_1,n_2}\delta_{l_1,l_2}\delta_{m_1,m_2}$

where δ is the Kronecker delta function. The STOs given in Eq. A1 are a modified version of the real hydrogen-like orbitals which differ from the original orbitals only in the radial part. These node-less functions simplify considerably the calculation of most integrals involved in electronic structure calculations. However, they do not obey the orthonormality condition, and thus their overlap should be considered explicitly.

Due to the fact that the STOs have the same angular behavior as the hydrogen-like orbital, their single center orthonormality with respect to the angular quantum numbers is conserved. Integration with respect to the radial part of the STOs presented in Eq. A1 gives rise to the following overlap expression:

$$ {}_{\alpha}\langle n_2, l_2, m_2 | n_1, l_1, m_1 \rangle_{\alpha} = \left(\frac{2\zeta_1}{\zeta_1 + \zeta_2} \right)^{n_1+0.5} \cdot \left(\frac{2\zeta_2}{\zeta_1 + \zeta_2} \right)^{n_2+0.5} \frac{(n_1+n_2)!}{\sqrt{(2n_1)!(2n_2)!}} \delta_{l_1,l_2} \delta_{m_1,m_2}. \quad \text{(A2)} $$

Next we consider the case of the overlap between two coaxially aligned STOs.

2. Two coaxial center overlap integrals

When the two STOs reside on different atomic centers with a coinciding Z axis, the overlap integral is given by the following expression:[169,170]

$$ {}_{\beta}\langle n_2, l_2, m_2 | n_1, l_1, m_1 \rangle_{\alpha}^{\parallel} = \frac{\delta_{m_1,m_2}(-1)^{l_2-\lambda}}{\sqrt{(2n_1)!(2n_2)!}} \rho^{n_1+n_2+1} (1+t)^{n_1+\frac{1}{2}} (1-t)^{n_2+\frac{1}{2}} \cdot \sum_{\alpha=-\lambda}^{l_1} \sum_{\beta=\lambda}^{l_2} \sum_{q=0}^{\alpha+\beta} g_{\alpha\beta}^{q}(l_1\lambda, l_2\lambda) Q_{n_1-\alpha, n_2-\beta}^{q}(\rho, t), \quad \text{(A3)} $$

where $\rho = \frac{1}{2}R(\zeta_1 + \zeta_2)$, $t = \frac{\zeta_1 - \zeta_2}{\zeta_1 + \zeta_2}$, $\lambda = |m_1|$, and $R = |\mathbf{R}| = [(x_2 - x_1)^2 + (y_2 - y_1)^2 + (z_2 - z_1)^2]^{\frac{1}{2}}$. The functions $g_{\alpha\beta}^{q}(l_1\lambda, l_2\lambda)$ and $Q_{n_1-\alpha,n_2-\beta}^{q}(\rho, t)$ are of the following form:

$$ g_{\alpha\beta}^{q}(l_1\lambda, l_2\lambda) = g_{\alpha\beta}^{0}(l_1\lambda, l_2\lambda) F_q(\alpha + \lambda, \beta - \lambda) \quad \text{(A4)} $$

and

$$ Q_{N_1,N_2}^{q}(\rho, t) = \sum_{m=0}^{N_1+N_2} F_m(N_1, N_2) A_{N_1+N_2+q-m}(\rho) B_{q+m}(\rho t). \quad \text{(A5)} $$

Here $F_m(N_1, N_2)$ is given by ($0 \le m \le N_1 + N_2$):

$$ F_m(N_1, N_2) = N_1! N_2! \sum_{k=0}^{N_2} \frac{(-1)^k}{k!(m-k)!(N_2-k)!(N_1-m+k)!} \quad \text{(A6)} $$

and $A_n(\rho)$ and $B_n(\rho t)$ are the auxiliary functions defined by:

$$A_k(\rho) \equiv \int_1^\infty \mu^k e^{-\rho\mu} d\mu \tag{A7}$$

$$B_k(\rho t) \equiv \int_{-1}^1 \nu^k e^{-\rho t\nu} d\nu \tag{A8}$$

and determined from the following recursion relations:[171,173]

$$A_k(\rho) = \begin{cases} \frac{e^{-r}}{\rho} & k = 0, \\ \frac{1}{\rho}\left[kA_{k-1}(\rho) + e^{-\rho}\right] & k > 0. \end{cases} \tag{A9}$$

Due to numerical stability issues the recursion relation of $B_k(\rho t)$ in the case where $t \neq 0$ is calculated separately for two regions. When $\frac{k}{\rho t} < 1$ the recursion is done upwards in the following manner:

$$B_k(\rho t) = \begin{cases} \frac{2}{\rho t}\sinh(\rho t) & k = 0, \\ \frac{1}{\rho t}\left[kB_{k-1}(\rho t) + (-1)^k e^{\rho t} - e^{-\rho t}\right] & k > 0. \end{cases} \tag{A10}$$

When $\frac{k}{\rho t} \geq 1$ the recursion is done downwards:

$$B_k(\rho t) = \begin{cases} \frac{2}{\rho t}\sinh(\rho t) & k_{top}, \\ \frac{1}{k+1}\left[(\rho t)B_{k+1} + (-1)^k e^{\rho t} + e^{-\rho t})\right] & k < k_{top}. \end{cases} \tag{A11}$$

and the value of k_{top} is determined from the number of significant digits d needed in the calculation of $B_{k \leq k_{max}}(\rho t)$ in the following form:

$$k_{top} \geq \begin{cases} \frac{d}{|log\left(\frac{k_{max}}{\rho t}\right)|} + k_{max} & k_{max} \neq \rho t, \\ k_{max}^2 & k_{max} = \rho t. \end{cases} \tag{A12}$$

When $t = 0$ the expression reduces to:

$$B_k(0) = \frac{1 + (-1)^k}{k + 1}. \tag{A13}$$

Finally, the function $g^0_{\alpha\beta}(l_1\lambda, l_2\lambda)$ in Eq. A4 is given by the following expression:

$$g^0_{\alpha\beta}(l_1\lambda, l_2\lambda) = \frac{1}{2^{l_1+l_2+1}}\left[\frac{(2l_1+1)(l_1-\lambda)!(2l_2+1)(l_2-\lambda)!}{(l_1+\lambda)!(l_2+\lambda)!}\right]^{\frac{1}{2}} \cdot$$
$$\frac{(l_1+\beta)!(-1)^{\frac{1}{2}(l_1-\alpha)+\frac{1}{2}(l_2-\beta)-\lambda}}{[\frac{1}{2}(l_2-\beta)]![\frac{1}{2}(l_2+\beta)]!(\beta-\lambda)!} \cdot \sum_{i=0}^{2\lambda}{}' \frac{(-1)^{\frac{i}{2}}(l_1+\alpha+2\lambda-i)!F_i(\lambda,\lambda)}{\left[\frac{1}{2}(l_1-\alpha)-\lambda+\frac{i}{2}\right]!\left[\frac{1}{2}(l_1+\alpha)+\lambda-\frac{i}{2}\right]!(\alpha+\lambda-i)!}. \tag{A14}$$

The sign $\sum_i' = 0$ designates that the summation is taken only over the even values of i. $g^0_{\alpha\beta}(l_1\lambda, l_2\lambda)$ is assigned the value of zero if at least one of the numbers $l_1 \pm \alpha$ or $l_2 \pm \beta$ is odd. It should be noted that in equations A6 and A14 terms with factorials of negative numbers do not contribute to the summation.

3. General overlap integrals

The full expression for the overlap integral in the general case where the atomic centers do not necessarily reside on coaxially aligned frames is given in terms of the aligned integrals using appropriate rotation relations as follows:[170,172]

$$ {}_\beta\langle n_2, l_2, m_2 | n_1, l_1, m_1 \rangle_\alpha = \sum_{\lambda=0}^{min(l_1,l_2)} T^{*\lambda}_{l_1 m_1, l_2 m_2}(\Theta, \Phi) {}_\beta\langle n_2, l_2, \lambda | n_1, l_1, \lambda \rangle^{\|}_\alpha. \tag{A15}$$

The rotation coefficients $T^{*\lambda}_{l_1 m_1, l_2 m_2}(\Theta, \Phi)$ are given by the following formula (for real STOs):

$$T^{\lambda}_{l_1 m_1, l_2 m_2}(\Theta, \Phi) = \frac{2}{(1+\delta_{\lambda 0})[(1+\delta_{m_1 0})(1+\delta_{m_2 0})]^{\frac{1}{2}}} \sum_{i=-1}^{1}{}' \sum_{L=|l_1-l_2|}^{l_1+l_2}{}' (\epsilon_{m_1,0})^{\delta_{i,\epsilon_{m1,m2}}} C^{l_1 l_2 L}_{i\gamma_1, \gamma_2, i\gamma_1+\gamma_2} C^{l_1 l_2 L}_{\lambda, -\lambda, 0} \left[\frac{2\pi(1+\delta_{M_i 0})}{2L+1}\right]^{\frac{1}{2}} S_{LM_i}(\Theta, \Phi). \tag{A16}$$

Here, $\gamma_i = |m_i|$, $M_i = \epsilon_{m_1,m_2}|i\gamma_1 + \gamma_2|$, and

$$\epsilon_{m_1,m_2} = \begin{cases} 1 & (m_1 \geq 0 \text{ and } m_2 \geq 0) \text{ or } (m_1 < 0 \text{ and } m_2 < 0), \\ -1 & \text{else.} \end{cases} \tag{A17}$$

The coefficients $C^{j_1 j_2 J}_{m_1, m_2, M}$ appearing in Eq. A16 are related to the well known Clebsch-Gordan coefficients $(j_1 j_2 m_1 m_2 | j_1 j_2 J M)$ by the following relation:

$$C^{j_1 j_2 J}_{m_1, m_2, M} = (-1)^{\frac{1}{2}(|m_1|+m_1+|m_2|+m_2+|M|+M)} (j_1 j_2 m_1 m_2 | j_1 j_2 J M) \tag{A18}$$

and $S_{LM_i}(\Theta, \Phi)$ are the real spherical harmonics related to the imaginary counterparts $(Y_{LM_i}(\Theta, \Phi))$ by:

$$S_{lm}(\Theta, \Phi) = \frac{(-i)^{\delta_{m,-|m|}}}{\sqrt{2(1+\delta_{m0})}} (Y_{l|m|}(\Theta, \Phi) + \epsilon_{m,0} Y_{l,-|m|}(\Theta, \Phi)). \tag{A19}$$

This concludes the full description of the expressions involved in the analytic evaluation of the overlap integrals over the real STO basis set.

APPENDIX B: MAGNETIC TERMS INTEGRALS OVER REAL STOS AS LINEAR COMBINATIONS OF OVERLAP INTEGRALS

Extensive work on the analytical evaluation of magnetic multipole moment integrals over Slater type orbitals has been done in the context of the calculation of magnetic properties of molecules[224–229]. Although general, most of the expressions obtained are usually very complex and hard to implement. In the present work, however, only the lowest order moments integrals are necessary to be evaluated. Thus, it is useful to develop simple expressions that will be straightforward to implement in numerical calculations. This appendix is devoted to the development of such expressions. After somewhat tedious mathematical manipulations we find expressions for the magnetic terms integrals as simple linear combinations of the overlap integrals treated in appendix A. A reader interested only in the final expressions is urged to skip the detailed development presented below and use Eqs. B19, B31, and B39.

As noted before, we choose to apply the external magnetic field parallel to the X axis. The resulting magnetic linear and quadratic terms in the Hamiltonian (see Eqs. 40 and 41) are then given by:

$$\hat{H}_{lin}^{mag} = -\frac{\mu_B}{\hbar}\hat{L}_x B_x \tag{B1}$$

and

$$\hat{H}_{quad}^{mag} = \frac{q^2 B_x^2}{8m_e}\left(y^2 + z^2\right). \tag{B2}$$

Considering the London approximation presented in Eq. 44 we need to evaluate integrals of the following form: ${}_\alpha\left\langle n_1, l_1, m_1|\hat{L}_x|n_2, l_2, m_2\right\rangle_\beta$ and ${}_\alpha\langle n_1, l_1, m_1|y^2 + z^2|n_2, l_2, m_2\rangle_\beta$ where the integration is taken over the regular STOs rather than the gauge invariant STOs. Each of the magnetic terms will be treated separately in the following sections.

For the following calculations it shall be useful to rewrite the mathematical expression of the real STOs presented in Eq. A1 in the following form:

$$|n, l, m\rangle = R_n(r)S_{l,m}(\theta, \phi), \tag{B3}$$

where

$$R_n(r) = \frac{(2\zeta)^{n+0.5}}{\sqrt{(2n)!}} r^{n-1} e^{-\zeta r} \tag{B4}$$

and

$$S_{l,m}(\theta,\phi)=\begin{cases}\frac{(-1)^m}{\sqrt{2}}\left(Y_{l,m}(\theta,\phi)+Y^{\star}_{l,m}(\theta,\phi)\right) & m>0,\\ Y_{l,0}(\theta,\phi) & m=0,\\ \frac{(-1)^m}{i\sqrt{2}}\left(Y_{l,-m}(\theta,\phi)-Y^{\star}_{l,-m}(\theta,\phi)\right) & m<0.\end{cases} \tag{B5}$$

Using the following definition of the spherical harmonics:

$$Y_{l,m}\left(\theta,\phi\right)=(-1)^m N_{l,m}P_l^m[\cos(\theta)]e^{im\phi}, \tag{B6}$$

with

$$N_{l,m}\equiv\left[\frac{2l+1}{4\pi}\frac{(l-m)!}{(l+m)!}\right]^{\frac{1}{2}}, \tag{B7}$$

$S_{l,m}(\theta,\phi)$ may alternatively be written as:

$$S_{l,m}(\theta,\phi)=2^{0.5(1-\delta_{|m|,0})}N_{l,|m|}P_l^{|m|}\left[\cos(\theta)\right]\Phi_m(\phi). \tag{B8}$$

Here, the longitudinal angular dependence is given by the well known associated Legendre polynomials $P_l^{|m|}\left[\cos(\theta)\right]$ which can be defined using the following generating equation:

$$P_l^m(x)=\frac{1}{2^l l!}(1-x^2)^{\frac{m}{2}}\frac{d^{l+m}}{dx^{l+m}}(x^2-1)^l \tag{B9}$$

and the azimuthal angular dependence is given by:

$$\Phi_m(\phi)=\begin{cases}\cos(m\phi) & m\geq 0,\\ \sin(|m|\phi) & m<0.\end{cases} \tag{B10}$$

1. Linear magnetic term integrals

For the evaluation of the linear magnetic term integrals ${}_{\alpha}\left\langle n_1,l_1,m_1|\hat{L}_x|n_2,l_2,m_2\right\rangle_{\beta}$ we shall use the angular momentum creation and annihilation operators which relate to the the angular momentum component along the X axis by $\hat{L}_x=\frac{1}{2}\left(\hat{L}_+ + \hat{L}_-\right)$. Since the angular momentum operator operates only on the angular coordinates of the STO orbital it is sufficient to consider its operation on $S_{lm}(\theta,\phi)$ alone. We use the following equations for the operation of the creation and annihilation angular momentum operators on the spherical harmonics:

$$\hat{L}_+Y_{l,m}=\left[l(l+1)-m(m+1)\right]^{\frac{1}{2}}\hbar Y_{l,m+1} \tag{B11}$$

$$\hat{L}_-Y_{l,m}=\left[l(l+1)-m(m-1)\right]^{\frac{1}{2}}\hbar Y_{l,m-1}. \tag{B12}$$

and the relation between the spherical harmonic function and its complex conjugate $Y^{\star}_{l,m} = (-1)^m Y_{l,-m}$, in order to write down their operation on $S_{l,m}(\theta,\phi)$:

$$\hat{L}_+ S_{l,m}(\theta,\phi) = \hbar \begin{cases} \frac{(-1)^m}{\sqrt{2}} \left\{ \left[l(l+1) - m(m+1)\right]^{\frac{1}{2}} Y_{l,m+1}(\theta,\phi) + (-1)^m \left[l(l+1) + m(1-m)\right]^{\frac{1}{2}} Y_{l,1-m}(\theta,\phi) \right\} & m > 0, \\ \sqrt{l(l+1)} Y_{l,1}(\theta,\phi) & m = 0, \\ \frac{(-1)^m}{i\sqrt{2}} \left\{ \left[l(l+1) + m(1-m)\right]^{\frac{1}{2}} Y_{l,1-m}(\theta,\phi) - (-1)^m \left[l(l+1) - m(m+1)\right]^{\frac{1}{2}} Y_{l,m+1}(\theta,\phi) \right\} & m < 0. \end{cases} \tag{B13}$$

$$\hat{L}_- S_{l,m}(\theta,\phi) = \hbar \begin{cases} \frac{(-1)^m}{\sqrt{2}} \left\{ \left[l(l+1) - m(m-1)\right]^{\frac{1}{2}} Y_{l,m-1}(\theta,\phi) + (-1)^m \left[l(l+1) - m(m+1)\right]^{\frac{1}{2}} Y_{l,-m-1}(\theta,\phi) \right\} & m > 0, \\ \sqrt{l(l+1)} Y_{l,-1}(\theta,\phi) & m = 0, \\ \frac{(-1)^m}{i\sqrt{2}} \left\{ \left[l(l+1) - m(m+1)\right]^{\frac{1}{2}} Y_{l,-m-1}(\theta,\phi) - (-1)^m \left[l(l+1) - m(m-1)\right]^{\frac{1}{2}} Y_{l,m-1}(\theta,\phi) \right\} & m < 0. \end{cases} \tag{B14}$$

Thus, the operation of $\hat{L}_x$ on $S_{l,m}$ is given by:

$$\hat{L}_x S_{l,m}(\theta,\phi) = \frac{\hbar}{2}$$
$$\begin{cases} \frac{(-1)^m}{\sqrt{2}} \{ \left[l(l+1) - m(m-1)\right]^{\frac{1}{2}} \left(Y_{l,m-1} - Y^{\star}_{l,m-1} \right) + \left[l(l+1) - m(m+1)\right]^{\frac{1}{2}} \left(Y_{l,m+1} - Y^{\star}_{l,m+1} \right) \} & m > 0, \\ \sqrt{l(l+1)} \left(Y_{l,1} - Y^{\star}_{l,1} \right) & m = 0, \\ \frac{(-1)^m}{i\sqrt{2}} \left\{ \left[l(l+1) - m(m-1)\right]^{\frac{1}{2}} \left(Y_{l,-(m-1)} + Y^{\star}_{l,-(m-1)} \right) + \left[l(l+1) - m(m+1)\right]^{\frac{1}{2}} \left(Y_{l,-(m+1)} + Y^{\star}_{l,-(m+1)} \right) \right\} & m < 0, \end{cases} \tag{B15}$$

where we have denoted $Y_{l,m}(\theta,\phi) \equiv Y_{l,m}$. Using Eq. B5 we can now write this back in terms of the real spherical harmonics:

$$\hat{L}_x S_{l,m}(\theta,\phi) = \frac{-i\hbar}{2} \begin{cases} [l(l+1) - m(m-1)]^{\frac{1}{2}} S_{l,-(m-1)}(\theta,\phi) + [l(l+1) - m(m+1)]^{\frac{1}{2}} S_{l,-(m+1)}(\theta,\phi) & m > 1, \\ [l(l+1) - 2]^{\frac{1}{2}} S_{l,-2}(\theta,\phi) & m = 1, \\ \sqrt{2l(l+1)} S_{l,-1}(\theta,\phi) & m = 0, \\ -\left\{ [l(l+1) - 2]^{\frac{1}{2}} S_{l,2}(\theta,\phi) + \sqrt{2l(l+1)} S_{l,0}(\theta,\phi) \right\} & m = -1, \\ -\left\{ [l(l+1) - m(m-1)]^{\frac{1}{2}} S_{l,-(m-1)}(\theta,\phi) + [l(l+1) - m(m+1)]^{\frac{1}{2}} S_{l,-(m+1)}(\theta,\phi) \right\} & m < -1. \end{cases} \tag{B16}$$

In order to get the operation $\hat{L}_x|n,l,m>$ it is necessary to multiply the expression obtained in Eq. B16 by $R_n(r)$ to get:

$$\hat{L}_x|n,l,m> = \frac{-i\hbar}{2} \begin{cases} -\left\{ [l(l+1) - 2]^{\frac{1}{2}} |n,l,2> + \sqrt{2l(l+1)} |n,l,0> \right\} & m = -1, \\ \sqrt{2l(l+1)} |n,l,-1> & m = 0, \\ [l(l+1) - 2]^{\frac{1}{2}} |n,l,-2> & m = 1, \\ (-1)^{\delta_{m,|-m|}} \left\{ [l(l+1) - m(m-1)]^{\frac{1}{2}} |n,l,-(m-1)> + [l(l+1) - m(m+1)]^{\frac{1}{2}} |n,l,-(m+1)> \right\} & \text{else}, \end{cases} \tag{B17}$$

where we have combined the cases of $m > 1$ and $m < -1$. By the further usage of Kronecker δ-functions this expression reduces to:

$$\begin{aligned} \hat{L}_x|n,l,m> = (-i\hbar)\frac{(-1)^{\delta_{m,|-m|}}}{2}\{(1 - \delta_{m,0} - \delta_{m,1}) [l(l+1) - m(m-1)]^{\frac{1}{2}} |n,l,-(m-1)> + \\ (-\sqrt{2})^{\delta_{m,0}} (\sqrt{2})^{\delta_{m,-1}} [l(l+1) - m(m+1)]^{\frac{1}{2}} |n,l,-(m+1)>\}. \end{aligned} \tag{B18}$$

Finally, the full linear magnetic term integral can be written as a sum of two overlap integrals as follows:

$$
\begin{aligned}
{}_{\beta}\left\langle n_2, l_2, m_2|\hat{L}_x|n_1, l_1, m_1\right\rangle_{\alpha} = (-i\hbar)\frac{(-1)^{\delta_{m_1,|-m_1|}}}{2} \\
\{(1-\delta_{m_1,0}-\delta_{m_1,1})\left[l_1(l_1+1)-m_1(m_1-1)\right]^{\frac{1}{2}}\ {}_{\beta}\left\langle n_2, l_2, m_2|n_1, l_1, -(m_1-1)\right\rangle_{\alpha} + \\
(-\sqrt{2})^{\delta_{m_1,0}}(\sqrt{2})^{\delta_{m_1,-1}}\left[l_1(l_1+1)-m_1(m_1+1)\right]^{\frac{1}{2}}\ {}_{\beta}\left\langle n_2, l_2, m_2|n_1, l_1, -(m_1+1)\right\rangle_{\alpha}\}.
\end{aligned}
\tag{B19}
$$

2. Quadratic magnetic term integrals

Evaluating the quadratic magnetic term integrals involves the calculation of expressions of the form:

$$
\begin{aligned}
{}_{\alpha}\left\langle n_1, l_1, m_1 | y^2 + z^2 | n_2, l_2, m_2 \right\rangle_{\beta} = \\
({}_{\alpha}\langle n_1, l_1, m_1 | y)(y | n_2, l_2, m_2\rangle_{\beta}) + ({}_{\alpha}\langle n_1, l_1, m_1 | z)(z | n_2, l_2, m_2\rangle_{\beta}),
\end{aligned} \tag{B20}
$$

where we have used the fact that the position operators can be operated both on the ket and on the bra of the integral. Thus it is sufficient to calculate expressions of the form $y|n,l,m>$ and $z|n,l,m>$.

For the calculation we shall use the spherical representation of the Cartesian components:

$$
\begin{cases}
x = r\sin(\theta)\cos(\phi) \\
y = r\sin(\theta)\sin(\phi) \\
z = r\cos(\theta)
\end{cases} \tag{B21}
$$

and operate them on the real STOs using Eq. B3:

$$
\begin{cases}
x|n,l,m> = rR_n(r)\sin(\theta)\cos(\phi)S_{l,m}(\theta,\phi) \\
y|n,l,m> = rR_n(r)\sin(\theta)\sin(\phi)S_{l,m}(\theta,\phi) \\
z|n,l,m> = rR_n(r)\cos(\theta)S_{l,m}(\theta,\phi).
\end{cases} \tag{B22}
$$

The operation of r on the radial part of the STOs in Eq. B22 can be easily written as the radial part of a STO with a shifted principal quantum number:

$$
\begin{aligned}
rR_n(r) &= \frac{(2\zeta)^{n+0.5}}{\sqrt{(2n)!}} r^{(n+1)-1} e^{-\zeta r} = \frac{\sqrt{(2n+1)(2n+2)}}{2\zeta} \frac{(2\zeta)^{(n+1)+0.5}}{\sqrt{[2(n+1)]!}} r^{(n+1)-1} e^{-\zeta r} \\
&= \frac{\sqrt{(2n+1)(2n+2)}}{2\zeta} R_{n+1}(r),
\end{aligned} \tag{B23}
$$

where we have used the definition given in Eq. B4

To find the operation of the angular operators on the STOs we use the definition of $S_{l,m}(\theta,\phi)$ given in Eq. B8, the following relations for the associated Legendre polynomials:

$$
\begin{cases}
\cos(\theta)P_l^m[\cos(\theta)] = \left(\frac{l+m}{2l+1}\right) P_{l-1}^m[\cos(\theta)] + \left(\frac{l-m+1}{2l+1}\right) P_{l+1}^m[\cos(\theta)] \\
\sin(\theta)P_l^m[\cos(\theta)] = \left(\dfrac{1}{2l+1}\right) P_{l+1}^{m+1}[\cos(\theta)] - \left(\dfrac{1}{2l+1}\right) P_{l-1}^{m+1}[\cos(\theta)] \\
\qquad\qquad = \left[\dfrac{(l+m)(l+m-1)}{2l+1}\right] P_{l-1}^{m-1}[\cos(\theta)] - \left[\dfrac{(l-m+1)(l-m+2)}{2l+1}\right] P_{l+1}^{m-1}[\cos(\theta)]
\end{cases} \tag{B24}
$$

and the following trigonometric relations:

$$\begin{cases} \sin(\phi)\sin(|m|\phi) = \frac{1}{2}\{\cos[(|m|-1)\phi] - \cos[(|m|+1)\phi]\} \\ \cos(\phi)\sin(|m|\phi) = \frac{1}{2}\{\sin[(|m|-1)\phi] + \sin[(|m|+1)\phi]\} \\ \sin(\phi)\cos(|m|\phi) = \frac{1}{2}\{\sin[-(|m|-1)\phi] + \sin[(|m|+1)\phi]\} \\ \cos(\phi)\cos(|m|\phi) = \frac{1}{2}\{\cos[(|m|-1)\phi] + \cos[(|m|+1)\phi]\}. \end{cases} \tag{B25}$$

First we shall consider the angular part of the operation of z on an STO, $z|n,l,m>$. From Eqs. B22 and B8 it is clear that we have to evaluate the following expression:

$$\cos(\theta)S_{l,m}(\theta,\phi) = 2^{0.5(1-\delta_{|m|,0})}N_{l,|m|}\cos(\theta)P_l^{|m|}[\cos(\theta)] \begin{cases} \cos(m\phi) & m \geq 0, \\ \sin(|m|\phi) & m < 0. \end{cases} \tag{B26}$$

Using the relation given in Eq. B24 this can be written as:

$$\cos(\theta)S_{l,m}(\theta,\phi) = 2^{0.5(1-\delta_{|m|,0})}N_{l,|m|}\left[\left(\frac{l+|m|}{2l+1}\right)P_{l-1}^{|m|} + \left(\frac{l-|m|+1}{2l+1}\right)P_{l+1}^{|m|}\right] \begin{cases} \cos(m\phi) & m \geq 0, \\ \sin(|m|\phi) & m < 0, \end{cases} \tag{B27}$$

where we have denoted $P_l^m \equiv P_l^m[\cos(\theta)]$. When multiplying and dividing $P_{l-1}^{|m|}$ by $N_{l-1,|m|}$ and $P_{l+1}^{|m|}$ by $N_{l+1,|m|}$ this can be rewritten as:

$$\cos(\theta)S_{l,m}(\theta,\phi) = \frac{N_{l,|m|}}{N_{l-1,|m|}}\left(\frac{l+|m|}{2l+1}\right)S_{l-1,m}(\theta,\phi) + \frac{N_{l,|m|}}{N_{l+1,|m|}}\left(\frac{l-|m|+1}{2l+1}\right)S_{l+1,m}(\theta,\phi), \tag{B28}$$

which in turn reduces to:

$$\cos(\theta)S_{l,m}(\theta,\phi) = n_{l,m}^1 S_{l-1,m}(\theta,\phi) + n_{l+1,m}^1 S_{l+1,m}(\theta,\phi). \tag{B29}$$

Defining $n_{l,m}^1 \equiv \sqrt{\frac{(l-m)(l+m)}{(2l-1)(2l+1)}}$. Therefore, the full operation of z on a STO is given by a combination of Eqs. B3, B23 and B29 which yields:

$$z|n,l,m> = \frac{\sqrt{(2n+1)(2n+2)}}{2\zeta}\left[n_{l,m}^1|n+1,l-1,m> + n_{l+1,m}^1|n+1,l+1,m>\right]. \tag{B30}$$

The resulting integral can be written as a linear combination of four overlap integrals:

$$
\begin{aligned}
{}_{\beta}\left\langle n_2, l_2, m_2|z^2|n_1, l_1, m_1\right\rangle_{\alpha} = & \frac{\sqrt{(2n_1+1)(2n_1+2)(2n_2+1)(2n_2+2)}}{4\zeta_1\zeta_2} \\
& [n^1_{l_1,m_1} n^1_{l_2,m_2}\ {}_{\beta}\left\langle n_2+1, l_2-1, m_2|n_1+1, l_1-1, m_1\right\rangle_{\alpha} + n^1_{l_1+1,m_1} n^1_{l_2,m_2}\ {}_{\beta}\left\langle n_2+1, l_2-1, m_2|n_1+1, l_1+1, m_1\right\rangle_{\alpha} + \\
& n^1_{l_1,m_1} n^1_{l_2+1,m_2}\ {}_{\beta}\left\langle n_2+1, l_2+1, m_2|n_1+1, l_1-1, m_1\right\rangle_{\alpha} + n^1_{l_1+1,m_1} n^1_{l_2+1,m_2}\ {}_{\beta}\left\langle n_2+1, l_2+1, m_2|n_1+1, l_1+1, m_1\right\rangle_{\alpha}]. \quad \text{(B31)}
\end{aligned}
$$

We now turn to calculate the operation $y|n,l,m>$. Similar to what presented above, the angular operation is given by:

$$
\sin(\theta)\sin(\phi)S_{l,m}(\theta,\phi) = 2^{0.5(1-\delta_{|m|,0})} N_{l,|m|}\sin(\theta)P_l^{|m|}\left[\cos(\theta)\right]\sin(\phi)\Phi_m(\phi). \quad \text{(B32)}
$$

As before, by using Eq. B24 the longitudinal part can be written as:

$$
\begin{aligned}
& N_{l,|m|}\sin(\theta)P_l^{|m|}\left[\cos(\theta)\right] = \\
& \pm\left[\frac{(l\pm|m|+1)(l\pm|m|+2)}{(2l+1)(2l+3)}\right]^{\frac{1}{2}} N_{l+1,|m|\pm1}P_{l+1}^{|m|\pm1}[\cos(\theta)] \mp \left[\frac{(l\mp|m|)(l\mp|m|-1)}{(2l-1)(2l+1)}\right]^{\frac{1}{2}} N_{l-1,|m|\pm1}P_{l-1}^{|m|\pm1}[\cos(\theta)]. \quad \text{(B33)}
\end{aligned}
$$

The trigonometric relations presented in Eq. B25 give the following result for the azimuthal part:

$$
\begin{aligned}
\sin(\phi)\Phi_m(\phi) = & \begin{cases} \sin(\phi)\cos(m\phi) & m\geq 0, \\ \sin(\phi)\sin(|m|\phi) & m<0. \end{cases} = \frac{1}{2}\begin{cases} \sin[-(|m|-1)\phi]+\sin[(|m|+1)\phi] & m\geq 0, \\ \cos[(|m|-1)\phi]-\cos[(|m|+1)\phi] & m<0. \end{cases} \\
= & \frac{1}{2}\begin{cases} \sin[(m+1)\phi]-\sin[(m-1)\phi] & m>1, \\ \sin[2\phi] & m=1, \\ 2\sin(\phi) & m=0, \\ 1-\cos[2\phi] & m=-1, \\ \cos[(m+1)\phi]-\cos[(m-1)\phi] & m<-1. \end{cases} = \frac{1}{2}\begin{cases} 2\Phi_{-1}(\phi) & m=0, \\ \Phi_{-2}(\phi) & m=1, \\ \Phi_{-(m+1)}(\phi)-\Phi_{-(m-1)}(\phi) & \text{else.} \end{cases} \quad \text{(B34)}
\end{aligned}
$$

Merging Eqs. B33 and B34 results in the following expressions:

$$
\begin{aligned}
&N_{l,|m|}\sin(\theta)P_l^{|m|}\left[\cos(\theta)\right]\sin(\phi)\Phi_m(\phi) = \frac{1}{2} \\
&\begin{cases}
-\left[\frac{(l-|m|+1)(l-|m|+2)}{(2l+1)(2l+3)}\right]^{\frac{1}{2}} N_{l+1,|m|-1}P_{l+1}^{|m|-1}[\cos(\theta)]\Phi_{-(m+1)}(\phi) + \left[\frac{(l+|m|)(l+|m|-1)}{(2l-1)(2l+1)}\right]^{\frac{1}{2}} N_{l-1,|m|-1}P_{l-1}^{|m|-1}[\cos(\theta)]\Phi_{-(m+1)}(\phi) \\
-\left[\frac{(l+|m|+1)(l+|m|+2)}{(2l+1)(2l+3)}\right]^{\frac{1}{2}} N_{l+1,|m|+1}P_{l+1}^{|m|+1}[\cos(\theta)]\Phi_{-(m-1)}(\phi) + \left[\frac{(l-|m|)(l-|m|-1)}{(2l-1)(2l+1)}\right]^{\frac{1}{2}} N_{l-1,|m|+1}P_{l-1}^{|m|+1}[\cos(\theta)]\Phi_{-(m-1)}(\phi) & m<-1 \\
-\left[\frac{l(l+1)}{(2l+1)(2l+3)}\right]^{\frac{1}{2}} N_{l+1,0}P_{l+1}^{0}[\cos(\theta)]\Phi_{0}(\phi) + \left[\frac{(l+1)l}{(2l-1)(2l+1)}\right]^{\frac{1}{2}} N_{l-1,0}P_{l-1}^{0}[\cos(\theta)]\Phi_{0}(\phi) \\
-\left[\frac{(l+2)(l+3)}{(2l+1)(2l+3)}\right]^{\frac{1}{2}} N_{l+1,2}P_{l+1}^{2}[\cos(\theta)]\Phi_{2}(\phi) + \left[\frac{(l-1)(l-2)}{(2l-1)(2l+1)}\right]^{\frac{1}{2}} N_{l-1,2}P_{l-1}^{2}[\cos(\theta)]\Phi_{2}(\phi) & m=-1, \\
2\left[\frac{(l+1)(l+2)}{(2l+1)(2l+3)}\right]^{\frac{1}{2}} N_{l+1,1}P_{l+1}^{1}[\cos(\theta)]\Phi_{-1}(\phi) - 2\left[\frac{l(l-1)}{(2l-1)(2l+1)}\right]^{\frac{1}{2}} N_{l-1,1}P_{l-1}^{1}[\cos(\theta)]\Phi_{-1}(\phi) & m=0, \\
\left[\frac{(l+2)(l+3)}{(2l+1)(2l+3)}\right]^{\frac{1}{2}} N_{l+1,2}P_{l+1}^{2}[\cos(\theta)]\Phi_{-2}(\phi) - \left[\frac{(l-1)(l-2)}{(2l-1)(2l+1)}\right]^{\frac{1}{2}} N_{l-1,2}P_{l-1}^{2}[\cos(\theta)]\Phi_{-2}(\phi) & m=1, \\
\left[\frac{(l+|m|+1)(l+|m|+2)}{(2l+1)(2l+3)}\right]^{\frac{1}{2}} N_{l+1,|m|+1}P_{l+1}^{|m|+1}[\cos(\theta)]\Phi_{-(m+1)}(\phi) - \left[\frac{(l-|m|)(l-|m|-1)}{(2l-1)(2l+1)}\right]^{\frac{1}{2}} N_{l-1,|m|+1}P_{l-1}^{|m|+1}[\cos(\theta)]\Phi_{-(m+1)}(\phi) \\
+\left[\frac{(l-|m|+1)(l-|m|+2)}{(2l+1)(2l+3)}\right]^{\frac{1}{2}} N_{l+1,|m|-1}P_{l+1}^{|m|-1}[\cos(\theta)]\Phi_{-(m-1)}(\phi) - \left[\frac{(l+|m|)(l+|m|-1)}{(2l-1)(2l+1)}\right]^{\frac{1}{2}} N_{l-1,|m|-1}P_{l-1}^{|m|-1}[\cos(\theta)]\Phi_{-(m-1)}(\phi) & m>1.
\end{cases}
\end{aligned}
\tag{B35}
$$

Therefore,

$$\sin(\theta)\sin(\phi)S_{l,m}(\theta,\phi) = \frac{1}{2}\begin{cases} -\left[\frac{(l-|m|+1)(l-|m|+2)}{(2l+1)(2l+3)}\right]^{\frac{1}{2}} S_{l+1,-(m+1)}(\theta,\phi) + \left[\frac{(l+|m|)(l+|m|-1)}{(2l-1)(2l+1)}\right]^{\frac{1}{2}} S_{l-1,-(m+1)}(\theta,\phi) & \\ -\left[\frac{(l+|m|+1)(l+|m|+2)}{(2l+1)(2l+3)}\right]^{\frac{1}{2}} S_{l+1,-(m-1)}(\theta,\phi) + \left[\frac{(l-|m|)(l-|m|-1)}{(2l-1)(2l+1)}\right]^{\frac{1}{2}} S_{l-1,-(m-1)}(\theta,\phi) & m < -1 \\ -\sqrt{2}\left[\frac{l(l+1)}{(2l+1)(2l+3)}\right]^{\frac{1}{2}} S_{l+1,0}(\theta,\phi) + \sqrt{2}\left[\frac{(l+1)l}{(2l-1)(2l+1)}\right]^{\frac{1}{2}} S_{l-1,0}(\theta,\phi) & \\ -\left[\frac{(l+2)(l+3)}{(2l+1)(2l+3)}\right]^{\frac{1}{2}} S_{l+1,2}(\theta,\phi) + \left[\frac{(l-1)(l-2)}{(2l-1)(2l+1)}\right]^{\frac{1}{2}} S_{l-1,2}(\theta,\phi) & m = -1, \\ \sqrt{2}\left[\frac{(l+1)(l+2)}{(2l+1)(2l+3)}\right]^{\frac{1}{2}} S_{l+1,-1}(\theta,\phi) - \sqrt{2}\left[\frac{l(l-1)}{(2l-1)(2l+1)}\right]^{\frac{1}{2}} S_{l-1,-1}(\theta,\phi) & m = 0, \\ \left[\frac{(l+2)(l+3)}{(2l+1)(2l+3)}\right]^{\frac{1}{2}} S_{l+1,-2}(\theta,\phi) - \left[\frac{(l-1)(l-2)}{(2l-1)(2l+1)}\right]^{\frac{1}{2}} S_{l-1,-2}(\theta,\phi) & m = 1, \\ \left[\frac{(l+|m|+1)(l+|m|+2)}{(2l+1)(2l+3)}\right]^{\frac{1}{2}} S_{l+1,-(m+1)}(\theta,\phi) - \left[\frac{(l-|m|)(l-|m|-1)}{(2l-1)(2l+1)}\right]^{\frac{1}{2}} S_{l-1,-(m+1)}(\theta,\phi) & \\ + \left[\frac{(l-|m|+1)(l-|m|+2)}{(2l+1)(2l+3)}\right]^{\frac{1}{2}} S_{l+1,-(m-1)}(\theta,\phi) - \left[\frac{(l+|m|)(l+|m|-1)}{(2l-1)(2l+1)}\right]^{\frac{1}{2}} S_{l-1,-(m-1)}(\theta,\phi) & m > 1. \end{cases} \tag{B36}$$

Equation B36 can be further reduced by the application of several Kronecker δ functions to give the following unified expression:

$$\begin{aligned}\sin(\theta)\sin(\phi)S_{l,m}(\theta,\phi) =& \frac{(-1)^{\delta_{m,-|m|}}}{2}\{(-\sqrt{2})^{\delta_{m,0}}(\sqrt{2})^{\delta_{m,-1}}\left[n^2_{l+1,m+1}S_{l+1,-(m+1)}(\theta,\phi) - n^2_{l,-m}S_{l-1,-(m+1)}(\theta,\phi)\right] \\ &+ (1-\delta_{m,0}-\delta_{m,1})\left[n^2_{l+1,-(m-1)}S_{l+1,-(m-1)}(\theta,\phi) - n^2_{l,m}S_{l-1,-(m-1)}(\theta,\phi)\right]\},\end{aligned} \tag{B37}$$

where we have defined $n^2_{l,m} \equiv \left[\frac{(l+m-1)(l+m)}{(2l-1)(2l+1)}\right]^{\frac{1}{2}}$.

Finally, adding the radial part one finds that:

$$
\begin{aligned}
y|n,l,m>=&\frac{(-1)^{\delta_{m,-|m|}}\sqrt{(2n+1)(2n+2)}}{4\zeta}\\
&\{(-\sqrt{2})^{\delta_{m,0}}(\sqrt{2})^{\delta_{m,-1}}\left[n^2_{l+1,m+1}|n+1,l+1,-(m+1)>-n^2_{l,-m}|n+1,l-1,-(m+1)>\right]+\\
&(1-\delta_{m,0}-\delta_{m,1})\left[n^2_{l+1,-(m-1)}|n+1,l+1,-(m-1)>-n^2_{l,m}|n+1,l-1,-(m-1)>\right]\}.
\end{aligned}
\tag{B38}
$$

The resulting integral is a linear combination of 16 overlap terms:

$$
\begin{aligned}
&{}_\beta\left\langle n_2, l_2, m_2|y^2|n_1, l_1, m_1\right\rangle_\alpha = \frac{(-1)^{\delta_{m_1,-|m_1|}+\delta_{m_2,-|m_2|}}\sqrt{(2n_1+1)(2n_1+2)(2n_2+1)(2n_2+2)}}{16\zeta_1\zeta_2} \\
&\{(-\sqrt{2})^{\delta_{m_1,0}}(\sqrt{2})^{\delta_{m_1,-1}}(-\sqrt{2})^{\delta_{m_2,0}}(\sqrt{2})^{\delta_{m_2,-1}} n^2_{l_1+1,m_1+1} n^2_{l_2+1,m_2+1}\ {}_\beta\left\langle n_2+1, l_2+1, -(m_2+1)|n_1+1, l_1+1, -(m_1+1)\right\rangle_\alpha \\
&-(-\sqrt{2})^{\delta_{m_1,0}}(\sqrt{2})^{\delta_{m_1,-1}}(-\sqrt{2})^{\delta_{m_2,0}}(\sqrt{2})^{\delta_{m_2,-1}} n^2_{l_1+1,m_1+1} n^2_{l_2,-m_2}\ {}_\beta\left\langle n_2+1, l_2-1, -(m_2+1)|n_1+1, l_1+1, -(m_1+1)\right\rangle_\alpha \\
&+(-\sqrt{2})^{\delta_{m_1,0}}(\sqrt{2})^{\delta_{m_1,-1}}(1-\delta_{m_2,0}-\delta_{m_2,1}) n^2_{l_1+1,m_1+1} n^2_{l_2+1,-(m_2-1)}\ {}_\beta\left\langle n_2+1, l_2+1, -(m_2-1)|n_1+1, l_1+1, -(m_1+1)\right\rangle_\alpha \\
&-(-\sqrt{2})^{\delta_{m_1,0}}(\sqrt{2})^{\delta_{m_1,-1}}(1-\delta_{m_2,0}-\delta_{m_2,1}) n^2_{l_1+1,m_1+1} n^2_{l_2,m_2}\ {}_\beta\left\langle n_2+1, l_2-1, -(m_2-1)|n_1+1, l_1+1, -(m_1+1)\right\rangle_\alpha \\
&-(-\sqrt{2})^{\delta_{m_1,0}}(\sqrt{2})^{\delta_{m_1,-1}}(-\sqrt{2})^{\delta_{m_2,0}}(\sqrt{2})^{\delta_{m_2,-1}} n^2_{l_1,-m_1} n^2_{l_2+1,m_2+1}\ {}_\beta\left\langle n_2+1, l_2+1, -(m_2+1)|n_1+1, l_1-1, -(m_1+1)\right\rangle_\alpha \\
&+(-\sqrt{2})^{\delta_{m_1,0}}(\sqrt{2})^{\delta_{m_1,-1}}(-\sqrt{2})^{\delta_{m_2,0}}(\sqrt{2})^{\delta_{m_2,-1}} n^2_{l_1,-m_1} n^2_{l_2,-m_2}\ {}_\beta\left\langle n_2+1, l_2-1, -(m_2+1)|n_1+1, l_1-1, -(m_1+1)\right\rangle_\alpha \\
&-(-\sqrt{2})^{\delta_{m_1,0}}(\sqrt{2})^{\delta_{m_1,-1}}(1-\delta_{m_2,0}-\delta_{m_2,1}) n^2_{l_1,-m_1} n^2_{l_2+1,-(m_2-1)}\ {}_\beta\left\langle n_2+1, l_2+1, -(m_2-1)|n_1+1, l_1-1, -(m_1+1)\right\rangle_\alpha \\
&+(-\sqrt{2})^{\delta_{m_1,0}}(\sqrt{2})^{\delta_{m_1,-1}}(1-\delta_{m_2,0}-\delta_{m_2,1}) n^2_{l_1,-m_1} n^2_{l_2,m_2}\ {}_\beta\left\langle n_2+1, l_2-1, -(m_2-1)|n_1+1, l_1-1, -(m_1+1)\right\rangle_\alpha \\
&+(1-\delta_{m_1,0}-\delta_{m_1,1})(-\sqrt{2})^{\delta_{m_2,0}}(\sqrt{2})^{\delta_{m_2,-1}} n^2_{l_1+1,-(m_1-1)} n^2_{l_2+1,m_2+1}\ {}_\beta\left\langle n_2+1, l_2+1, -(m_2+1)|n_1+1, l_1+1, -(m_1-1)\right\rangle_\alpha \\
&-(1-\delta_{m_1,0}-\delta_{m_1,1})(-\sqrt{2})^{\delta_{m_2,0}}(\sqrt{2})^{\delta_{m_2,-1}} n^2_{l_1+1,-(m_1-1)} n^2_{l_2,-m_2}\ {}_\beta\left\langle n_2+1, l_2-1, -(m_2+1)|n_1+1, l_1+1, -(m_1-1)\right\rangle_\alpha \\
&+(1-\delta_{m_1,0}-\delta_{m_1,1})(1-\delta_{m_2,0}-\delta_{m_2,1}) n^2_{l_1+1,-(m_1-1)} n^2_{l_2+1,-(m_2-1)}\ {}_\beta\left\langle n_2+1, l_2+1, -(m_2-1)|n_1+1, l_1+1, -(m_1-1)\right\rangle_\alpha \\
&-(1-\delta_{m_1,0}-\delta_{m_1,1})(1-\delta_{m_2,0}-\delta_{m_2,1}) n^2_{l_1+1,-(m_1-1)} n^2_{l_2,m_2}\ {}_\beta\left\langle n_2+1, l_2-1, -(m_2-1)|n_1+1, l_1+1, -(m_1-1)\right\rangle_\alpha \\
&-(1-\delta_{m_1,0}-\delta_{m_1,1})(-\sqrt{2})^{\delta_{m_2,0}}(\sqrt{2})^{\delta_{m_2,-1}} n^2_{l_1,m_1} n^2_{l_2+1,m_2+1}\ {}_\beta\left\langle n_2+1, l_2+1, -(m_2+1)|n_1+1, l_1-1, -(m_1-1)\right\rangle_\alpha \\
&+(1-\delta_{m_1,0}-\delta_{m_1,1})(-\sqrt{2})^{\delta_{m_2,0}}(\sqrt{2})^{\delta_{m_2,-1}} n^2_{l_1,m_1} n^2_{l_2,-m_2}\ {}_\beta\left\langle n_2+1, l_2-1, -(m_2+1)|n_1+1, l_1-1, -(m_1-1)\right\rangle_\alpha \\
&-(1-\delta_{m_1,0}-\delta_{m_1,1})(1-\delta_{m_2,0}-\delta_{m_2,1}) n^2_{l_1,m_1} n^2_{l_2+1,-(m_2-1)}\ {}_\beta\left\langle n_2+1, l_2+1, -(m_2-1)|n_1+1, l_1-1, -(m_1-1)\right\rangle_\alpha \\
&+(1-\delta_{m_1,0}-\delta_{m_1,1})(1-\delta_{m_2,0}-\delta_{m_2,1}) n^2_{l_1,m_1} n^2_{l_2,m_2}\ {}_\beta\left\langle n_2+1, l_2-1, -(m_2-1)|n_1+1, l_1-1, -(m_1-1)\right\rangle_\alpha\}.
\end{aligned}
\tag{B39}
$$

As mentioned above the choice of pointing the magnetic field along the X axis is arbitrary. Nevertheless, if one is still interested in magnetic fields not pointing along one of the Cartesian axes similar expressions can be found for the other angular momentum components integrals using the same methodology presented above.

[1] N. S. Hush, *Ann. N.Y. Acad. Sci.* **1006**, 1 (2003).

[2] R. S. Mulliken, *J. Chem. Phys.* **7**, 20 (1939).

[3] R. A. Marcus, *J. Chem. Phys.* **24**, 966 (1956).

[4] G. Briegleb, *Elektronen-Donator-Acceptor Komplexe* (Springer-Verlag, Gottingen, 1961).

[5] R. S. Mulliken and W. B. Person, *Ann. Rev. Phys. Chem.* **13**, 107 (1962).

[6] R. A. Marcus, *J. Chem. Phys.* **43**, 679 (1965).

[7] R. S. Mulliken and W. B. Person, *Molecular Complexes* (Wiley-Interscience, New York, 1969).

[8] N. R. Kestner, J. Logan, and J. Jortner, *J. Phys. Chem.* **78**, 2148 (1974).

[9] M. Bixon and J. Jortner, *Faraday Discuss. Chem. Soc.* **74**, 17 (1982).

[10] M. Bixon and J. Jortner, *Adv. in Chem. Physics* **106**, 35 (1999).

[11] A. Aviram and M. A. Ratner, *Chem. Phys. Lett.* **29**, 277 (1974).

[12] R. M. Metzger, *J. Macromol. Sci. Pure Appl. Chem.* **A38**, 1499 (2001).

[13] G. Binning, H. Rohrer, C. Gerber, and E. Weibel, *Appl. Phys. Lett.* **40**, 178 (1982).

[14] G. Binning, H. Rohrer, C. Gerber, and E. Weibel, *Phys. Rev. Lett.* **49**, 57 (1982).

[15] G. Binning, C. F. Quate, and C. Gerber, *Phys. Rev. Lett.* **56**, 930 (1986).

[16] M. F. Crommie, C. P. Lutz, and D. M. Eigler, *Science* **262**, 218 (1993).

[17] H. C. Manoharan, C. P. Lutz, and D. M. Eigler, *Nature* **403**, 512 (2000).

[18] G. V. Nazin, X. H. Qiu, and W. Ho, *Science* **302**, 77 (2003).

[19] G. P. Collins, *Physics Today* **46**, 17 (1993).

[20] J. Jortner and M. Ratner, *Molecular Electronics* (Blackwell Science Inc., New York, 1997).

[21] C. Roth and C. Joachim, *Atomic and Molecular Wires* (Kluwer, Dordrecht, 1997).

[22] E. G. Emberly and G. Kirczenow, *Molecular Electronics: Science and Technology* **852**, 54 (1998).

[23] C. Dekker, *Physics Today* **52**, 22 (1999).

[24] M. Ratner, *Nature* **404**, 137 (2000).

[25] C. Joachim, J. k. Gimzewski, and A. Aviram, *Nature* **408**, 541 (2000).

[26] J. M. Tour, *Acc. Chem. Res.* **33**, 791 (2000).

[27] A. Nitzan, *Ann. Rev. Phys. Chem.* **52**, 681 (2001).

[28] S. T. Pantelides, M. D. Ventra, and N. D. Lang, *Physica B* **296**, 72 (2001).

[29] P. Avouris, *Acc. Chem. Res.* **35**, 1026 (2002).

[30] A. Nitzan and M. A. Ratner, *Science* **300**, 1384 (2003).

[31] J. R. Heath and M. A. Ratner, *Physics Today* **56**, 43 (2003).

[32] M. A. Reed, C. Zhou, C. J. Muller, T. P. Burgin, and J. M. Tour, *Science* **278**, 252 (1997).

[33] C. Kergueris, J. P. Bourgoin, S. Palacin, D. Esteve, C. Urbina, M. Magoga, and C. Joachim, *Phys. Rev. B* **59**, 12505 (1999).

[34] H. B. Weber, J. Reichert, F. Weigend, R. Ochs, D. Beckmann, M. Mayor, R. Ahlrichs, and H. von Lohneysen, *Chem. Phys.* **281**, 113 (2002).

[35] R. H. M. Smit, Y. Noat, C. Untiedt, N. D. Lang, M. C. van Hemert, and J. M. van Ruitenbeek, *Nature* **419**, 906 (2002).

[36] H. Park, A. K. L. Lim, A. P. Alivisatos, J. Park, and P. L. McEuen, *Appl. Phys. Lett.* **75**, 301 (1999).

[37] W. J. Liang, M. P. Shores, M. Bockrath, J. R. Long, and H. Park, *Nature* **417**, 725 (2002).

[38] Y. Selzer, L. T. Cai, M. A. Cabassi, Y. X. Yao, J. M. Tour, T. S. Mayer, and D. L. Allara, *Nano Lett.* **5**, 61 (2005).

[39] M. A. Guillorn, D. W. Carr, R. C. Tiberio, E. Greenbaum, and M. L. Simpson, *J. Vac. Sci. Technol. B* **18**, 1177 (2000).

[40] J. Park, A. N. Pasupathy, J. I. Goldsmith, C. Chang, Y. Yaish, J. R. Petta, M. Rinkoski, J. P. Sethna, H. D. Abruna, P. L. McEuen, and D. C. Ralph, *Nature* **417**, 722 (2002).

[41] D. L. Klein, P. L. McEuen, J. E. B. Katari, R. Roth, and A. P. Alivisatos, *Appl. Phys. Lett.* **68**, 2574 (1996).

[42] D. Davidovic and M. Tinkham, *Appl. Phys. Lett.* **73**, 3959 (1998).

[43] A. F. Morpurgo, C. M. Marcus, and D. B. Robinson, *Appl. Phys. Lett.* **74**, 2084 (1999).

[44] C. Z. Li, H. X. He, and N. J. Tao, *Appl. Phys. Lett.* **77**, 3995 (2000).

[45] Y. V. Kervennic, H. S. J. V. der Zant, A. F. Morpurgo, L. Gurevich, and L. P. Kouwenhoven, *Appl. Phys. Lett.* **80**, 321 (2002).

[46] S. Frank, P. Poncharal, Z. L. Wang, and W. A. de Heer, *Science* **280**, 1744 (1998).

[47] K. Slowinski, H. K. Y. Fong, and M. Majda, *J. Am. Chem. Soc.* **121**, 7257 (1999).

[48] R. E. Holmlin, R. Haag, M. L. Chabinyc, R. F. Ismagilov, A. E. Cohen, A. Terfort, M. A. Rampi, and G. M. Whitesides, *J. Am. Chem. Soc.* **123**, 5075 (2001).

[49] J. G. Kushmerick, D. B. Holt, J. C. Yang, J. Naciri, M. H. Moore, and R. Shashidhar, *Phys.*

Rev. Lett. **89**, 086802 (2002).

[50] M. Dorogi, J. G. R. Osifchin, R. P. Andres, and R. Reifenberger, *Phys. Rev. B* **52**, 9071 (1995).

[51] D. I. Gittins, D. Bethell, D. J. Schiffrin, and R. J. Nichol, *Nature* **408**, 67 (2000).

[52] X. D. Cui, A. Primak, X. Zarate, J. Tomfohr, O. F. Sankey, A. L. Moore, T. A. Moore, D. Gust, G. Harris, and S. M. Lindsay, *Science* **294**, 571 (2001).

[53] S. J. Tans, M. H. Devoret, H. Dai, A. Thess, R. E. Smalley, L. J. Geerligs, and C. Dekker, *Nature* **386**, 474 (1997).

[54] D. Porath, A. Bezryadin, S. de Vries, and C. Dekker, *Nature* **403**, 635 (2000).

[55] R. F. Service, *Science* **302**, 556 (2003).

[56] R. Landauer, *IBM J. Res. Dev.* **1**, 223 (1957).

[57] W. Tian, S. Datta, S. Hong, R. Reifenberger, J. I. Henderson, and C. P. Kubiak, *J. Chem. Phys.* **109**, 2874 (1998).

[58] R. Baer and D. Neuhauser, *J. Am. Chem. Soc.* **124**, 4200 (2002).

[59] R. Collepardo-Guevara, D. Walter, D. Neuhauser, and R. Baer, *Chem. Phys. Lett.* **393**, 367 (2004).

[60] O. Hod, R. Baer, and E. Rabani, *J. Phys. Chem. B* **108**, 14807 (2004).

[61] O. Hod, E. Rabani, and R. Baer, *J. Chem. Phys.* **123**, 051103 (2005).

[62] O. Hod, R. Baer, and E. Rabani, *J. Am. Chem. Soc.* **127**, 1648 (2005).

[63] S. Datta, *Electronic Transport in Mesoscopic Systems* (Cambridge University Press, Cambridge, 1995).

[64] V. Mujica, M. Kemp, A. Roitberg, and M. Ratner, *J. Chem. Phys.* **104**, 7296 (1996).

[65] L. E. Hall, J. R. Reimers, N. S. Hush, and K. Silverbrook, *J. Chem. Phys.* **112**, 1510 (2000).

[66] Y. Xue, S. Datta, and M. A. Ratner, *J. Chem. Phys.* **115**, 4292 (2001).

[67] A. W. Ghosh, F. Zahid, S. Datta, and R. R. Brige, *Chem. Phys.* **281**, 225 (2002).

[68] J. Heurich, J. C. Cuevas, W. Wenzel, and G. Schon, *Phys. Rev. Lett.* **88**, 256803 (2002).

[69] M. Brandbyge, J. L. Mozos, P. Ordejon, J. Taylor, and K.Stokbro, *Phys. Rev. B* **65**, 165401 (2002).

[70] S. Hou, J. Zhang, R. Li, J. Ning, R. Han, Z. Shen, X. Zhao, Z. Xue, and Q. Wu, *Nanotechnology* **16**, 239 (2005).

[71] R. Baer, T. Seideman, S. Ilani, and D. Neuhauser, *J. Chem. Phys.* **120**, 3387 (2003).

[72] R. Baer and D. Neuhauser, *Int. J. Quant. Chem.* **91**, 524 (2003).

[73] G. Stefanucci and C.-O. Almbladh, *Europhys. Lett.* **67**, 14 (2004).

[74] N. Sai, M. Zwolak, G. Vignale, and M. D. Ventra, *Phys. Rev. Lett.* **94**, 186810 (2005).

[75] S. Kurth, G. Stefanucci, C.-O. Almbladh, A. Rubio, and E. K. U. Gross, *Phys. Rev. B* **72**, 035308 (2005).

[76] P. Delaney and J. C. Greer, *Phys. Rev. Lett.* **93**, 036805 (2004).

[77] K. Burke, R. Car, and R. Gebauer, *Phys. Rev. Lett.* **94**, 146803 (2005).

[78] Y. Aharonov and D. Bohm, *Phys. Rev.* **115**, 485 (1959).

[79] W. Eherenberg and R. E. Siday, *Proc. Phys. Soc. (London)* **B62**, 8 (1949).

[80] R. G. Chambers, *Phys. Rev. Lett.* **5**, 3 (1960).

[81] R. D. Parks and W. A. Little, *Phys. Rev.* **133**, 000A97 (1964).

[82] D. Y. Sharvin and Y. V. Sharvin, *JETP Lett.* **34**, 272 (1981).

[83] B. L. Al'tshuler, A. G. Aronov, B. Z. Spivak, D. Y. Sharvin, and Y. V. Sharvin, *JETP Lett.* **35**, 588 (1982).

[84] G. Möllensdedt, H. Schmid, and H. Lichte, *Proc. 10th Int. Congress on Electron Microscopy* (Deutschgesellschaft für Elektronen Mikroskopie, Hamburg, 1982).

[85] A. Tonomura, T. Matsuda, R. Suzuki, A. Fukuhara, N. Osakabe, H. Umezaki, J. Endo, K. Shinagawa, Y. Sugita, and H. Fujiwara, *Phys. Rev. Lett.* **48**, 1443 (1982).

[86] N. B. Brandt, E. N. Bogachek, D. V. Gitsu, G. A. Gogadze, I. O. Kulik, A. A. Nikolaeva, and Y. G. Ponomarev, *Fiz. Nisk. Temp.* **8**, 718 (1982).

[87] F. R. Ladan and J. Maurer, *C. R. Acad. Sci.* **297**, 227 (1983).

[88] H. Schmid, *Proc. 8th European Congress on Electron Microscopy (eds Csanady, A., Rohlich, P. and Szabo, D.)* (Programme Committee of the 8th Eur. Congr. on Electron Microsc., Budapest, 1984).

[89] M. Gijs, C. van Haesandonck, and Y. Bruynseraede, *Phys. Rev. Lett.* **52**, 2069 (1984).

[90] M. Gijs, C. van Haesandonck, and Y. Bruynseraede, *Phys. Rev. B* **30**, 2964 (1984).

[91] B. Pannetier, J. Chaussy, R. Rammal, and P. Gandit, *Phys. Rev. Lett.* **53**, 718 (1984).

[92] Y. V. Sharvin, *Physica (Amsterdam)* **126B**, 288 (1984).

[93] J. M. Gordon, *Phys. Rev. B* **30**, 6770 (1984).

[94] B. Pannetier, J. Chaussy, R. Rammal, and P. Gandit, *Phys. Rev. B* **31**, 3209 (1985).

[95] G. J. Dolan, *Bull. Am. Phys. Soc.* **30**, 395 (1985).

[96] B. L. Al'tshuler, A. G. Aronov, and B. Z. Spivak, *JETP Lett.* **33**, 94 (1981).

[97] M. Büttiker, Y. Imry, and R. Landauer, *Phys. Lett. A* **96**, 365 (1983).

[98] Y. Gefen, Y. Imry, and M. Y. Azbel, *Surf. Sci.* **142**, 203 (1984).

[99] Y. Gefen, Y. Imry, and M. Y. Azbel, *Phys. Rev. Lett.* **52**, 129 (1984).

[100] M. Büttiker, Y. Imry, and M. Y. Azbel, *Phys. Rev. A* **30**, 1982 (1984).

[101] J. P. Carini, K. A. Muttalib, and S. R. Nagel, *Phys. Rev. Lett.* **53**, 102 (1984).

[102] D. A. Browne, J. P. Carini, K. A. Muttalib, and S. R. Nagel, *Phys. Rev. B* **30**, 6798 (1984).

[103] M. Büttiker, Y. Imry, R. Landauer, and S. Pinhas, *Phys. Rev. B* **31**, 6207 (1985).

[104] R. A. Webb, S. Washburn, C. P. Umbach, and R. B. Laibowitz, *Phys. Rev. Lett.* **54**, 2696 (1985).

[105] A. G. Aronov and Y. V. Sharvin, *Rev. Mod. Phys.* **59**, 755 (1987).

[106] D. C. Ralph, C. T. Black, and M. Tinkham, *Phys. Rev. Lett.* **78**, 4087 (1997).

[107] D. H. Cobden, M. Bockrath, P. L. McEuen, A. G. Rinzler, and R. E. Smalley, *Phys. Rev. Lett.* **81**, 681 (1998).

[108] D. H. Cobden, M. Bockrath, N. G. Chopra, A. Zettl, P. L. McEuen, A. Rinzler, A. Thess, and R. E. Smalley, *Physica B: Cond. Mat.* **251**, 132 (1998).

[109] S. M. Cronenwett, T. H. Oosterkamp, and L. P. Kouwenhoven, *Science* **281**, 540 (1998).

[110] D. Goldhaber-Gordon, H. Shtrikman, D. Mahalu, D. Abusch-Magder, U. Meirav, and M. A. Kastner, *Nature* **391**, 156 (1998).

[111] J. N. ringrd, D. H. Cobden, and P. E. Lindelof, *Nature* **408**, 342 (2000).

[112] M. R. Buitelaar, T. Nussbaumer, , and C. Schönenberger, *Phys. Rev. Lett.* **89**, 256801 (2002).

[113] A. N. Pasupathy, R. C. Bialczak, J. Martinek, J. E. Grose, L. A. K. Donev, P. L. McEuen, and D. C. Ralph, *Science* **306**, 86 (2004).

[114] L. H. Yu and D. Natelson, *Nano Lett.* **4**, 79 (2004).

[115] S. Tarucha, D. G. Austing, T. Honda, R. J. van der Hage, and L. P. Kouwenhoven, *Phys. Rev. Lett.* **77**, 3613 (1996).

[116] D. R. Stewart, D. Sprinzak, C. M. Marcus, C. I. Duruöz, and J. J. S. Harris, *Science* **278**, 1784 (1997).

[117] E. D. Minot, Y. Yaish, V. Sazonova, and P. L. McEuen, *Nature* **428**, 536 (2004).

[118] F. L. Carter, *Molecular Electronic devices II* (Marcel Dekker, New York, 1987).

[119] G. A. Prinz, *Phys. Today* **48**, 58 (1995).

[120] G. A. Prinz, *Science* **282**, 1660 (1998).

[121] A. Brataas, Y. V. Nazarov, and G. E. W. Bauer, *Phys. Rev. Lett.* **84**, 2481 (2000).

[122] F. J. Jedema, A. T. Filip, and B. J. van Wees, *Nature* **410**, 345 (2001).

[123] I. Malajovich, J. J. Berry, N. Samarth, and D. D. Awschalom, *Nature* **411**, 770 (2001).

[124] S. A. Wolf, D. D. Awschalom, R. A. Buhrman, J. M. Daughton, S. von Molnár, M. L. Roukes, A. Y. Chtchelkanova, and D. M. Treger, *Science* **294**, 1488 (2001).

[125] J. A. Gupta, R. Knobel, N. Samarth, and D. D. Awschalom, *Science* **292**, 2458 (2001).

[126] I. Žutić, J. Fabian, and S. D. Sarma, *Rev. Mod. Phys.* **76**, 323 (2004).

[127] P. Sharma, *Science* **307**, 531 (2005).

[128] A. Yacoby, M. Heiblum, D. Mahalu, and H. Shtrikman, *Phys. Rev. Lett.* **74**, 4047 (1995).

[129] R. Schuster, E. Buks, M. Heiblum, D. Mahalu, V. Umansky, and H. Shtrikman, *Nature* **385**, 417 (1997).

[130] Y. Ji, M. Heiblum, D. Sprinzak, D. Mahalu, and H. Shtrikman, *Science* **290**, 779 (2000).

[131] C. Kittel, *Introduction to Solid State Physics* (Wiley, New-York, 1996).

[132] Y. Gefen, Y. Imry, and N. Y. Azbel, *Phys. Rev. Lett.* **52**, 129 (1984).

[133] M. Cahay, S. Bandyopadhyay, and H. L. Grubin, *Phys. Rev. B* **39**, 12989 (1989).

[134] Y. Imry, *Introduction to Mesoscopic Physics, 2nd ed.* (Oxford University Press, Oxford, 2002).

[135] A. Aharony, O. Entin-Wohlman, and Y. Imry, *Phys. Rev. Lett.* **90**, 156802 (2003).

[136] C. Benjamin, S. Bandopadhyay, and A. M. Jayannavar, *Solid State Comm.* **124**, 331 (2002).

[137] A. M. Jayannavar and C. Benjamin, *Pramana - J. Phys.* **59**, 385 (2002).

[138] A. Aharony, O. Entin-Wohlman, B. I. Halperin, and Y. Imry, *Phys. Rev. B* **66**, 115311 (2002).

[139] G. A. Vugalter, A. K. Das, and V. A. Sorokin, *Eur. J. Phys.* **25**, 157 (2004).

[140] R. Martel, T. Schmidt, H. R. Shea, T. Hertel, and P. Avouris, *Appl. Phys. Lett.* **73**, 2447 (1998).

[141] S. J. Tans, A. R. M. Verschueren, and C. Dekker, *Nature* **393**, 49 (1998).

[142] A. Bachtold, P. Hadley, T. Nakanishi, and C. Dekker, *Science* **294**, 1317 (2001).

[143] H. W. C. Postma, T. Teepen, Z. Yao, M. Grifoni, and C. Dekker, *Science* **293**, 76 (2001).

[144] A. Javey, J. Guo, Q. Wang, M. Lundstrom, and H. Dai, *Nature* **424**, 654 (2003).

[145] C. H. Wu and D. Ramamurthy, *Phys. Rev. B* **65**, 075313 (2002).

[146] L. Onsager, *Phys. Rev.* **38**, 2265 (1931).

[147] M. Büttiker, *Phys. Rev. Lett.* **57**, 1761 (1986).

[148] O. Entin-Wohlman, A. Aharony, Y. Imry, Y. Levinson, and A. Schiller, *Phys. Rev. Lett.* **88**,

166801 (2002).

[149] T. Palm and L. Thylén, *J. Appl. Phys.* **79**, 8076 (1996).

[150] M.Galperin, M.A.Ratner, and A.Nitzan, *J. Chem. Phys.* **121**, 11965 (2004).

[151] T. N. Todorov, G. A. D. Briggs, and A. P. Sutton, *J. Phys.: Condens. Matter* **5**, 2389 (1993).

[152] G. D. Mahan, *Many-Particle Physics* (Plenum Press, New-York, 1990).

[153] S. Datta, *Nanotechnology* **15**, S433 (2004).

[154] S. Pleutin, H. Grabert, G. L. Ingold, and A. Nitzan, *J. Chem. Phys.* **118**, 3756 (2003).

[155] Y. Xue, S. Datta, and M. A. Ratner, *Chem. Phys.* **281**, 151 (2002).

[156] M. Paulsson, *arXiv:cond-mat/0210519 v1* (2002).

[157] M. P. L. Sancho, J. M. L. Sancho, and J. Rubio, *J. Phys. F.:Met. Phys.* **14**, 1205 (1984).

[158] M. P. L. Sancho, J. M. L. Sancho, and J. Rubio, *J. Phys. F.:Met. Phys.* **15**, 851 (1985).

[159] M. B. Nardelli, *Phys. Rev. B* **60**, 7828 (1999).

[160] D. Neuhauser and M. Baer, *J. Chem. Phys.* **90**, 4351 (1989).

[161] T. Seideman and W. H. Miller, *J. Chem. Phys.* **97**, 2499 (1992).

[162] U. V. Riss and H. D. Meyer, *J. Chem. Phys.* **105**, 1409 (1996).

[163] R. Hoffmann, *J. Chem. Phys.* **39**, 1397 (1963).

[164] C. Cohen-Tannoudji, B. Diu, and F. Laloë, *Quantum Mechanics* (Wiley, New York, 1977).

[165] J. C. Slater, *Phys. Rev.* **36**, 57 (1930).

[166] J. A. Pople and D. L. Beveridge, *Approximate Molecular Orbital Theory* (McGraw-Hill, New York, 1970).

[167] F. London, *J. Phys. Radium* **8**, 397 (1937).

[168] J. A. Pople, *J. Chem. Phys.* **37**, 53 (1962).

[169] I. I. Guseinov, *J. Phys. B.:Atom. Molec. Phys.* **3**, 1399 (1970).

[170] I. I. Guseinov, *Phys. Rev. A* **32**, 1864 (1985).

[171] I. I. Guseinov, A. Özmen, Ü. Atav, and H. Yüksel, *Int. J. Quant. Chem.* **67**, 199 (1998).

[172] I. I. Guseinov and B. A. Mamedov, *J. Mol. Struct. (Theochem)* **465**, 1 (1999).

[173] I. I. Guseinov, *Pramana - J. Phys.* **61**, C781 (2003).

[174] S. Iijima, *Nature (London)* **354**, 56 (1991).

[175] M. S. Dresselhaus, G. Dresselhaus, and P. C. Eklund, *Science of Fullerenes and Carbon Nanotubes* (Academic, San Diego, 1996).

[176] R. Saito, G. Dresselhaus, and M. S. Dresselhaus, *Pysical Properties of Carbon Nanotubes*

(Imperial College Press, London, 1999).

[177] P. J. F. Harris, *Carbon Nanotubes and Related Structures. New aterials for the Twenty-first Century* (Cambridge University Press, Cambridge, 2001).

[178] D. Qian, G. J. Wagner, W. K. Liu, M.-F. Yu, and R. S. Ruoff, *Appl. Mech. Rev.* **55**, 495 (2002).

[179] D. Srivastava, C. Wei, and K. Cho, *Appl. Mech. Rev.* **56**, 215 (2003).

[180] Z. Yao, H. W. C. Postma, L. Balents, and C. Dekker, *Nature* **402**, 273 (1999).

[181] P. G. Collins and P. Avouris, *Scientific American* page 62 (December 2000).

[182] M. S. Fuhrer, J. Nygard, L. Shih, M. Forero, Y.-G. Yoon, M. S. C. Mazzoni, H. J. Choi, J. Ihm, S. G. Louie, A. Zettl, and P. L. McEuen, *Science* **288**, 494 (2000).

[183] C. Zhou, J. Kong, E. Yenilmez, and H. Dai, *Science* **290**, 1552 (2000).

[184] T. Rueckes, K. Kim, E. Joselevich, G. Y. Tseng, C.-L. Cheung, and C. M. Lieber, *Science* **289**, 94 (2000).

[185] M. Bockrath, W. Liang, D. Bozovic, J. H. Hafner, C. M. Lieber, M. Tinkham, and H. Park, *Science* **291**, 283 (2001).

[186] G. Treboux, P. Lapstun, and K. Silverbrook, *Chem. Phys. Lett.* **306**, 402 (1999).

[187] F. Léonard and J. Tersoff, *Phys. Rev. Lett.* **85**, 4767 (2000).

[188] A. N. Andriotis, M. Menon, D. Srivastava, and L. Chernozatonskii, *Phys. Rev. Lett.* **87**, 66802 (2001).

[189] A. Bachtold, C. Strunk, J.-P. Salvetat, J.-M. Bonard, L. Forro, T. Nussbaumer, and C. Schonenberger, *Nature* **397**, 673 (1999).

[190] U. C. Coskun, T.-C. Wei, S. Vishveshwara, P. M. Goldbart, and A. Bezryadin, *Science* **304**, 1132 (2004).

[191] S. Zaric, G. N. Ostojic, J. Kono, J. Shavey, V. C. Moore, M. S. Strano, R. H. Hauge, R. E. Smalley., and X. Wei, *Science* **304**, 1129 (2004).

[192] W. Liang, M. Bockrath, D. Bozovic, J. H. Hafner, M. Tinkham, and H. Park, *Nature* **411**, 665 (2001).

[193] M. M. Deshmukh, A. L. Prieto, Q. Gu, and H. Park, *Nano Lett.* **3**, 1383 (2003).

[194] F. Q. Xie, L. Nittler, C. Obermair, and T. Schimmel, *prl* **93**, 128303 (2004).

[195] M. J. Biercuk, N. Mason, J. Martin, A. Yacoby, and C. M. Marcus, *prl* **94**, 026801 (2005).

[196] A. Javey, P. Qi, Q. Wang, and H. Dai, *Proc. Nat. Acad. Sci.* **101**, 13408 (2004).

[197] H. A. Staab and F. Diederich, *Angew. Chem. Int. Ed. Engl.* **17**, 372 (1978).

[198] H. A. Staab and F. Diederich, *Chem. Ber.* **116**, 3487 (1983).

[199] H. A. Staab, F. Diederich, C. Krieger, and D. Schweitzer, *Chem. Ber.* **116**, 3504 (1983).

[200] J. Cioslowski, P. B. O'connor, and E. D. Fleischmann, *J. Am. Chem. Soc.* **113**, 1086 (1991).

[201] J. Aihara, *J. Am. Chem. Soc.* **114**, 865 (1992).

[202] E. Steiner, P. W. Fowler, L. W. Jenneskens, and A. Acocellaa, *Chem. Commun.* pages 659–660 (2001).

[203] B. Hajgató and K. Ohno, *Chem. Phys. Lett.* **385**, 512 (2004).

[204] S. Tikhodeev, M. Natario, K. Makoshi, T. Mii, and H. Ueba, *Surface Science* **493**, 63 (2001).

[205] T. Mii, S. Tikhodeev, and H. Ueba, *Surface Science* **502-503**, 26 (2002).

[206] T. Mii, S. G. Tikhodeev, and H. Ueba, *Phys. Rev. B* **68**, 205406 (2003).

[207] A. Mitra, I. Aleiner, and A. J. Millis, *Phys. Rev. B* **69**, 245302 (2004).

[208] L. V. Keldysh, *Sov. Phys. JETP* **20**, 1018 (1965).

[209] L. P. Kadanoff and G. Baym, *Quantum Statistical Mechanics. Green's Function Methods in Equilibrium and Nonequilibrium Problems* (Benjamin, Reading, MA, 1962).

[210] M. Wagner, *Phys. Rev. B* **44**, 6104 (1991).

[211] A. B. Migdal, *Sov. Phys. JETP* **7**, 996 (1958).

[212] R. S. Mulliken, C. A. Rieke, D. Orloff, and H. Orloff, *J. Chem. Phys.* **17**, 1248 (1949).

[213] C. C. J. Roothaan, *J. Chem. Phys.* **19**, 1445 (1951).

[214] J. C. Slater and G. F. Koster, *Phys. Rev.* **94**, 1498 (1954).

[215] R. R. Sharma, *Phys. Rev. A* **13**, 517 (1976).

[216] S. W. Oh and S. Ahn, *J. Kor. Chem. Soc.* **23**, 125 (1979).

[217] W. Hierse and P. M. Oppeneer, *J. Chem. Phys.* **99**, 1278 (1993).

[218] W. Hierse and P. M. Oppeneer, *Int. J. Quant. Chem.* **52**, 1249 (1994).

[219] I. I. Guseinov, *J. Mol. Struct. (Theochem)* **367**, 83 (1996).

[220] H. W. Jones, *Int. J. Quant. Chem.* **61**, 881 (1997).

[221] S. M. Mekelleche and A. Baba-Ahmed, *Int. J. Quant. Chem.* **63**, 843 (1997).

[222] T. Özdogan and M. Orbay, *Int. J. Quant. Chem.* **87**, 15 (2002).

[223] B. A. Mamedov, M. Kara, and M. Orbay, *Chinese J. Phys.* **40**, 283 (2002).

[224] H. Ichimura and A. Rauk, *J. Chem. Phys.* **59**, 5720 (1973).

[225] R. L. Match and J. Anderson, *J. Chem. Phys.* **61**, 1252 (1974).

[226] I. I. Guseinov and F. S. Sadichov, *J. Phys. B: Atoms. Molec. Phys.* **10**, L507 (1977).

[227] I. I. Guseinov, *Int. J. Quant. Chem.* **68**, 145 (1997).

[228] I. I. Guseinov, B. A. Mamedov, T. Özdogan, and M. Orbay, *Pramana - J. Phys.* **53**, 727 (1999).

[229] M. E. Beck and G. Hohlneicher, *Theor. Chem. Acc.* **101**, 297 (1999).